UNIVERSITY OF CALGARY

VSP processing for coal reflections

by

Salman Bubshait

A THESIS
SUBMITTED TO THE FACULTY OF GRADUATE STUDIES
IN PARTIAL FULFILMENT OF THE REQUIREMENTS FOR THE
DEGREE OF MASTER OF SCIENCE

DEPARTMENT OF GEOSCIENCE
CALGARY, ALBERTA
FEBRUARY 2010

UNIVERSITY OF CALGARY

FACULTY OF GRADUATE STUDIES

The undersigned certify that they have read, and recommend to the Faculty of Graduate Studies for acceptance, a thesis entitled "VSP processing for coal reflections" submitted by Salman Bubshait in partial fulfilment of the requirements for the degree of Master of Science.

Supervisor, Dr. Donald Lawton, Department of Geoscience

Dr. Larry Lines, Department of Geoscience

Dr. Michael Wieser, Department of Physics and Astronomy

February 8, 2010

Abstract

Five VSP surveys were acquired in Alberta as part of a study of Mannville coals. The goal is to study the AVO variation in the Mannville coals to detect anomalies using VSP wavefields.

The zero offset VSP survey was processed using the VISTA software through to corridor stack and shows high reflection quality of P waves with no significant multiples in the data.

A log analysis and synthetic seismogram were generated to compare with the outside and inside corridor stacks obtained from the zero offset VSP survey. The top of the Mannville B coals was indicated by a sharp trough and/or decrease in impedance in all the stacks in addition to the synthetic. The synthetic seismogram proved to the best match to the outside corridor stack. Also, an analysis of the mute window proved that varying the mute from 30-70 ms gave the same approximate result possibly because of no significant multiples in the data.

Also, the three walkaway VSPs along different azimuths were processed through to the VSPCDP stage. A recommendation is suggested to have an overlap of a receiver in the borehole to minimize shot static errors. The walkaways displayed high reflection quality of both P and S waves that highlighted the Mannville coals. A slight improvement of the reflection of the coals is noticed in the SV waves over the P waves as offset increases.

An AVO study was performed on all three walkaway VSP surveys. The walkaways were converted to angle gathers and processed in the Hampson-Russell AVO and STRATA packages. Intercept versus gradient AVO crossplots were generated for the

Mannville B coals that indicated a potential gas anomaly in the southeast angle gathers. However, the east and southeast did not indicate a gas anomaly. The AVO intercept versus gradient crossplots consistently plotted the Mannville B coal with a strong AVO intercept in quadrant II.

Inversion was performed on the walkaway angle gathers to invert for the P and S wave impedances. The impedances then were utilized to generate the Lambda Rho versus the Mu Rho crossplots. All the Lambda Rho versus the Mu Rho crossplots indicated that the Mannville B coals plotted over the background trend indicating that the coals are non gas bearing. There were some physically impossible Lambda Rho values in the top of the Mannville Fm due to errors in the inversion but left the Mannville B coal target zone unaffected.

Acknowledgements

I would like to first and far most my advisor Professor Donald Lawton whom without which this project would not be possible.

I would also like to extend a special thanks to Rick Kuzmiski of GEDCO for offering consultation whenever needed. In addition, I would like to thank Carlos Montana and Mingyu Zhang of GEDCO.

Thank you for the CREWES sponsors for supporting this work, particularly Encana Corporation for providing access to the VSP data and GEDCO for proving VISTA VSP processing software.

In addition, I would like to thank my Professors and doctors at CREWES and the University of Calgary. Thank you Dr. Robert Stewart, Dr. Larry Lines, Dr. Robert Ferguson, Dr. Gary Margrave, Dr. Kristopher Innanen and Dr. Michael Wieser. In addition I would like to acknowledge my colleges, friends and staff at CREWES and the University of Calgary for their help and support. Thank you Mohammad Al-Duhailan, Abdullah Alshuhail, Laura Baird, Kevin Hall, Hussain Hammad, Cathy Hubbell, Dr. Rolf Mayer, Carlos Montana, Taher Sodager, and Zimin Zhang other CREWES staff for assistance. Lastly, I would like to thank Saudi Aramco for their scholarship support.

I would also like to thank the professionals in Aramco that facilitated my success. Thank you Dr. Muhammed Alsaggaf, Dr. Panos Kelamis, Dr. Timothy Keho, Dr. Nabeel Alafaleg, Suha Albehaisi, Lynda Oversby and all of the people of EXPEC ARC of Saudi Aramco.

Dedication

I would like to thank Allah The Almighty for giving me this opportunity to continue my studies. I cannot ask for a better life and for Allah I will always be faithful and grateful.

I would like to dedicate my work to my wife Sara who stood by me when needed most and was the source of my encouragement and source of hope an inspiration; making me eternally grateful. In addition, a special thanks goes to my parents who are the direct reason for the man that I am today. I cannot thank my parents enough for their endless support and prayers. I wish also to thank my sister, my brother and his family for their support.

Furthermore, I would like to express my gratitude to my wife’s family, from her mother, to her little sister, to her brothers and to her big sister and her husband and kids for their prayers and welcoming me into the family that I am proud and honored to be a part of.

Extended thanks goes to all my relatives from Almoaibed, Bubshait, Aldugaither, Alsarami, Alshaya, Alsowaygih, Alfaleh, Alhomaid, Aljindan and Alnaim families for their continuous prayers for my success. Their good intentions will be forever appreciated.

Moreover, I cannot forget to thank all my friends in Saudi Arabia, Canada and the USA for being good friends to me and continuously asking about my well being and treating me like family.

Lastly, all our prayers go to our brother Shaya Alshaya. May Allah grant him the highest level of heaven.

Table of Contents

List of Tables

List of Figures and Illustrations

List of Symbols, Abbreviations and Nomenclature

Symbol	Definition
U of C	University of Calgary
VSP	Vertical Seismic Profiling
CBM	Coal Bed Methane
KB	Kelly Bushing
MSL	Mean Sea Level
RMS	Root Mean Square
FRT	Field Record Timing
-TT	Wavefield minus the first break times
+TT	Wavefield plus the first break times
NMO	Normal Move Out
TWT	Two Way Time
TVD	Total Vertical Depth
CMP	Common Mid Point
TVR	Time Variant Rotation
AVO	Amplitude Variation with Offset
Vp	P wave velocity
Vs	S wave velocity
ρ	Density
λ	Incompressibility
μ	Rigidity
DHI	Direct Hydrocarbon Indicators
V_{INT}	Interval velocity
V_{RMS}	Root Mean Square Velocity
$R(\theta)$	Reflectivity with angle dependence
Rp	P wave reflectivity
Rs	S wave reflectivity
G	AVO gradient
$\lambda\rho$	Lambda Rho
$\mu\rho$	Mu Rho
Zp	P wave impedance
Zs	S wave impedance
Ip	P wave impedance
Is	S wave impedance
O	VSP to well offset
h	CDP half offset
a	Offset from midpoint to well
D	Depth from surface to reflector
dr	Depth from receiver to reflector
ds	Depth from surface to receiver
$\Delta\tau_k$	Traveltime across an interval
V_k	Average velocity across an interval
X, Y	Horizontal components
X’	Maximized energy component
Y’	Transverse energy component

CHAPTER 1: INTRODUCTION

1.1 Vertical seismic profiling introduction

Vertical Seismic Profiling (VSP) is used to obtain rock properties of a target horizon as well as to acquire a seismic image of the subsurface that helps with surface seismic interpretation and processing. Rock properties obtained from VSP surveys include velocity, attenuation, impedance and anisotropy. In addition, VSP surveys are used in the analysis of wave propagation (Stewart, 2001).

There are several ways in which a VSP survey is conducted. Generally, VSP surveys have receivers down the borehole and the sources on the surface. If a source is located tens of meters away from the borehole containing the receivers, then it is a “Zero Offset VSP Survey.” If there are several sources at multiple offsets from the borehole, then it is called a “Walkaway VSP Survey” or “Multi offset VSP survey.” In addition, if walkaway sources are at several azimuths from the borehole, the survey is called “Multi azimuth survey.” All of the surveys mentioned provide 2D images of the subsurface. A 3D image also can be obtained with a full areal set of sources (Stewart, 2001). Figure 1.1 shows a simple illustration of a VSP survey.

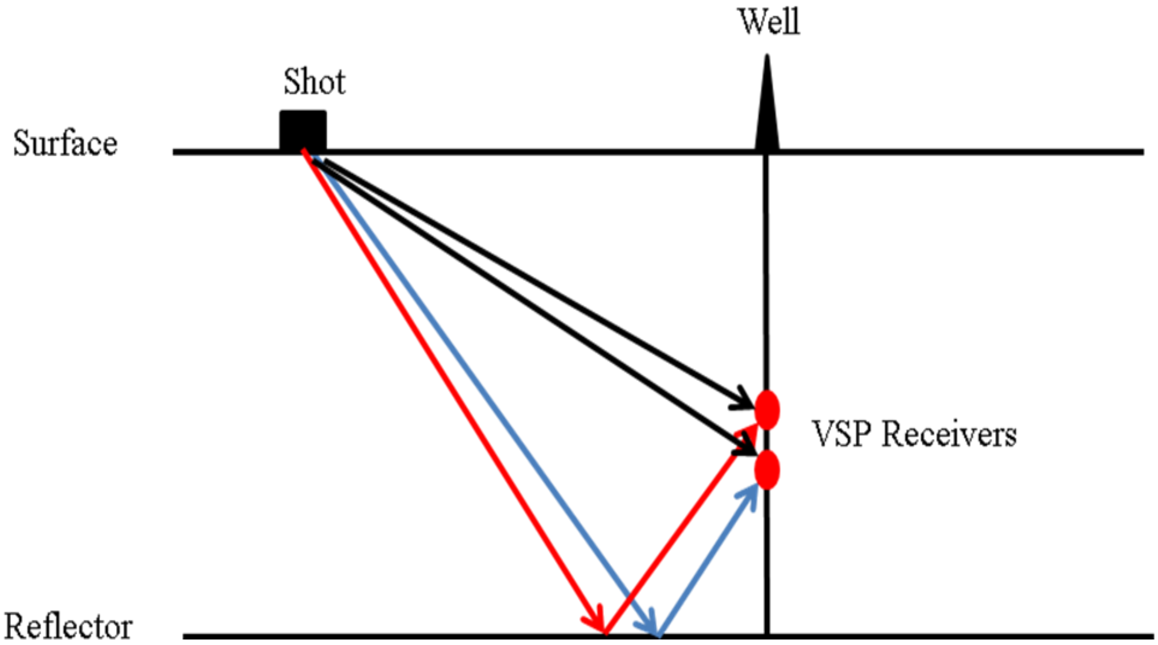

Figure 1.1: An illustration of a VSP survey. The red dots resemble receivers in the borehole while the arrows simulate ray paths.

Figure 1.1 resembles a simple zero offset VSP survey. The figure shows a single source with multiple receivers and multiple raypath reflections for a single reflector. The receivers are located in the borehole of the well and receive the various wavefields. The two black arrows show the downgoing waves going to the receiver directly. The red and blue arrows show two different raypaths to two different receivers.

In general, VSP acquisition has many advantages for exploration interests. VSP surveys provide a direct link between surface seismic and well log data to obtain information about lithology types and saturations. In addition, VSP surveys can provide necessary interval velocities if there is difficulty in obtaining a sonic log of the same well. A tremendous advantage that VSP surveys have over surface seismic data is that they measure both downgoing and upgoing wavefields. This advantage results in several insights one of which is measuring the source downgoing waves at each level to design a deconvolution operator to be applied to the upgoing waves in order to obtain seismic reflectivity. Seismic reflectivity is related to the response of the geological layers in terms of seismic impedance. Seismic impedance is the product of velocity and density of each layer that the seismic waves travel in. In addition, VSP reflections could have better resolution than surface seismic surveys and could identify lithological layers more distinctly (Stewart and Disiena, 1989).

VSP processing also gives insight to eliminating multiples. The processing of zero offset VSP, for instance, leads to the process of corridor stacking. Corridor stacking extracts a small mute window of upgoing wavefield data around the first breaks that contains the primary reflections. This is because upgoing multiples do not make it all the way to the first break times (to all receivers). This small mute window is extracted to give the ideally multiple free outside corridor stack and what is left is considered the inside corridor stack holding the rest of the reflections and multiples if they exist. Comparing the outside versus inside corridor stacks highlights any significant multiples in the data which inturn would help in their elimination (Hinds et al., 1999 and Campbell et al., 2005).

VSP surveys can be utilized in several petroleum applications. VSP data can help in side-track drilling and help in determining the exact depth of a formation using time to depth relations (Stewart and Disiena, 1989). This is because VSP data can be used to laterally image the subsurface (Hardage, 1983). In addition, VSP surveys are used to predict rock properties ahead of the drill bit. If the downgoing and upgoing wavefields below the well total depth are known, seismic reflectivity is used to invert for seismic impedances which are related to rock type, porosity and pore pressure (Hardage, 1983).

Also, VSP data can help interpret zones of overpressure and therefore drillers can avoid overpressure problems (Stewart and Disiena, 1989 and Campbell et al, 2005).

The purpose of acquiring different VSP surveys depends on the goal of the survey. A zero offset VSP survey can provide information about the time-depth conversion, normal incidence reflectivity and interval velocities in depth. On the other hand, a multi offset VSP survey could be used for AVO analysis (Stewart, 2001).

1.2 Geological background of study area

A zero offset and three walkaway multi length VSP surveys were acquired to investigate fractured lower Cretaceous coals in southern Alberta. These fractures, better known as face and butt cleat fracture systems, are permeability conduits for methane production. The face cleats help propagate the gasses to the wellbore because of their continuity while the butt cleats propagate the gas to face cleats (Richardson, 2003, Alduhailan, 2008). Studies show that coals should be less than 1200 m deep or at least 2000 m deep to prevent the sealing of cleats in the coals (Richardson, 2003; Ayers, 2002).

In general, the amount of methane gas within porous coal systems is larger than that of conventional gas around the world. However, most of the coal bed methane (CBM) systems have not been produced (Bell and Bachu, 2003). The coals are mostly self sourcing but some have gas which has migrated from some other formation. Contained or migrated gas in the coals can be thermogenic, biogenic or a mix (Ayers, 2002). Coals have to be in a high enough rank to contain methane (Richardson, 2003). Other factors that affect gas storage include moisture, gas composition and pressure. Most of the methane gas exists in a primary state in the mircopores of the coal. It also exists in a secondary state adsorbed in the micropores of the fracture matrix or in water (Ayers, 2002). Figure 1.2 shows a stratigraphic sequence of coal bearing formations in Alberta. The target zone of this thesis is the Mannville B coals that are located in the lower Cretaceous Mannville Group. Figure 1.3 shows the dominant stress direction in the Western Canadian Sedimentary Basin.

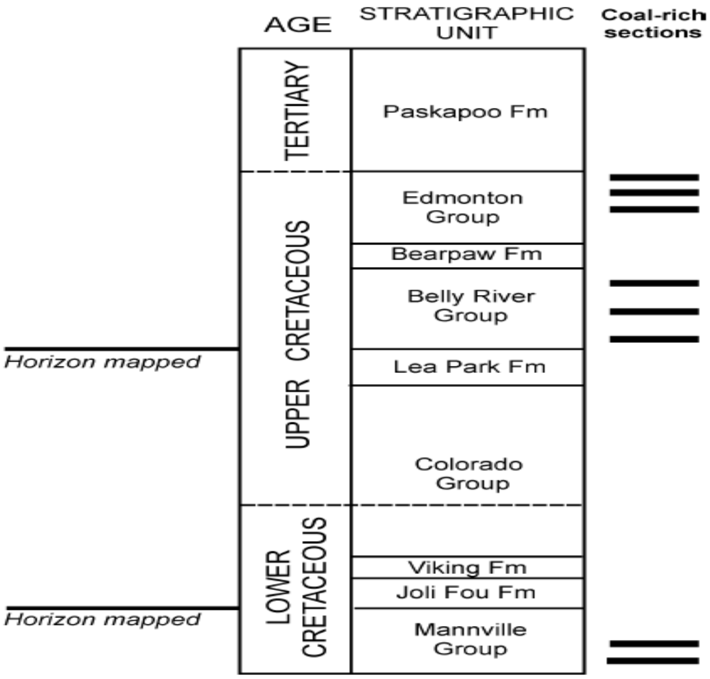

Figure 1.2: Stratigraphic geological sequence of coal bearing formations in Alberta (Bell and Bachu, 2003).

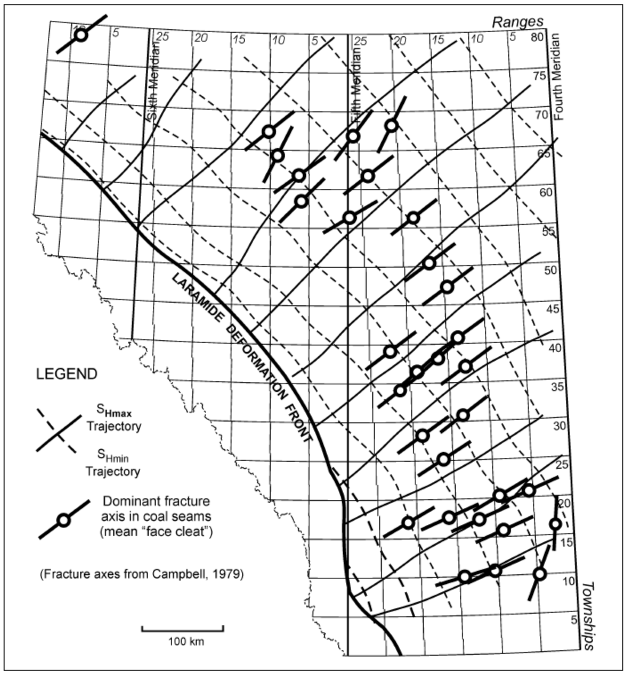

Figure 1.3: The maximum stress direction is NE-SW which is parallel to the face cleats (Bell and Bachu).

Figure 1.2 highlights the major coal bearing formations in Alberta. As mentioned previously, the target of this thesis is the Mannville B coal that exists within the lower Cretaceous Mannville Group. Other coal deposits are located in the upper Cretaceous Horseshoe Canyon Formation of the Edmonton Group, the upper Cretaceous Belly River and the upper Cretaceous to Pliocene Paskapoo Formation (Bell and Bachu, 2003).

Figure 1.3 shows the regional stress in the lower Cretaceous coal seams. Studies have shown that the lowest regional stress is inversely related to permeability and is mostly horizontal in Western Canada. The horizontal stress was obtained through micro-fracture testing taken from 50 wells in the area where a fracture was initiated and then opened and closed several times to obtain a closure pressure that is related to the smallest principle stress acting on it. If this pressure is lower than the overburden vertical pressure, then the smallest horizontal stress is the calculated result. Other methods of determining stress include mini-fracture analysis, leak off analysis and fracture breakdown pressures (Bell and Bachu, 2003). Ultimately (Bell and Bachu, 2003) conclude that their study infers that the most permeable vertical fractures for methane flow in the coals are aligned to the plane perpendicular to the regional lowest principle stress. This regional trend is in the northeast to southwest direction.

1.3 Thesis outline and goal

The goal of this thesis is to investigate the possibility of the existence of methane gas in the Lower Cretaceous Mannville B coals. This goal is to be achieved after evaluating the attributes of Amplitude Variation with Offset (AVO) of the processed VSP surveys. The target coals are 11 meters thick and located at depth 1423 meters total vertical depth.

Several steps were taken to reach the thesis goal which will be explained throughout this thesis. The procedures and studies included in this thesis are:

- Describe the acquisition and processing of the zero offset VSP survey and evaluate the result compared to synthetics generated from well logs acquired in the same VSP well.
- Describe the acquisition and processing of the three walkaway VSP surveys and generate angle gathers for each VSP walkaway survey.
- AVO attribute studies are performed on the walkaway angle gathers that are then related to rock properties for further analysis of the possibility of having methane coals in the Mannville B Coals.

The zero offset VSP and all three walkaway VSPs are processed using VISTA, a processing software package developed by GEDCO. In addition, the well logs and AVO analysis will be analyzed using ELog and STRATA packages of the Hampson-Russell software.

1.4 Thesis structure

The structure of the thesis includes four chapters and two appendices. Chapter 1 provides an introduction to VSP surveys and the possible applications and advantages for performing VSP surveys. The chapter also provides the goal of the thesis and steps that will be performed to achieve it. Chapter 2 deals with the acquisition and processing of the zero offset VSP survey and evaluate the results of stacking with a synthetic seismogram generated from the log data. Chapter 3 describes the acquisition and processing of the three walkaway VSP surveys. These walkaway surveys are all processed with the same flows to obtain walkaway angle gathers that will later be assessed for AVO analysis. Chapter 4 analyzes the existence of methane gas in the Mannville B coals through AVO crossplots and by inverting for impedances that are related to rock properties that help in the assessment. Chapter 5 states the conclusions and recommendations arrived by in this thesis. Appendix A includes the east walkaway raw three component data to show how these components compare and how these components behave with increase offset. Appendix B shows the calculation of the angles of incidence for the lowest four receivers in the walkaway VSP surveys. These calculations are used to convert the offsets of the offset gathers obtained from the VSP data to angle gathers.

CHAPTER 2: ZERO OFFSET VSP ACQUISITON AND PROCESSING

2.1 Introduction

VSP surveys have some distinct advantages over surface seismic surveys. One key advantage is the ability to separate the downgoing (direct) and upgoing (reflected) wavefields that enable the calculation of true reflection amplitude or seismic impedance (Hinds et al., 1999). The results of the calculation permit the correlation between well logs and surface seismic on one hand with the VSP result in the other (Stewart and Disiena, 1989). Of course, VSP data have enhanced high frequency content because waves travel through the near surface low velocity level only once. This may help in the detection of reflectors not seen on the surface seismic data. Also, another key advantage of VSP is the ability to identify multiples and can help eliminated inter-bed multiples on both VSP and surface seismic data (Parker and Jones, 2008).

2.2 Acquisition of zero offset VSP

The acquisition parameters used for the zero offset VSP is listed in table 2.1.

Table 2.1: Acquisition parameters for the zero offset VSP (modified from Parker and Jones, 2008).

Acquisition Parameters	Zero offset VSP
Source	Two Vibroseis Trucks
Source offset	62 m
Receiver tool	16 shuttle tool with 3C receivers
Receiver separation	15.1 m
Acquisition depths	48.7 - 1420 m
Vibroseis frequency	8 - 120 Hz
Vibroseis sweep	12 s
Kelly Bushing elevation (MSL)	872.2 m
Datum elevation or ground level (MSL)	868.1 m

Table 2.1 explains the geometry of the zero offset VSP. The source offset explains that the position of the source is 62 meter away from the borehole that contains the VSP receivers. The receiver tool contains 16 shuttles with three component receivers indicating that the tool has 16 levels of receivers separated by 15.1 meters with each receiver containing two horizontal components and one vertical component. The two horizontal components are used to polarize the horizontal energy towards the source and the vertical component polarizes the wavefield in the plane of the source and well. The sources of the zero offset VSP survey are two vibroseis trucks. A vibroseis truck is a common seismic source used to shake the ground in order to generate seismic waves with a certain bandwidth. Vibroseis trucks are preferred to dynamite sources in some cases where a specific bandwidth is desired and can be performed as a sweep where frequencies can start low and increase with time (Kalinski, 2007). The frequency

bandwidth for this specific zero offset VSP survey runs from 8-120 Hz produced over a sweep of 12 seconds. The term Kelly Bushing refers to a rotary table that rotates the drill string and is sometimes referred to in oil field drilling for a reference depth (Schlumberger Oilfield Glossary). The ground level is considered the datum to which the VSP is referenced.

After acquisition the zero offset VSP is ready for processing. A generalized zero offset VSP processing flow is taken and modified from (Coulombe, 1993) and displayed in Figure 2.1.

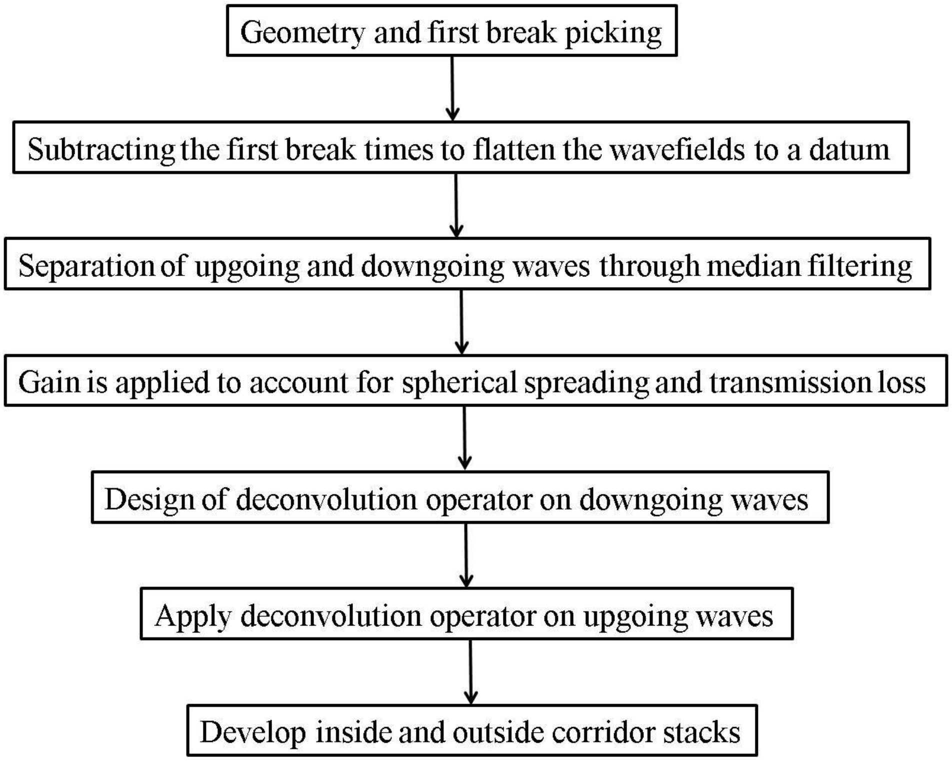

Figure 2.1: Generalized zero offset VSP processing flow (Taken and modified from Coulombe, 1993).

The following sections will explain the zero offset VSP processing procedure in more detail.

2.3 Geometry and first breaks

As described in the acquisition section, the receivers in the borehole contain two horizontal components and one vertical component. The two horizontal components are named X and Y while the vertical component is named the Z component. The X and Y components rotate randomly in the borehole since there is no control over their direction. The two horizontal components need to be polarized and corrected for this rotation effect. The correction will take place with hodogram rotations later in this chapter.

The geometry of the zero offset VSP has been set with channel numbers 1, 2, 3, corresponding to X, Y and Z and assigned with Trace Code ID of 1, 3 and 2 respectively. The first break times are picked on the raw vertical Z component shown in Figure 2.2. Figure 2.2 also highlights the Mannville coal reflection of interest and the dominant downgoing waves. The Z components displayed in Figures 2.2 is displayed with Automatic Gain Control (AGC). AGC is a statistical amplitude adjustment applied to the traces for better visual aid. A temporal window is determined, in this case 500 milliseconds, where the root-mean-squared amplitudes in the window is computed and an amplitude model is computed. The resulting trace is computed by dividing the original trace by the modeled trace (Margrave, 2008). Since this is a vertical well, the downgoing P waves in the zero offset survey dominate the energy of the wavefields. The X and Y components, with first breaks displayed, are shown in Figure 2.3 and Figure 2.4 respectively. The dominance in the downgoing and upgoing P waves is clear in the Z component compared to the X and Y components.

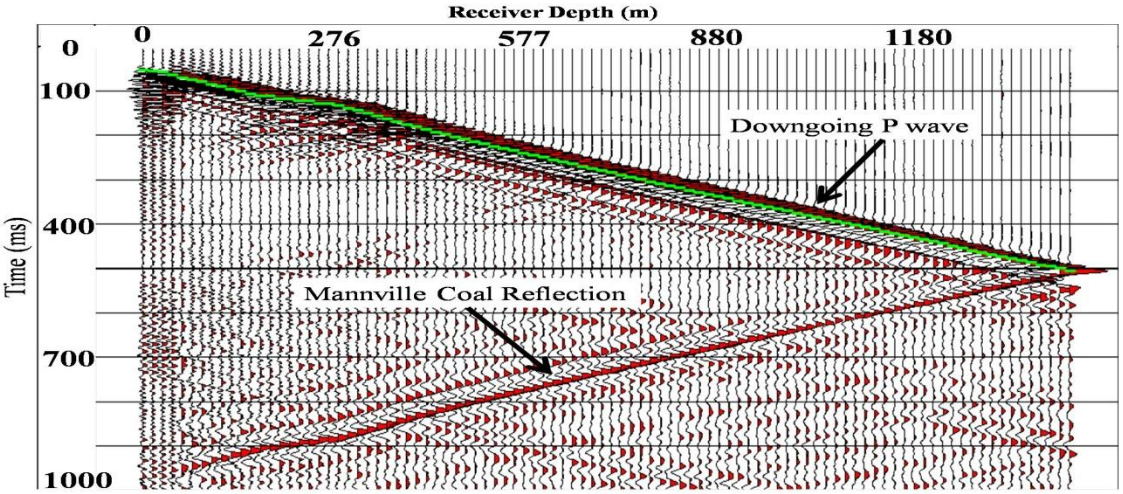

Figure 2.2: Raw zero offset VSP Z component with first break times (green) and AGC.

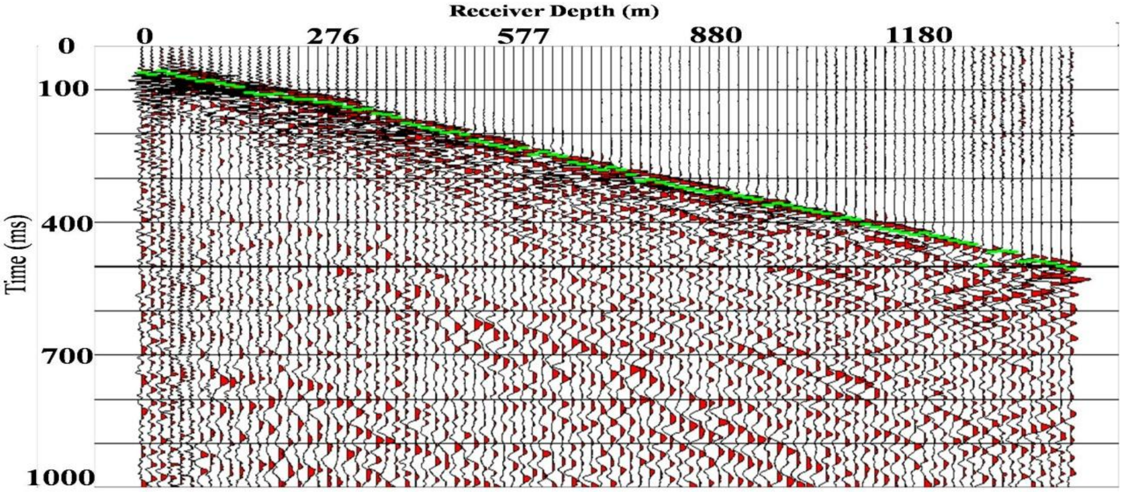

Figure 2.3: Raw zero offset VSP X component with first break times (green) with AGC.

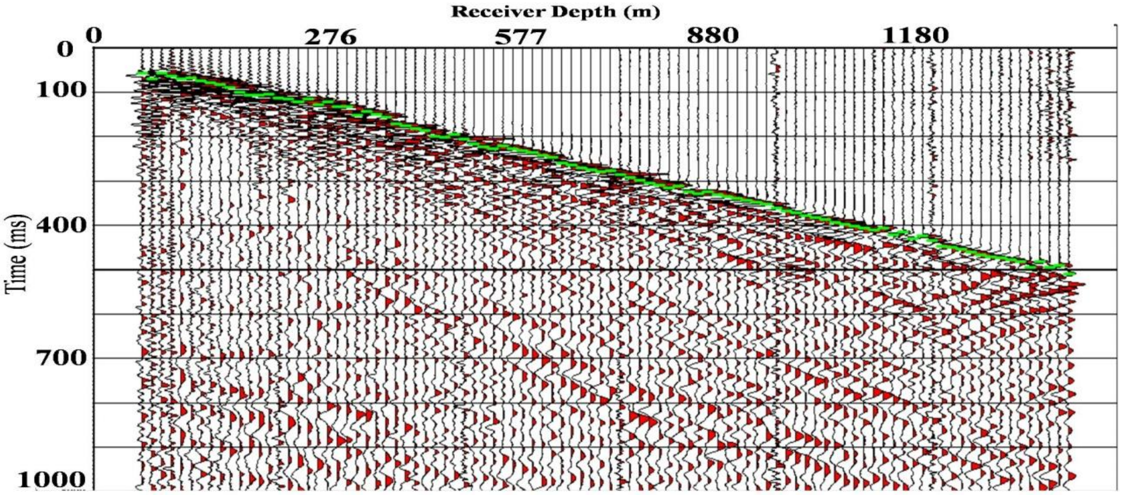

Figure 2.4: Raw zero offset VSP Y component with first break times (green) with AGC.

For the zero offset VSP, the processing was focused only on the raw vertical Z component. It is apparent from the X and Y component figures that there is not enough upgoing energy to be processed. According to (Hardage, 1983) the vertical component measures the vertical particle motion while the horizontal components measure the horizontal particle motion. Knowing that the source is a P wave generating vibroseis truck and relatively close to the borehole, most of the wavefield particle motion will affect the vertical component since the particle motion is in the direction of wave propagation. Therefore, the horizontal components do not contain enough energy to process at near offsets.

The first breaks were picked and the interval velocities were calculated and displayed in Figure 2.5. These interval velocities calculated from the zero offset first breaks are essentially a 1D velocity model that will be used later in walkaway VSP processing. The interval velocity is a special kind of average velocity for a specified interval expressed as (Margrave, 2008):

$$V_{aveint}(\tau_0, \tau_2) = \frac{1}{\tau_2 - \tau_0} \sum_{k=1}^{n} V_k \Delta\tau_k$$

Where:

$$\tau_2 - \tau_0 = \sum_{k=1}^{n} \Delta\tau_k$$

Is the total travel time across the interval. Also V_k here is the average velocity across the k interval and $\Delta\tau_k$ is the traveltime across the interval.

The root-mean-square velocity (V_{rms}) is expressed as follows (Sheriff, 1997):

$$V_{rms}^2 = \frac{\sum_i V_i^2 t_i}{\sum_i t_i}$$

Where V_i and t_i are the velocity and time across an interval. The assumptions behind V_{rms} are that layers are assumed to be horizontal and the velocities can be approximated by straight lines (Sheriff, 1997). The advantage of using V_{rms} is that we can approximate the change of velocity with depth by assuming a replacement medium that has a constant velocity replacing the subsurface layers that the waves propagate in (Margrave, 2008).

The interval velocity is related to the root-mean-square velocity (V_n) as follows (Dix, 1955):

$$V_n^2 = (V_{An}^2 \sum_1^n \Delta T_i - V_{An-1}^2 \sum_1^{n-1} \Delta T_i)/\Delta T_n$$

Where V_n is the V_{rms} velocity and t_n is the zero offset arrival time to the nth reflector (Sheriff, 1997). Furthermore, V_{An} is the average interval velocity of the layer (Dix, 1955).

The shallowest of the interval velocities are the near surface velocity which is calculated by dividing the depth of the first receiver, 48.7 m, by the first break time of the first receiver, 0.0522 s and rounded to 950 m/s.

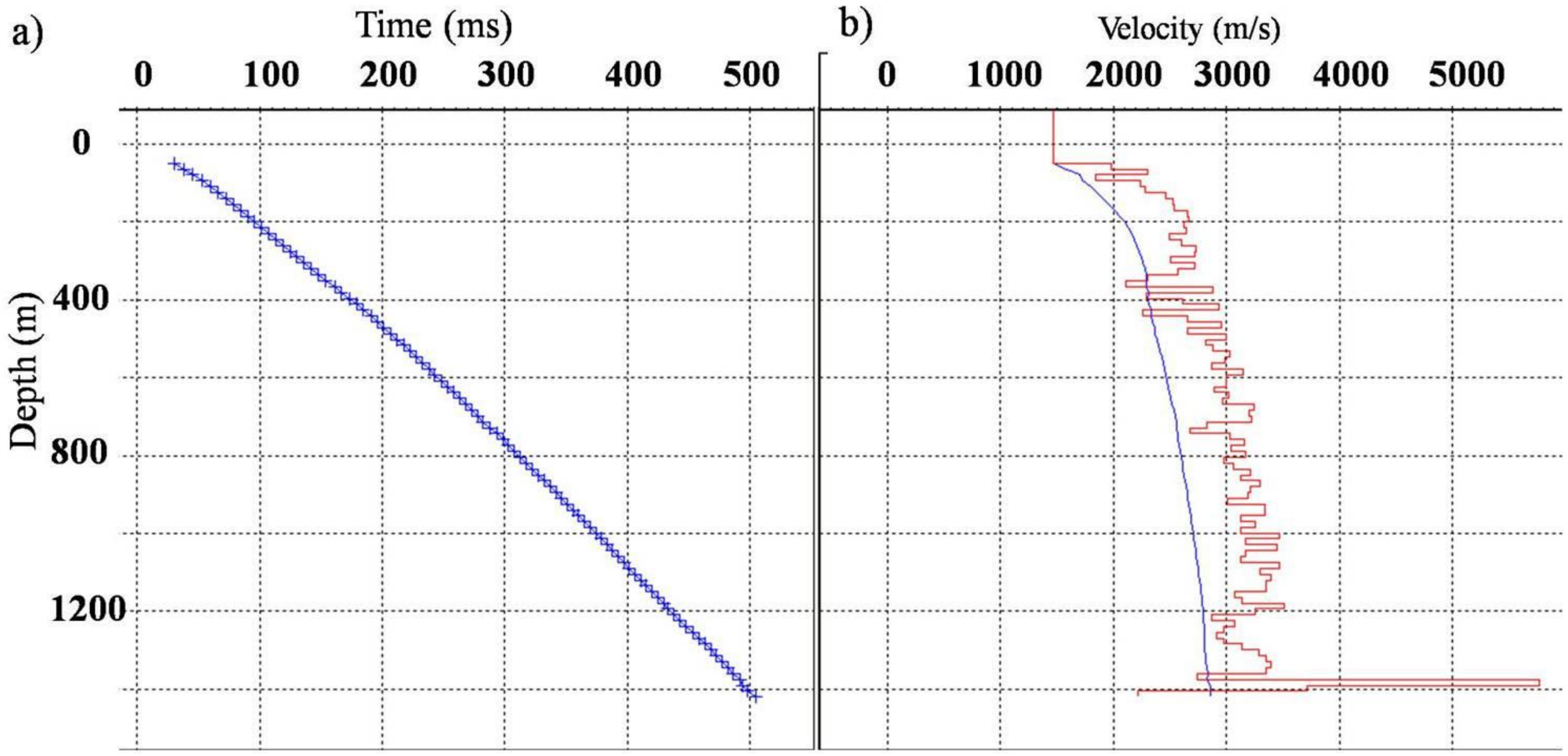

Figure 2.5: Zero offset velocity model calculated from the first breaks. a) shows the first break times of the raw vertical Z component plotted against depth (blue). b) shows the corresponding interval velocities in red with RMS velocity in blue.

2.4 Median filtering

The next major processing step was to separate the downgoing from upgoing wavefields. Figure 2.6 shows the flow used for wavefield separation.

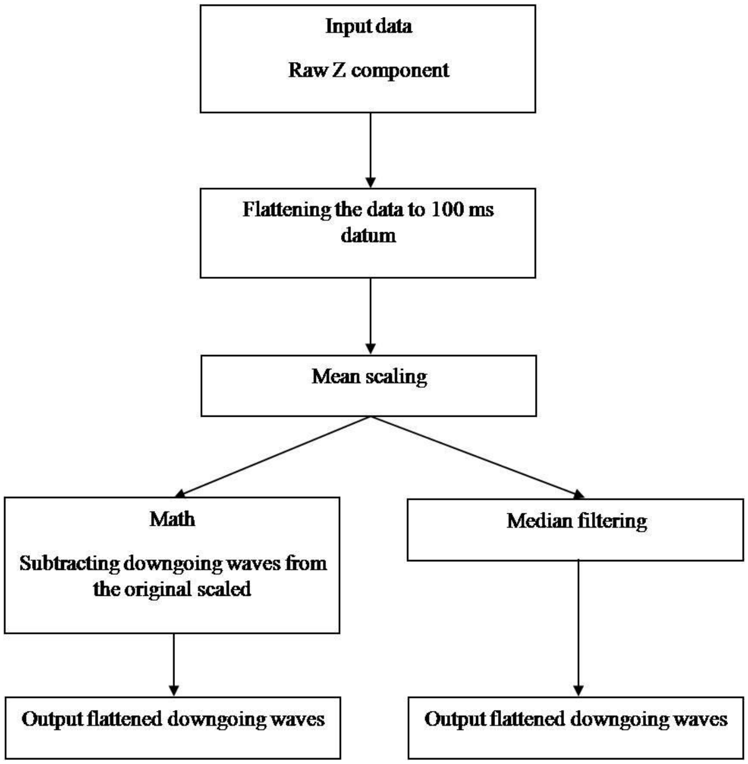

Figure 2.6: Wavefield separation flow for zero offset VSP.

Median filtering is the method that I chose to separate the wavefields and tested different lengths of median filtering, which consist of 9, 11, 13, 14, 15, 19 and 21 median point filter. In median filtering, the traces of a selected window are organized in ascending amplitude. The median is the trace representing (N+1)/2 where N is the number of traces and is odd. If N is even, then the median is the average of the middle two traces. The median is then taken for the median window of traces selected and the window is then incremented to the next range of traces (Hardage, 1983 and Hinds et al, 1999). Figure 2.6 explains the flow of median filtering. The raw Z component is considered the input to the flow. This raw Z component is then flattened to a 100 ms datum by subtracting the first break times from each trace. The flattened raw Z component is shown in Figure 2.7. Next, mean scaling is applied by calculating a scale for each trace sample and multiplying it by the trace (VISTA help). The mean scaling is applied in a specified window of 95 – 105 ms to cover the first break only. Mean scaling is intended to enhance the first break amplitudes before separation. After applying a 21 point median filter, the downgoing waves are preserved and the upgoing waves are eliminated from the data. Subtracting the flattened downgoing waves from the original flattened raw Z component gives the flattened upgoing waves.

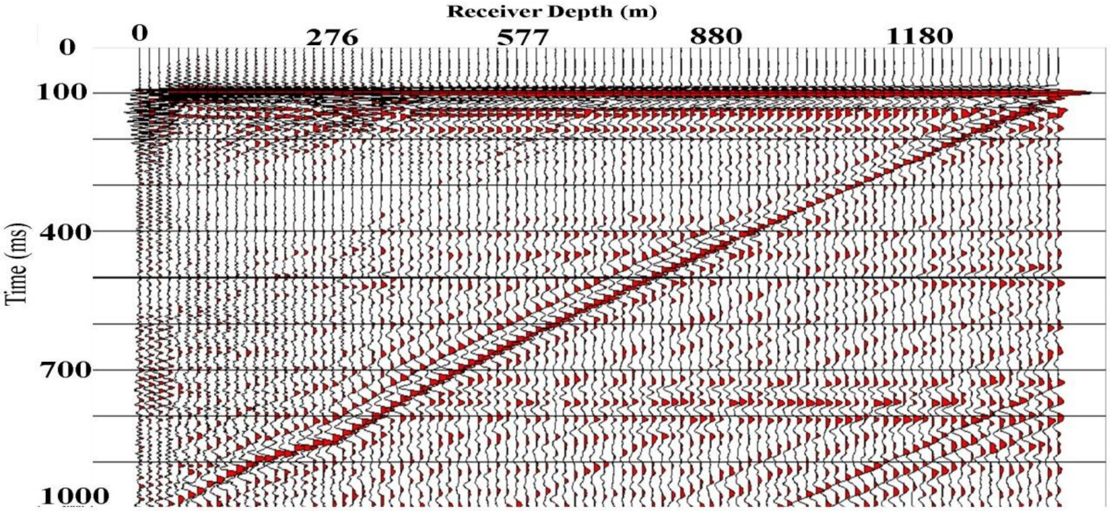

Figure 2.7: Flattened zero offset raw Z component with AGC. Flattening was applied by subtracting the first break times from each trace.

The assessment of the effect of median filtering was initially analyzed on the upgoing waves. The median filters did not have a distinct effect on upgoing waves, therefore the analysis was mainly based on the isolation of the downgoing waves. A 21 point median filter was applied and proved to best isolate the downgoing waves and showed the most continuous and coherent downgoing events while eliminating the upgoing waves. The first four traces of the median filtered 21 point median filter flattened Z component were deleted because of noise. Figure 2.8 shows the downgoing Z wavefield after applying a 21 point median filter with 500 ms Automatic Gain Control (AGC). Figure 2.9 shows the resulting upgoing Z wavefield after subtracting the downgoing waves from the original flattened Z wavefields and adding the first break times again shown with -9 dB applied to the amplitudes.

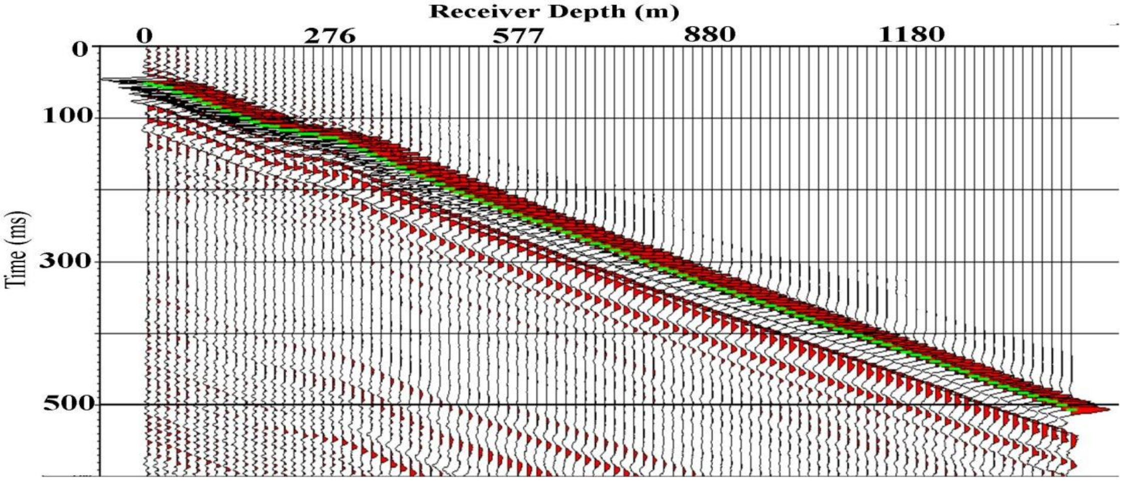

Figure 2.8: Downgoing wavefield after 21-point median filter. AGC applied for display.

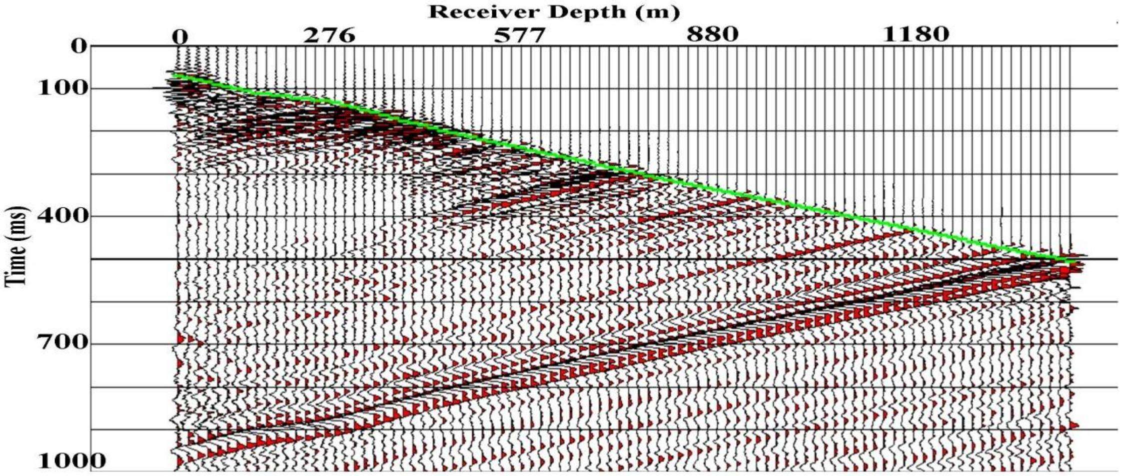

Figure 2.9: Upgoing wavefield after 21-point median filtering and subtracting the downgoing going waves from the original wavefield. A scale of -9 dB is applied for display

2.5 Deconvolution

The next step was to deconvolve the data using the downgoing direct wavefield, that represents the source signature, and applying it to the upgoing wavefield. A division of upgoing frequency spectrum waves over downgoing frequency spectrum of waves in the FK domain creates a zero phase multiple free wavefield (Hinds et al, 1999). Figure 2.9 shows the deconvolution flow.

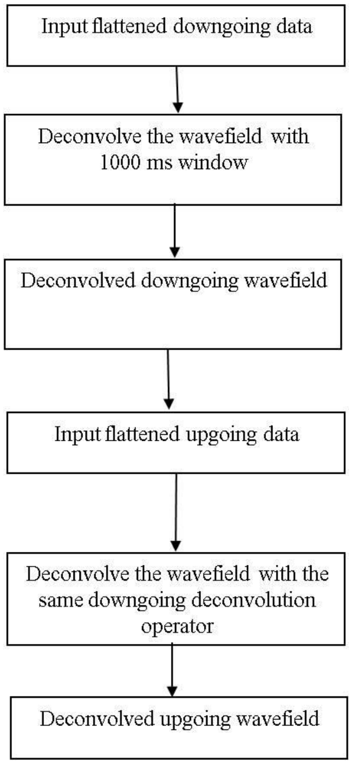

Figure 2.10: Deconvolution flow for the zero offset VSP survey.

The first part of the deconvolution flow has the downgoing Z flattened wavefield after 21 point median filtering applied to it to optimize the deconvolution parameters. The deconvolution windows started at 0 ms and extended to 1000 ms. This wide window is chosen because the data was found to not contain significant multiples within it. The same deconvolution operator applied to the downgoing wavefield is to be applied to the upgoing Z wavefield. The result gives the deconvolved upgoing Z flattened wavefield. Figure 2.11 shows the deconvolved downgoing wavefield while Figure 2.12 shows the deconvolved upgoing wavefield.

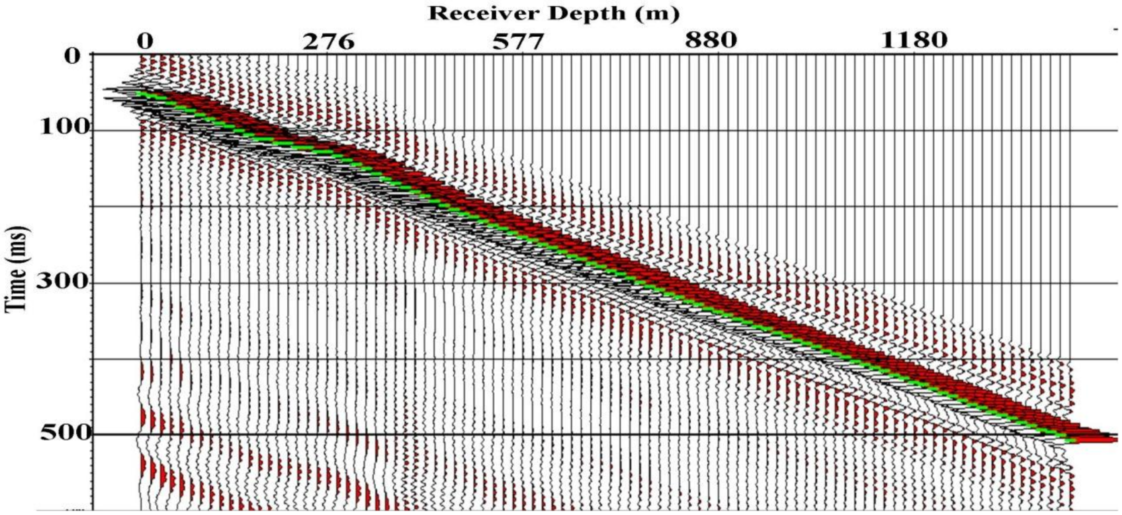

Figure 2.11: The deconvolved downgoing Z(+TT) after 21 point median filtering.

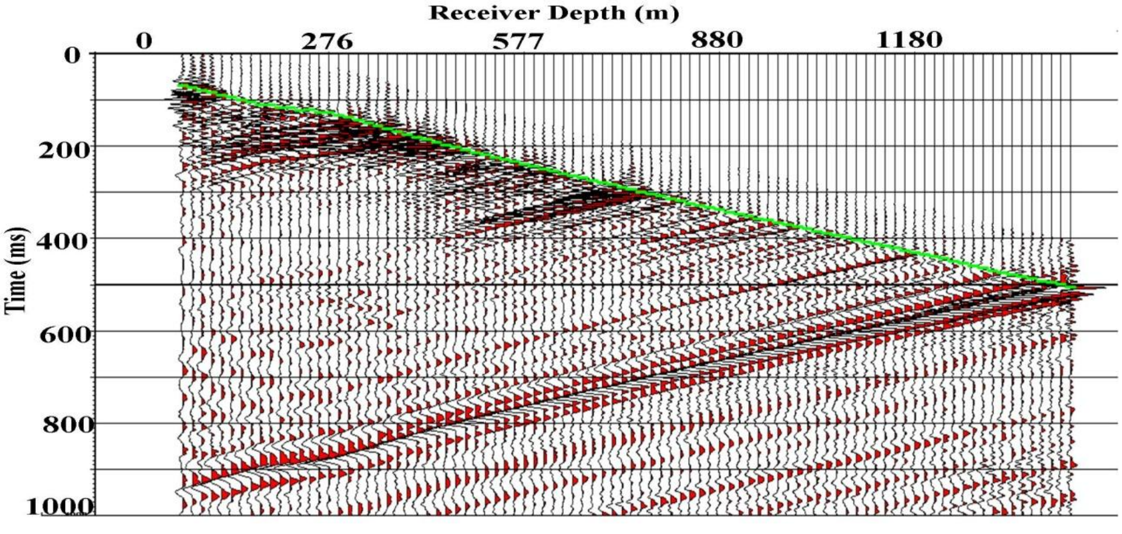

Figure 2.12: The deconvolved upgoing Z(+TT) after 21 point median filtering.

After deconvolution, the upgoing and downgoing events are sharper and better defined. The deconvolution process appears successful because no significant multiples are apparent in the upgoing and downgoing wavefields. To insure this successful deconvolution result, the amplitude spectrum of one of the upgoing wavefield traces along with the average amplitude spectrum of the entire upgoing wavefield is shown before and after deconvolution in Figures 2.13 and 2.14 respectively.

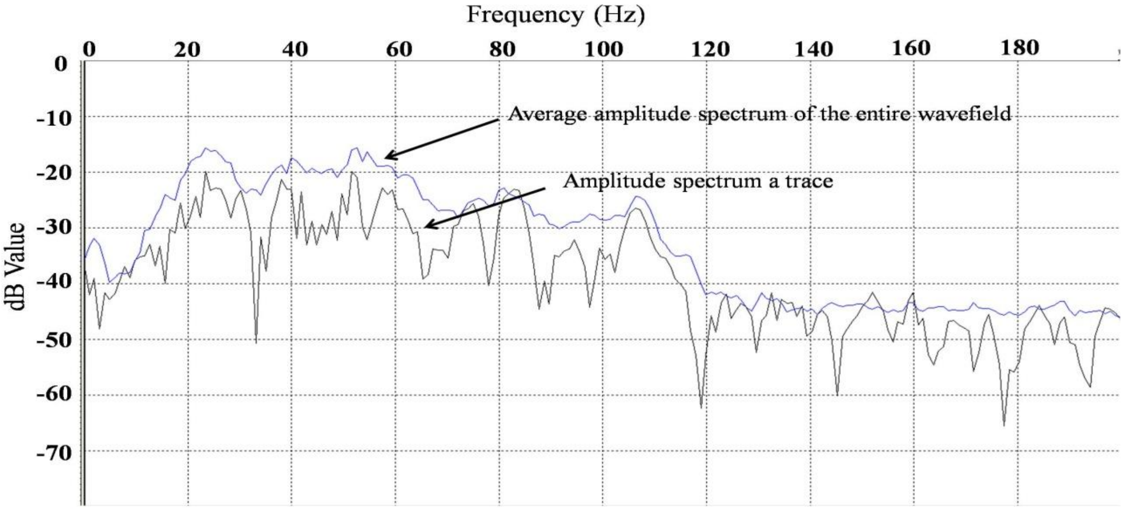

Figure 2.13: Amplitude spectrum of the upgoing wavefield before deconvolution.

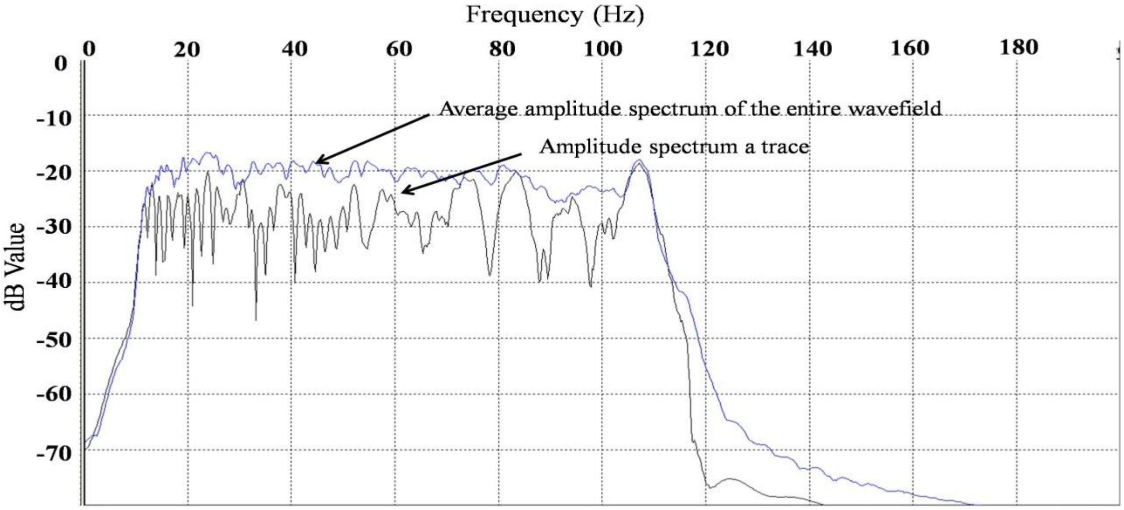

Figure 2.14: Amplitude spectrum of the upgoing wavefield after deconvolution.

The amplitude spectrums vary in result before and after deconvolution. It is apparent that before deconvolution, in Figure 2.13, the amplitude spectrums start off high in amplitude and decay with increasing frequency. On the other hand, Figure 2.14 shows the amplitude spectrums having an average white reflectivity over the range of frequencies. The point of deconvolution is to remove the effect of the wavelet to obtain a seismic reflectivity which is generally believed to be a white reflectivity series (Margrave, 2008). Figure 2.14 shows that the deconvolution operator did a good job in gaining a white reflectivity especially when comparing the overall average amplitude spectrum of the entire upgoing wavefield before and after deconvolution.

2.6 Corridor stacking

Now that the data is deconvolved, the need to develop inside and outside corridor stacks is pursued. The flow that illustrates the creation of corridor stacks is illustrated in Figure 2.15. The input data to be stacked is the deconvolved median filtered upgoing Z wavefield, which then has an exponential gain applied to it to account for spherical spreading and transmission losses. The Z wavefield is converted back to Field Record Timing (FRT) by adding the first breaks to every trace before the application of Normal Moveout (NMO) correction. NMO is normally applied to seismic data to map the trace recorded at a certain offset to what it would be if it was recorded at zero offset. The NMO correction uses the interval velocities calculated earlier, from first breaks of the zero offset raw Z component, to ensure that events are located at their proper times. The NMO-corrected data was then converted to two-way-time by multiplying the first break times by two. This produces the first output of the upgoing Z that is in two-way-time and NMO corrected displayed in Figure 2.16. The result is then bandpass filtered to limit noise. The two way time and NMO corrected Z upgoing wavefield is median filtered with 4 point median filtering to enhance the signal to noise ratio. Furthermore the data is bandpass filtered once more. Then the result is converted back to field record time, corridor muted and converted back to two way time to produce an inside corridor mute and an outside corridor mute. A corridor mute of 50 ms and to a depth of 1220 m is applied to the corridor muted data. The outside and inside corridor mutes are in Figures 2.17 and 2.18 respectively.

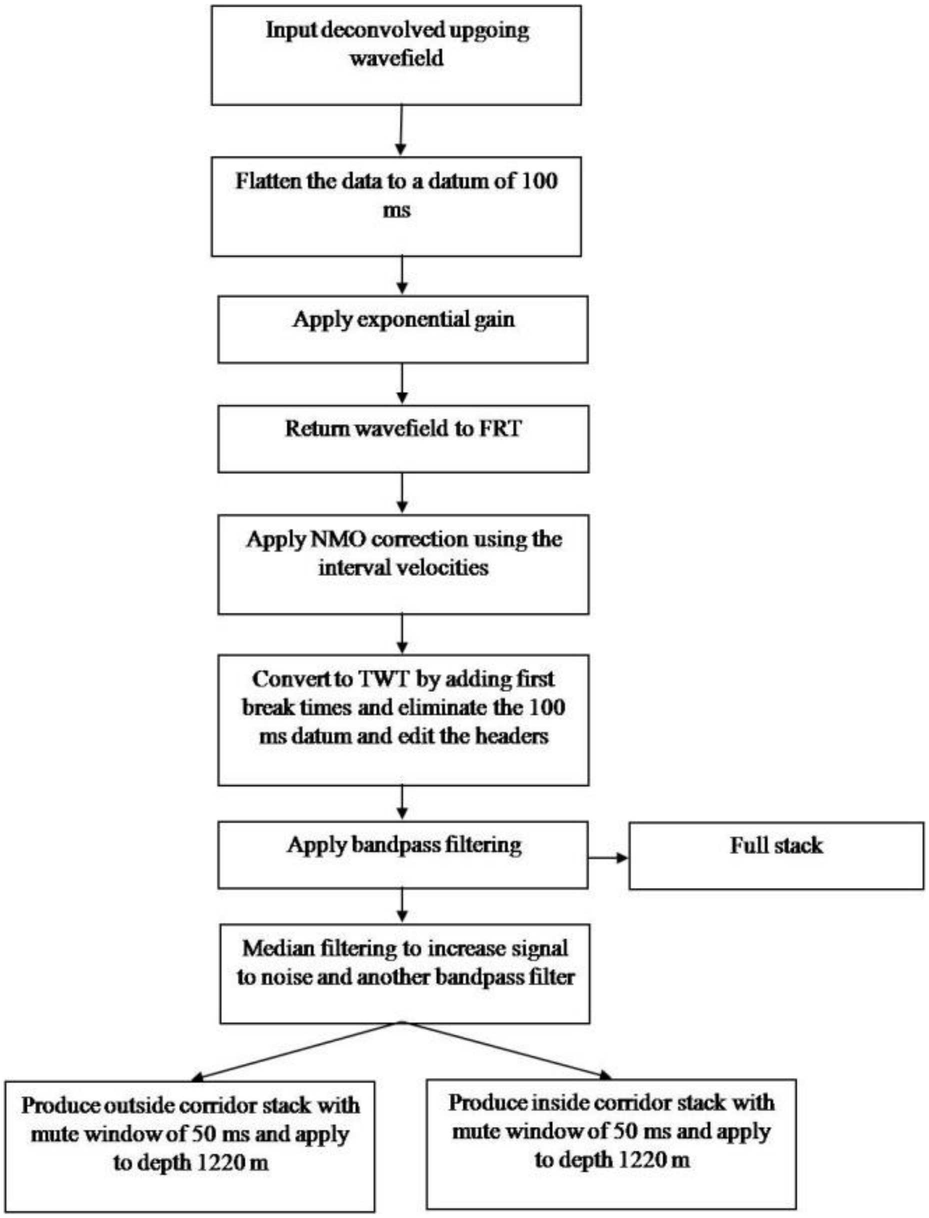

Figure 2.15: Outside and inside corridor flow for zero offset VSP data.

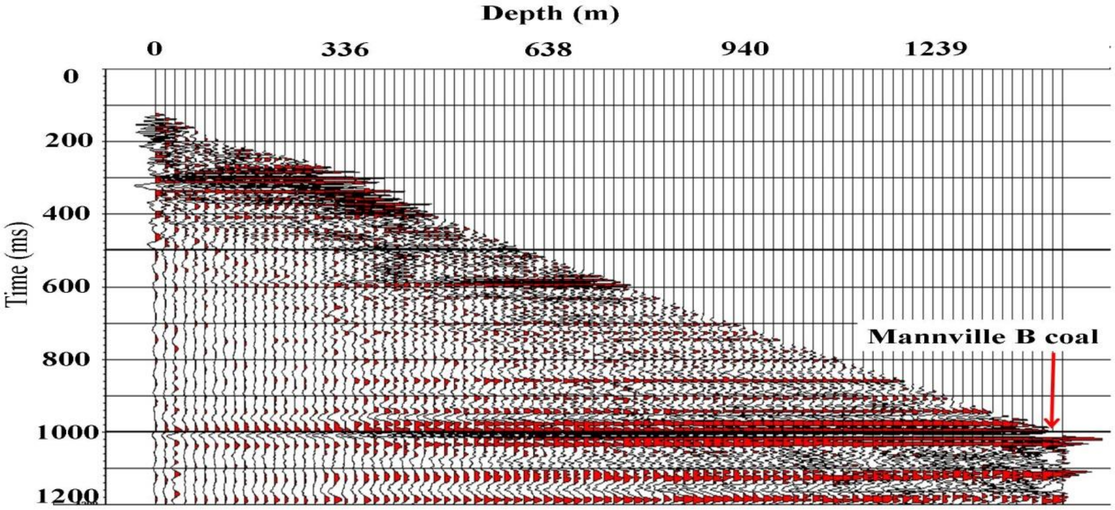

Figure 2.16: The two way time upgoing Z wavefield.

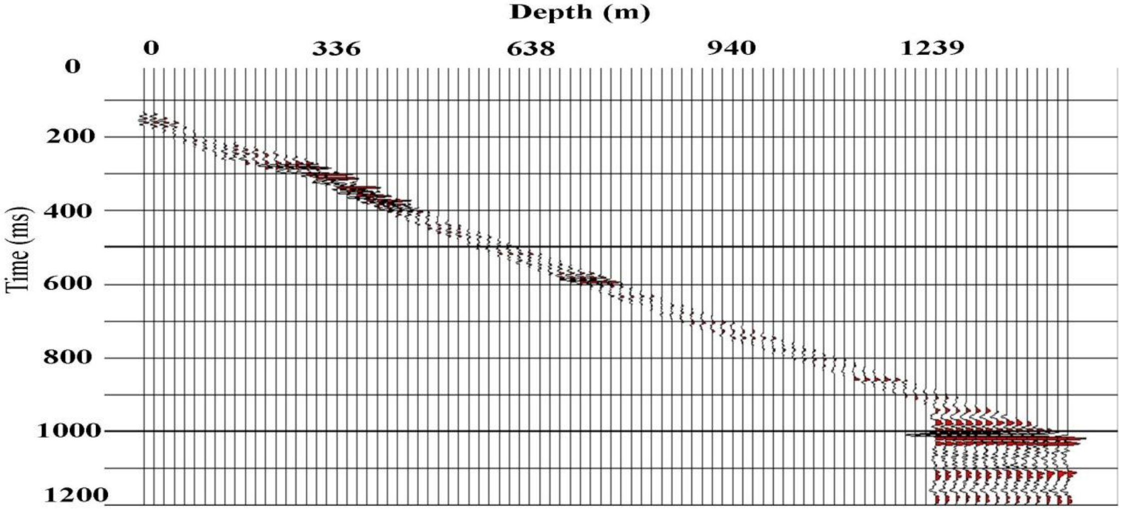

Figure 2.17: The 50 ms outside corridor mute with AGC applied for display.

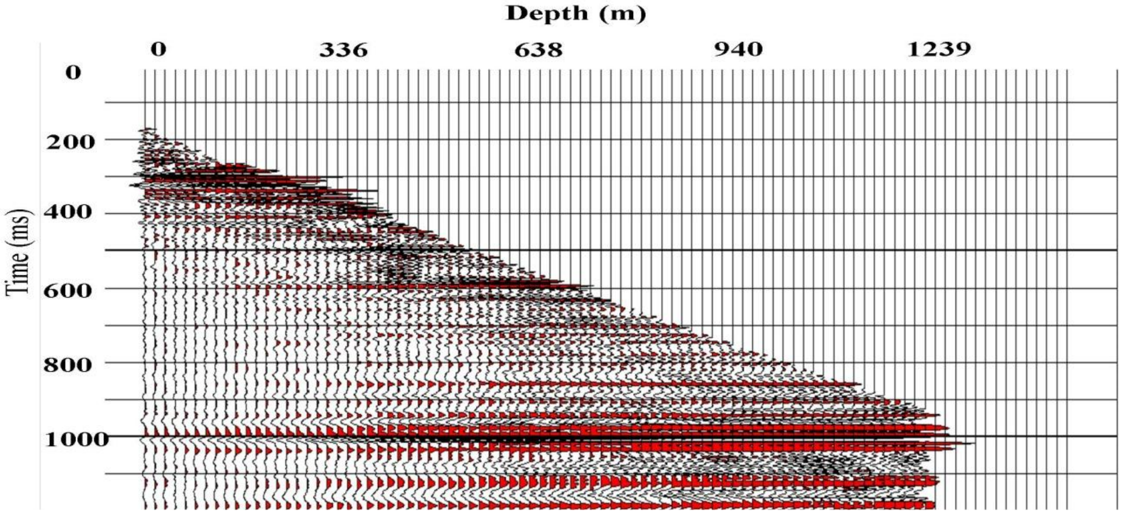

Figure 2.18: The 50 ms inside corridor mute with AGC applied for display.

Figures 2.17 and 2.18 show the outside and inside corridor data after applying the mute of 50 ms to the two way time upgoing Z wavefield. These two mutes are to be stacked and compared in order to assess if multiples do exist in the data. The result of stacking both mutes and repeating the trace 10 times for display purposes is displayed in Figure 2.19.

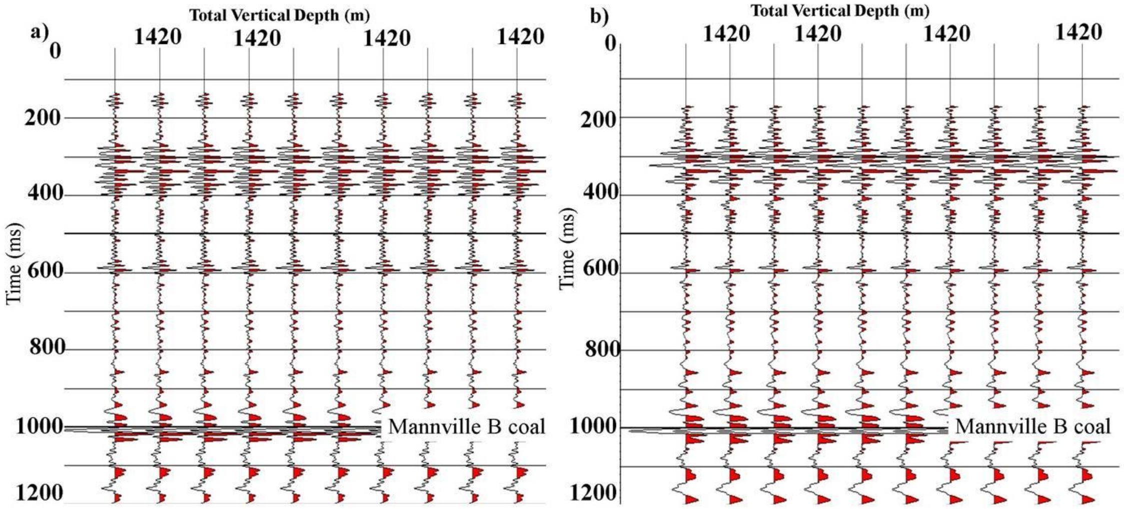

Figure 2.19: The left shows in outside corridor stack and the right shows the inside corridor stack.

The outside and inside corridor stacks show no significant differences which implies that there are no significant multiples in the data. In order to assess the width of the mute window, additional outside corridor stacks were generated with window lengths of 30 ms, 40 ms, 60 ms, and 70 ms in addition to the original 50 ms window. These corridor stacks are shown in Figure 2.20.

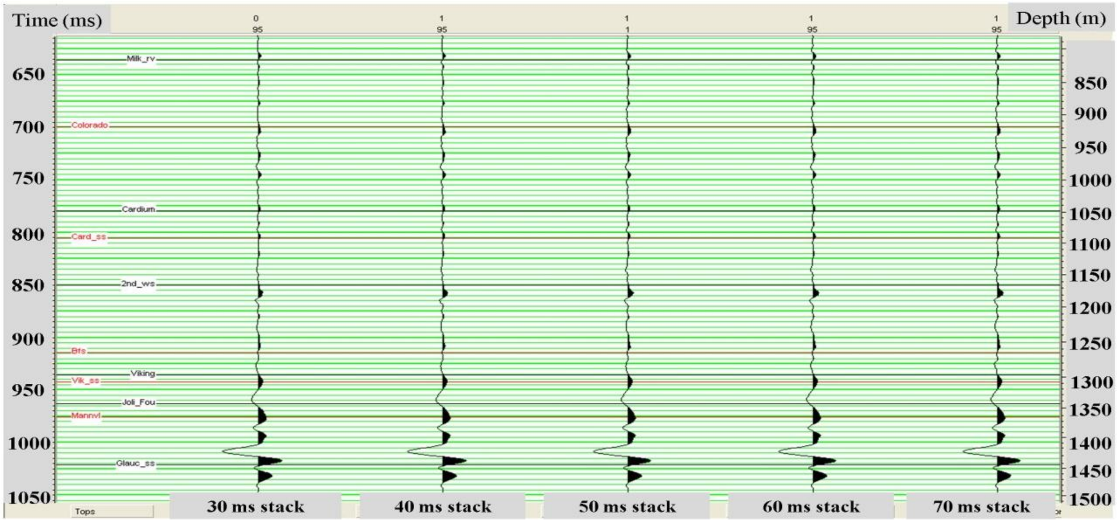

Figure 2.20: Zero offset VSP outside corridor stacks. From left to right: corridor stacks with mute windows 30 ms, 40 ms, 50 ms, 60 ms and 70 ms.

Analyzing the outside corridor stack, I deduced that there are no significant differences in increasing the length of the corridor mute between 30 to 70 ms. This indicates that either the deconvolution eliminated all significant multiples and therefore these selected mutes do not contain anything that might affect their amplitudes or the mutes are not wide enough to include any multiples. In any case, the object of the outside corridor mute is to contain only primaries, which is what I consider is achieved.

2.7 Wireline logs and comparison

Wireline logs from the VSP well were obtained and utilized to generate synthetic seismograms in this section. A sonic log, density log and gamma ray log were acquired from 252 m depth to 1464 m depth, starting just above the Edmonton Fm and ending below the Mannville Fm. The logs mentioned above are displayed in Figure 2.21 along with the computed impedances and reflectivity from the log data.

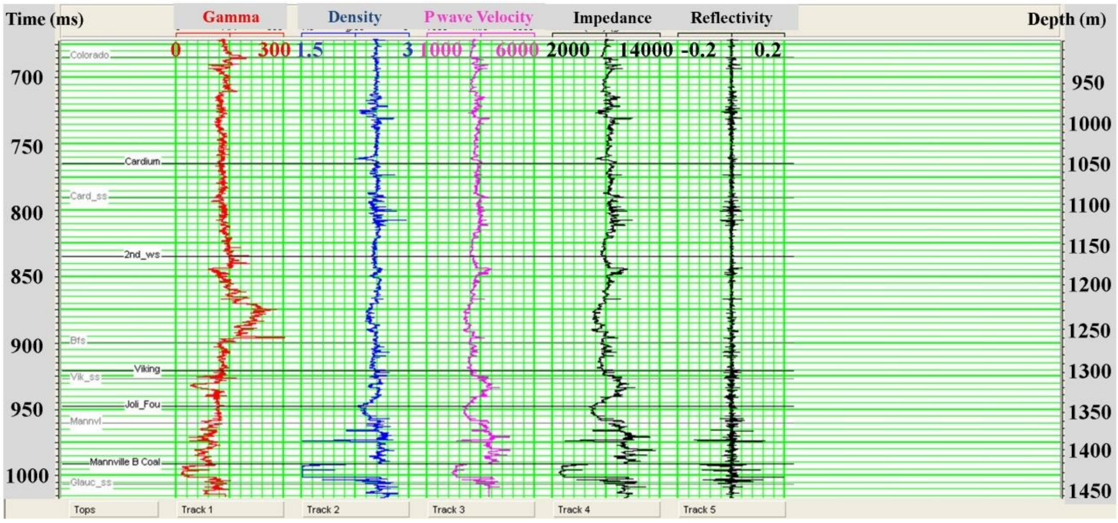

Figure 2.21: The wireline logs acquired in the VSP well are shown. From left to right: formation tops, gamma ray log (red), density log (blue), P wave velocity (magenta), computed impedance (black) and computed reflectivity (black).

As described in Chapter 2, the VSP outside and inside corridor stacks were obtained using a 50 ms corridor mute window. The outside corridor stack was used to determine a wavelet to convolve with the reflectivity computed from the logs in order to obtain a synthetic seismogram to compare with the processed VSP data. A statistical wavelet extraction tool in the Hampson-Russell software was restricted to a time window of 985-1025 ms near the zone of the Mannville B coals. To obtain the wavelet, the autocorrelation of the traces are calculated and then the amplitude spectrum of the result is obtained. Next the square root of the amplitude spectrum is taken to obtain the amplitudes spectrum of the wavelet. Then this amplitude spectrum is used to estimate the wavelet (Hampson-Russell Assistant). The extracted outside corridor stack wavelet is displayed in Figure 2.22. Figure 2.23 shows the amplitude spectrum of the extracted wavelet.

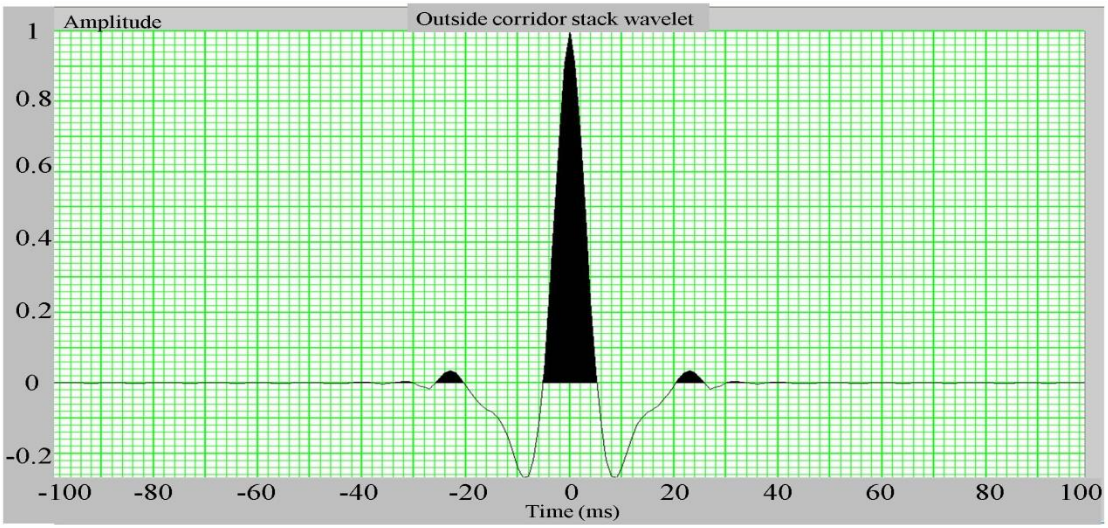

Figure 2.22: Extracted statistical wavelet from the zero offset outside 50 ms VSP corridor stack.

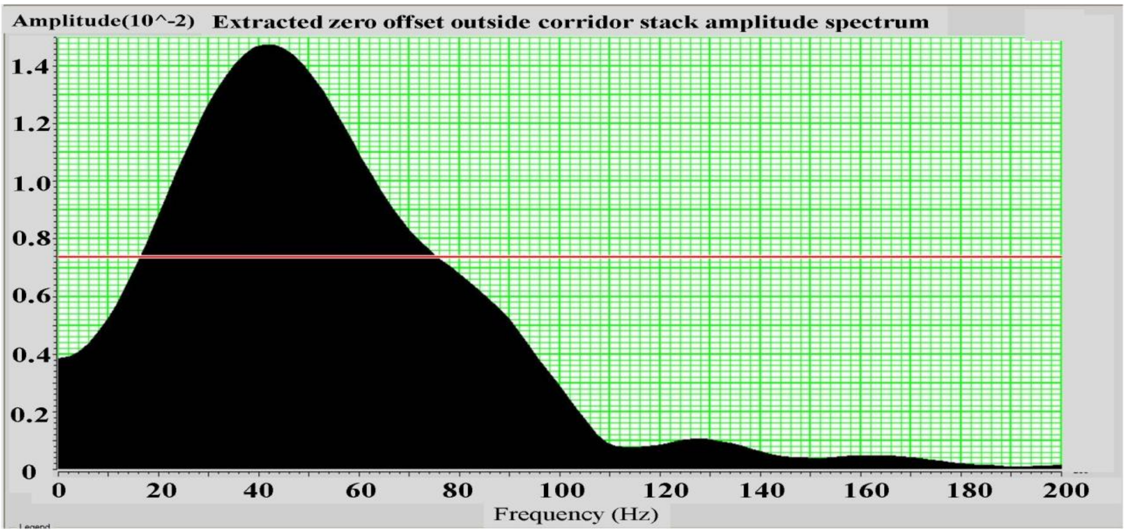

Figure 2.23: Amplitude spectrum of the extracted wavelet from the zero offset outside 50 ms VSP corridor stack.

Figure 2.23 shows that the extracted statistical wavelet has a dominant frequency of about 42 Hz. After examining the outside corridor stack wavelet, I decided to generate a synthetic seismogram using the extracted wavelet for comparison.

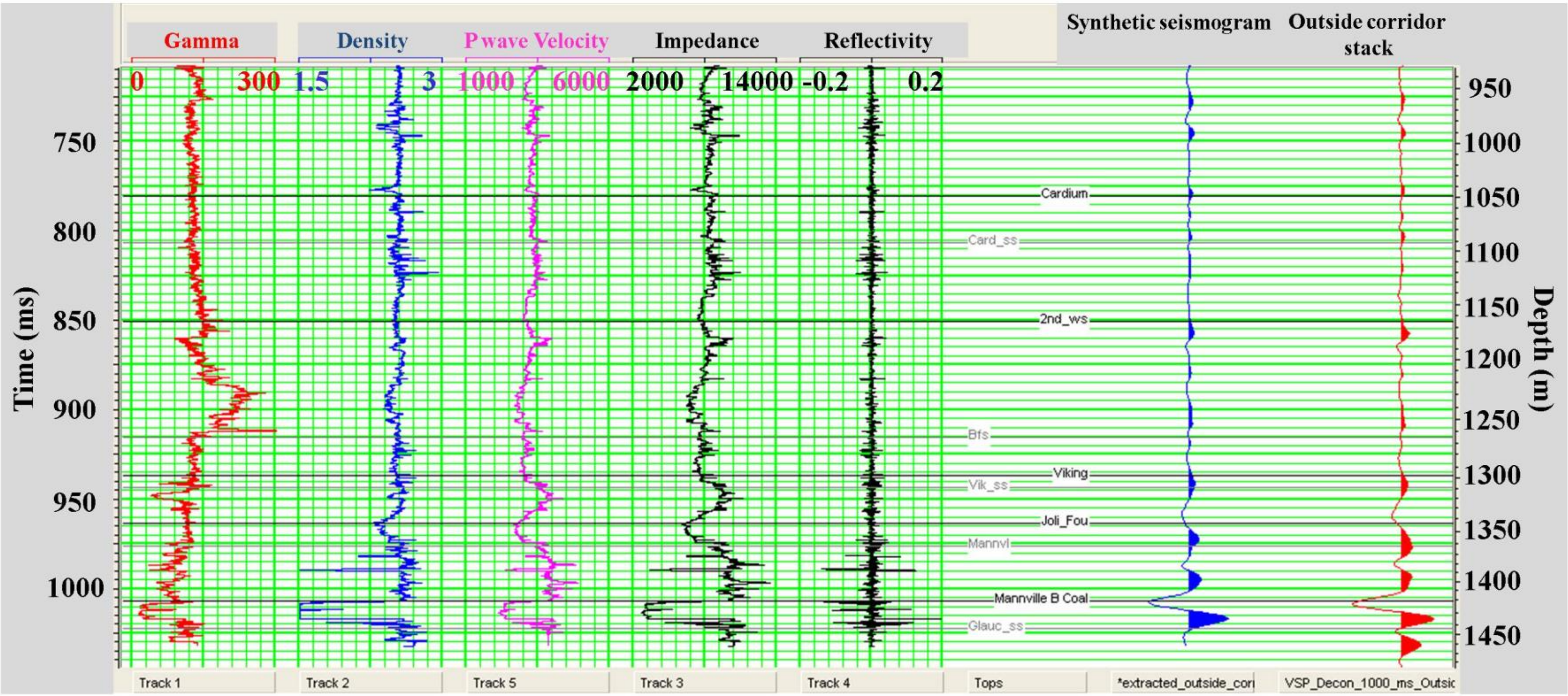

Figure 2.24: Wireline logs plotted alongside the tops, synthetics seismogram generated the extracted wavelet and the outside corridor stack. From left to right: gamma ray log (red), density log (blue), P wave velocities (magenta), computed impedance (black), computed reflectivity (black), formation tops, synthetic seismogram (blue) and outside corridor stack (red).

Analyzing Figure 2.24 indicates the top of the Mannville formation and the top of the Mannville B coals with sharp character in the outside corridor stack and synthetic seismogram. An excellent correlation is achieved between the synthetic seismogram, generated by convolving the log computed reflectivity with the extracted wavelet, and the outside corridor stack that resulted in a 92 % correlation percentage. The top of the Mannville Fm is the increase in impedance at around 975 ms and 1363 m Total Vertical Depth (TVD). On the other hand, the top of the Mannville B coals, which is our target, is indicated by the reduction in P wave velocity, reduction in density, reduction in impedance and therefore corresponding to a trough on the synthetic seismogram and outside corridor stack at 1006 ms or 1423 m TVD.

A further study is conducted by comparing the synthetic seismogram to the outside corridor stack, the inside corridor stack and the full stack. Figure 2.25

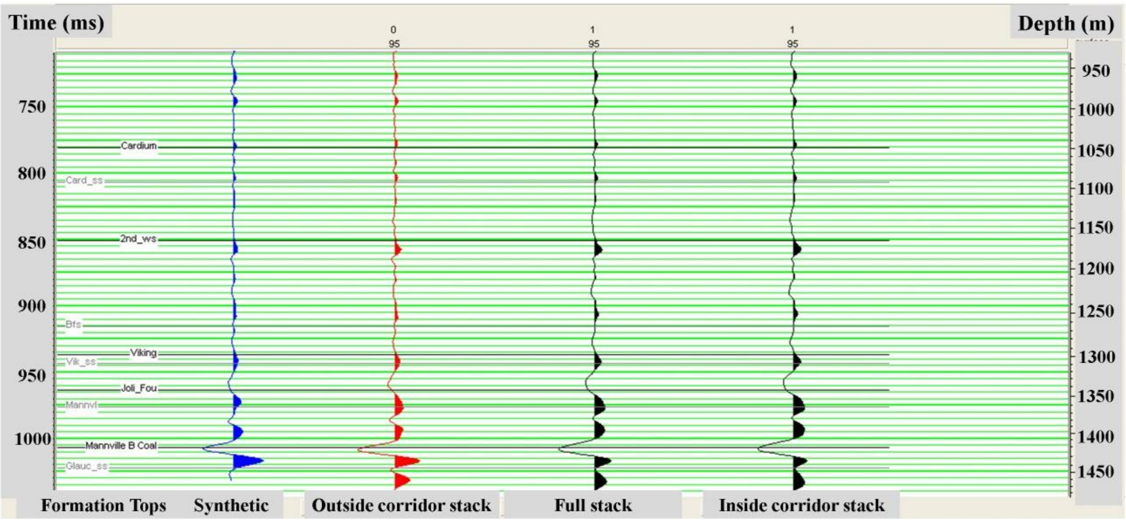

Figure 2.25: The synthetic seismogram plotted alongside the outside corridor stack, the full stack and the inside corridor stack respectively.

Figure 2.25 displays the synthetic seismogram generated from the convolution of the extracted wavelet with the log calculated reflectivity alongside the outside corridor stack, the full stack and the inside corridor stack respectively from left to right. The synthetic seismogram is the closest in similarity to the outside corridor stack in terms of the shape of the trough indicating the coals at 1423 m TVD or 1006 ms and the peak just below of it at 1017 ms or 1435 m TVD. On the other hand, the full stack and inside corridor stack are very similar in terms of the amplitudes and shapes of the peaks and trough especially within the Mannville Fm. This is expected since the only difference between the full stack and the inside corridor stack is that narrow strip of 50 ms around the first breaks that are used to generate the outside corridor stack.

3.8 Discussion

In the zero offset VSP processing, the only component processed is the vertical Z component. This is due to the lack of P wave energy in the two horizontal components. From the raw Z component, a velocity model was obtained, derived from the first break traveltimes and will be used in future walkaway VSP processing.

For wavefield separation, a 21 point median filter was applied to the flattened downgoing waves to eliminate upgoing waves. Then the upgoing waves were obtained after subtracting the median filtered downgoing waves from the original data to yield the upgoing waves.

Deconvolution was performed on both downgoing and upgoing waves. The deconvolution operator was designed on the downgoing wavefield and then applied to the upgoing wavefield. The deconvolution produced sharper and better defined reflection events. Analyzing the amplitude spectrum of the upgoing wavefield before and after deconvolution proved that the applied deconvolution operator resulted in a white reflectivity series. After deconvolution, no multiples were apparent in the upgoing wavefield.

The last processing step was the computation of the inside and outside corridor stacks. The corridor mute was set to 50 ms which aimed to isolate P wave primary reflections and exclude multiples if any. Varying this mute window between 30 – 70 ms proved no significant difference in the window selection of the outside corridor stack. This is interpreted as either the multiples in the data were removed by deconvolution of that the mute windows selected were not wide enough to include any multiples. The outside corridor stack showed no significant multiples when compared to the inside corridor stack.

The zero offset VSP outside corridor stack has a dominant frequency of 42 Hz. The comparison of the outside corridor stack with the synthetic seismogram showed an excellent correlation between the stacks and they both appear very similar. All of the corridor stacks and the synthetic seismogram indicate the Mannville B coals with a sharp trough and the top of the Mannville Fm with a peak. An excellent correlation was also obtained between the synthetic seismogram, the outside corridor stack, the full stack and the inside corridor stack. The full stack and inside corridor stack appear to be very similar to each other with subtle differences between them and the outside corridor stack.

CHAPTER 3: WALKAWAY VSP

Three walkaway VSP survey lines were oriented east, southeast and south of the well. There were ten offset shots for the east survey while the other two surveys each had eleven offset shots. Each walkaway is processed using the same processing flow starting from geometry and first break picking to VSPCDP and VSPCCP mapping. In this section, a near, mid and far offset of the east walkaway VSP are shown in each processing step only. The final result of the south and southeast walkaways are displayed near the end of the chapter.

3.1 Acquisition

The VSP east, southeast and south walkaway shot offsets are summarized in Table 3.1. Figure 3.1 shows the orientation of the three VSP surveys and the offset shot points.

Table 3.1: East, southeast and south walkaway shot offsets.

Shot counter	East Offset (m)	Southeast Offset (m)	South Offset (m)
1	-51	-51	51
2	114	131	-139
3	249	270	-240
4	388	431	-379
5	529	551	-518
6	667	692	-647
7	807	830	-802
8	946	970	-938
9	1086	1100	-1079
10	1226	1250	-1214
11	N/A	1391	-1346

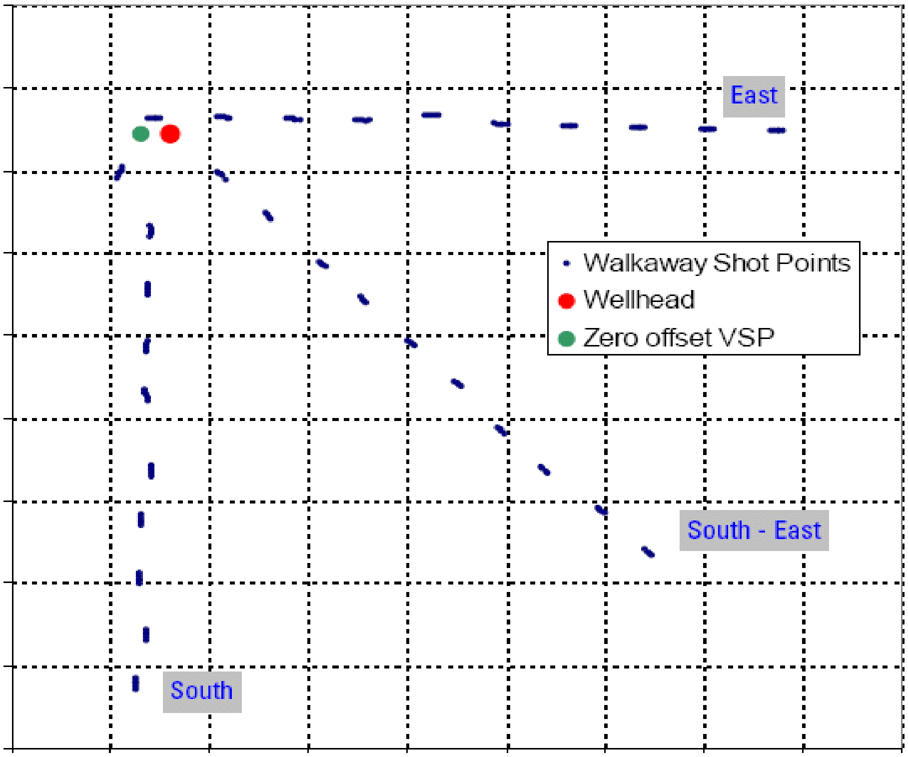

Figure 3.1: The three walkaway VSP surveys east, southeast and south. The dotted lines show the offset shot points with axes northing and easting. The figure also shows the well and the Zero Offset VSP survey location (Parker and Jones, 2008).

Each shot had its own elevation that had be taken into account while entering the shot geometries. Figure 4.2 shows the shot elevation for each of the walkaway lines.

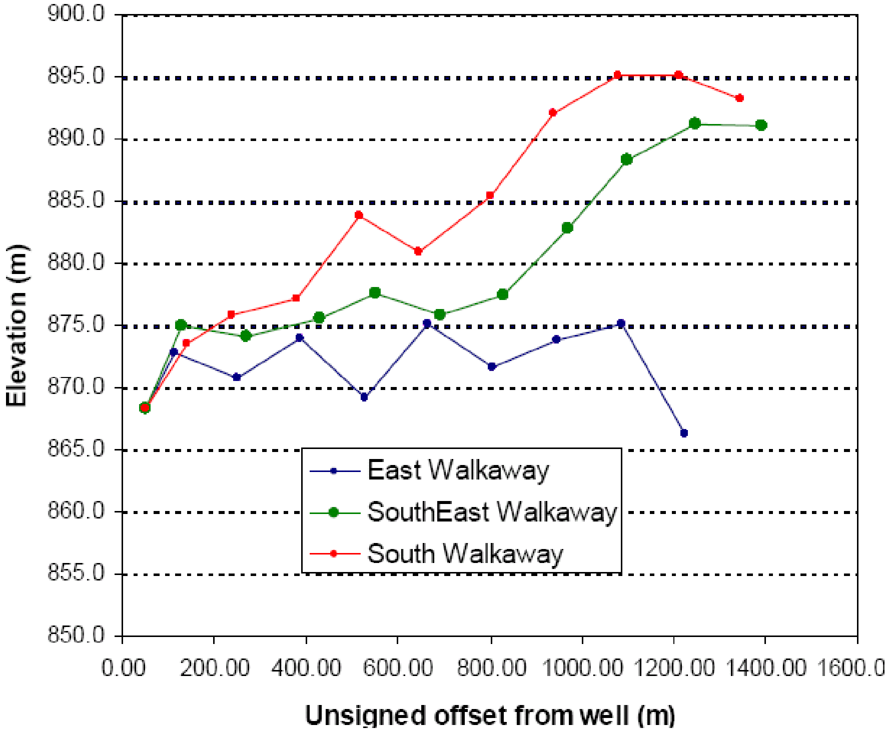

Figure 3.2: Elevation of each of the offset shot points for all three walkaway VSP surveys (Parker and Jones, 2008).

Table 3.2 shows the acquisition parameters of the three walkaway VSPs.

Table 3.2: Walkaway VSP acquisition parameters.

Acquisition Parameters	Details
Source	Dynamite
Receiver tool	Four 8 shuttles with 3C receivers
Receiver separation	15.1 m
Acquisition depths	468 - 1420 m
Kelly Bushing elevation (MSL)	872.2 m
Datum elevation or ground level (MSL)	868.1 m

Table 3.2 shows the acquisition parameters used for all three walkaway surveys. The sources of the three surveys were dynamite sources that were buried approximately 15 m from the surface. The receiver tool contains 8 shuttles with three component

receivers indicating that the tool has 8 levels of receivers separated by 15.1 meters with each receiver containing two horizontal components and one vertical component. The receivers were distributed from depth 468 m to 1420 m. The Kelly Bushing and datum was the same as that of the zero offset VSP survey discussed in Chapter 2. Figure 3.3 illustrates how these receivers were assembled in the borehole. The horizontal position of the tools is just for illustration purposes.

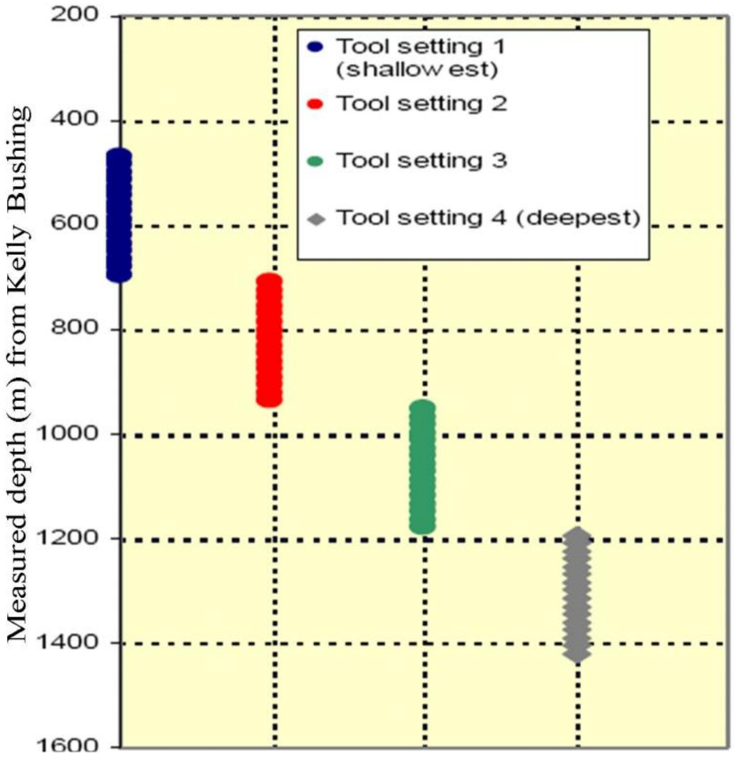

Figure 3.3: An illustration of the assembly of receivers in the borehole for the acquisition of the Walkaway VSP surveys.

3.2 Geometry

An essential step in VSP processing is the geometry input. The data provided contained all the offset shots in one file. A flow to separate all the shots depending on their offset was created and utilized. Shot depths were set to 15 meters below the shot elevation. Replacement velocities are calculated by dividing the straight distance from source to receiver on the first arrival time to the shallowest receiver.

In the global settings of the program, sorting for the data stacks were set to primary and secondary sorting to create headers just as follows:

1) Primary: Common Mid Point (CMP), Secondary: Source-Receiver Offset.
2) Primary: Trace Code ID, Secondary: Depth Receiver.
3) Primary: Shot Point Number, Secondary: Depth Receiver.
4) Primary: Source-Receiver Offset, Secondary: Depth Receiver.

For each offset, the headers were modified to create Trace Code IDs. Each channel has the three components X, Y and Z numbered as 1, 2, and 3 respectively are referred to as 1, 3, and 2 respectively for Trace Code ID.

3.3 First breaks

The common shot gathers were sorted into the X, Y and Z components. On each component, the first breaks are picked on the first trough of the raw Z component and transferred to the other two components. The X and Y horizontal components are randomly changing directions in the borehole and therefore have to be rotated to show consistent upgoing and downgoing wavefields. Figures 3.4 – 3.6 show all three components of the data for a near (114 m), mid (529 m) and far (946 m) offset of the east walkaway VSP survey.

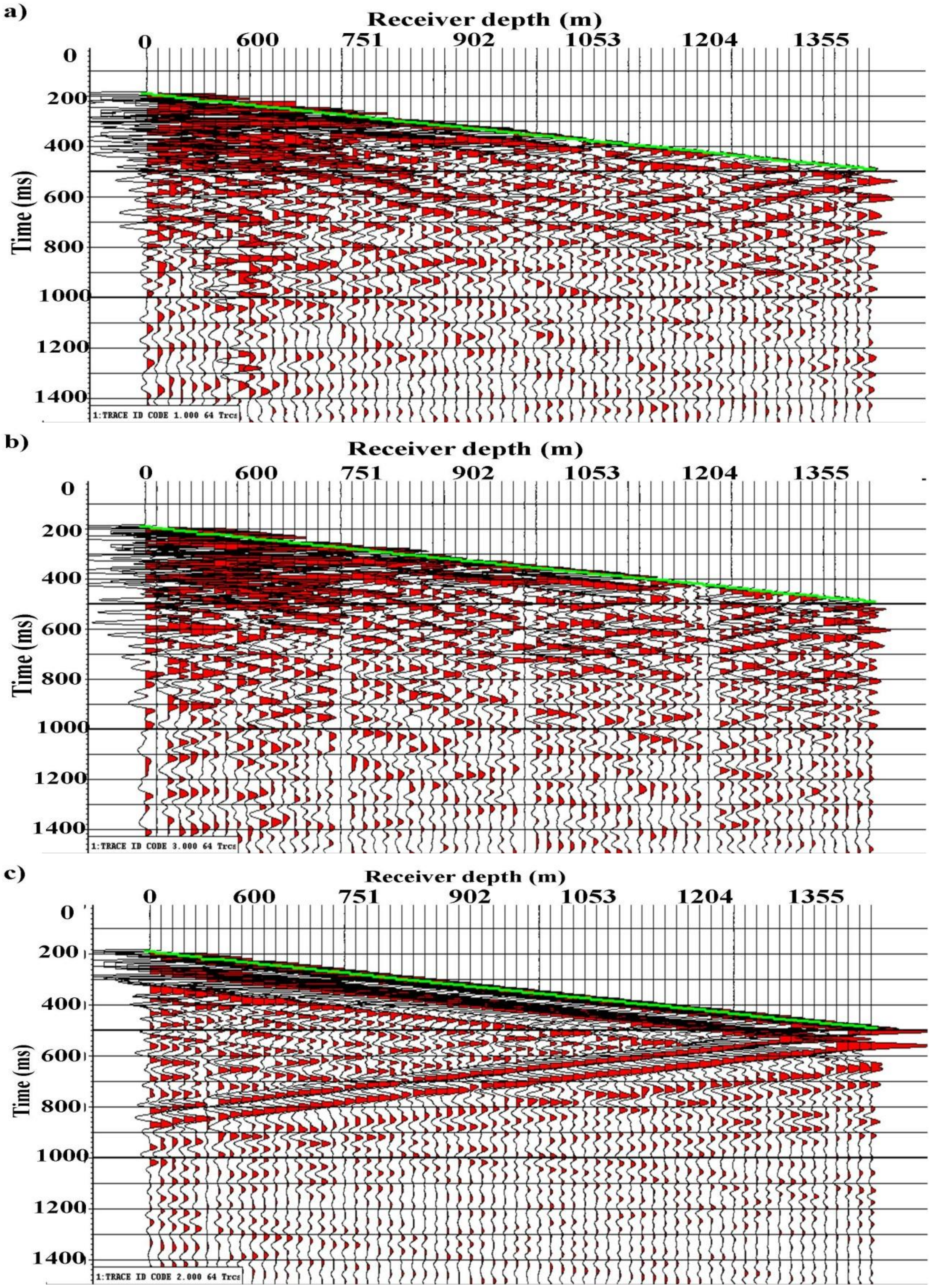

Figure 3.4: East walkaway data at offset 114 a) X component b) Y component c) Z component.

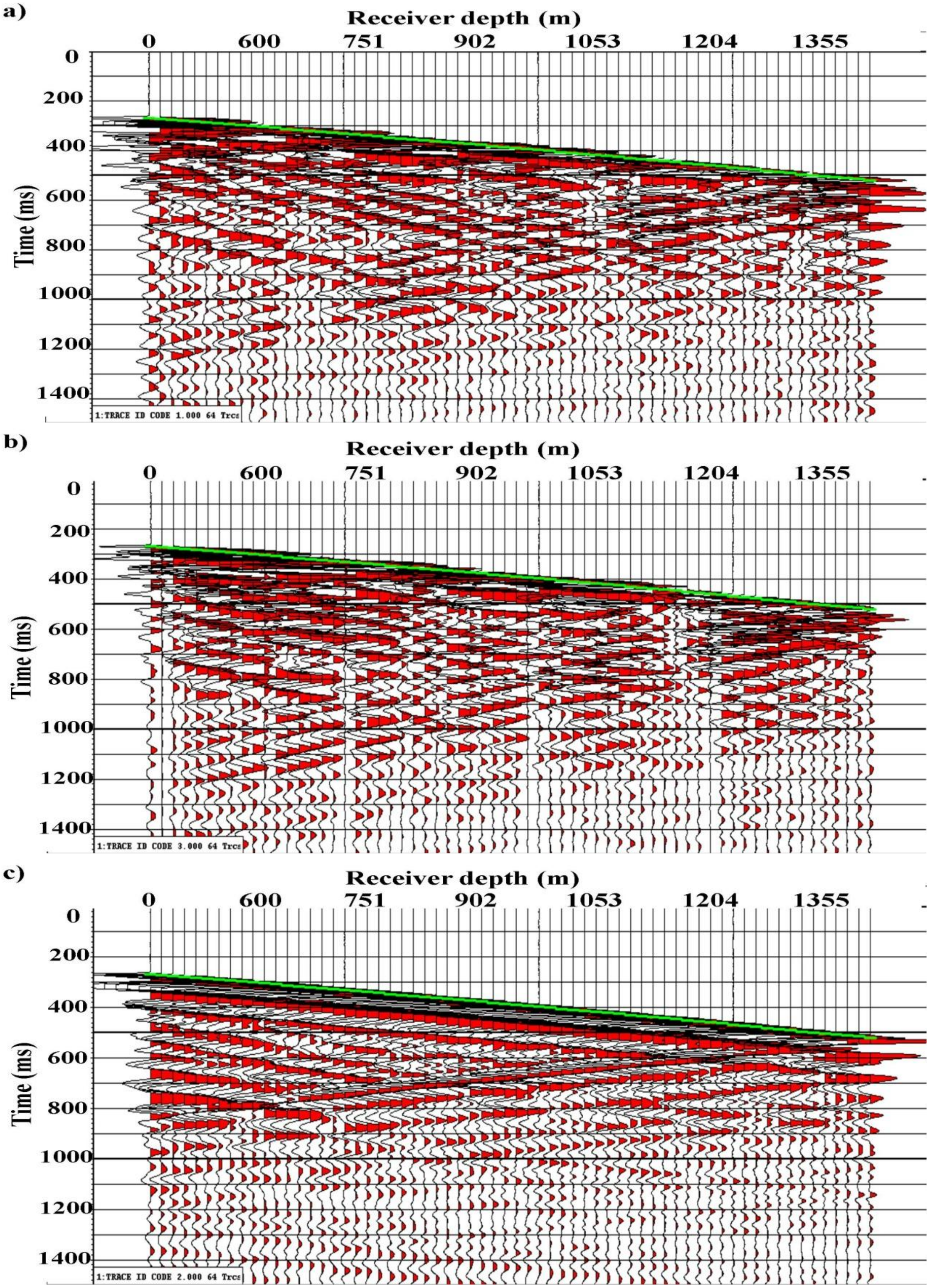

Figure 3.5: East walkaway data at offset 529 a) X component b) Y component c) Z component.

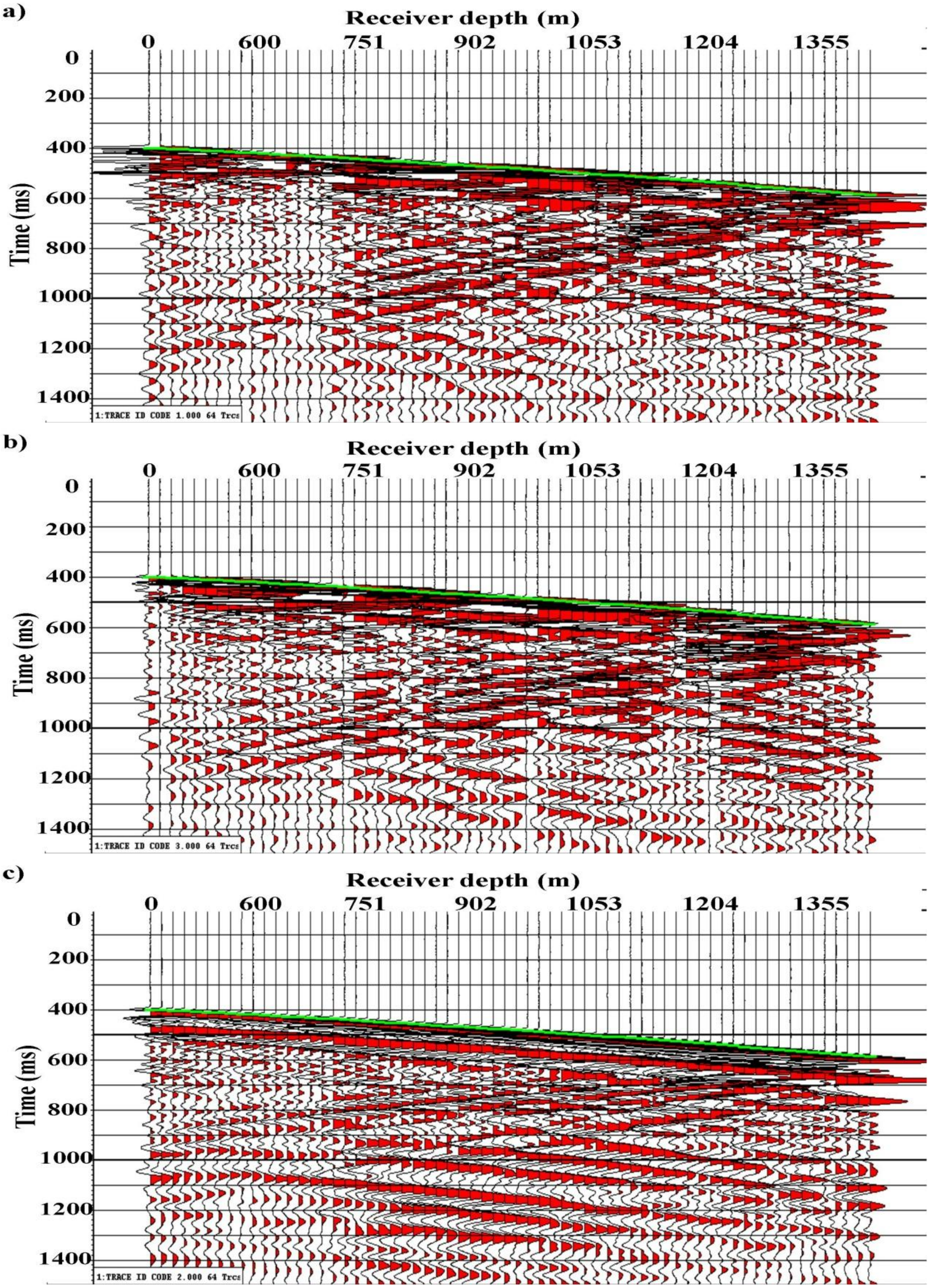

Figure 3.6: East walkaway data at offset 946 a) X component b) Y component c) Z component.

Assessing the different components with increasing offset, the records indicated different characteristics. It is evident that as the offset increases, the number of shear waves also increases in all three components. It is also noticed that as offset increases, the amplitude of the shear waves also increases especially downgoing shear waves at later times of each component. These observations are explained by the Zoeppritz equations in the next section.

There is a dominance of downgoing P waves in the Z component for each offset. In addition, as offset increases, the components are consumed more with shear waves overlaying the P wave reflections especially in the Z components of each offset and is clear in Figures 3.5 and 3.6.

The two horizontal components X and Y express an increase in shear wave with increase of offset as well. It is noted that not much reflection energy is noticed in the horizontal components compared with the vertical Z component. Furthermore, the two horizontal components show mixed upgoing and downgoing wavefields with lack of definition. Hodogram rotations will be performed later in this chapter to isolate the downgoing waves from the upgoing waves. The full component selection of the east walkaway VSP survey data can be seen in Appendix A.

3.4 Zoeppritz explorer

In seismic processing and analysis, the relation of amplitude change with the increase of offset is investigated. Zoeppritz equations are usually utilized for analysis of amplitude reflections of seismic data and give the reflection and transmission amplitudes of plane waves as a function of angle of incidence (Shuey, 1985).

The underlying assumptions of the Zoeppritz equations have to do with two boundary conditions. The first is continuity of displacement where no rupture or sliding of boundaries is tolerated. The second is the continuity of traction or stress tensor (Lines and Newrick, 2004).

To get a better understanding of the relationship between reflection coefficients and incidence angle as expressed by the Zoeppritz equations and some approximations, an example is generated using the CREWES Zoeppritz Reflectivity Explorer 2.1. Table 3.3 shows the petrophysical values used to calculate reflection amplitudes at the top of the Mannville B coal. Figure 3.7 shows the result of the reflection coefficients with increase of angle of incidence by means of Zoeppritz equation and both Aki-Richards approximation and the two term Shuey approximation.

Table 3.3: Estimation of Zoeppritz parameters for the top of the Mannville B Coal reflection.

	Vp (m/s)	Vs (m/s)	Density (kg/m^3)
Upper Layer	4270	2330	2600
Coal	2350	1120	1790

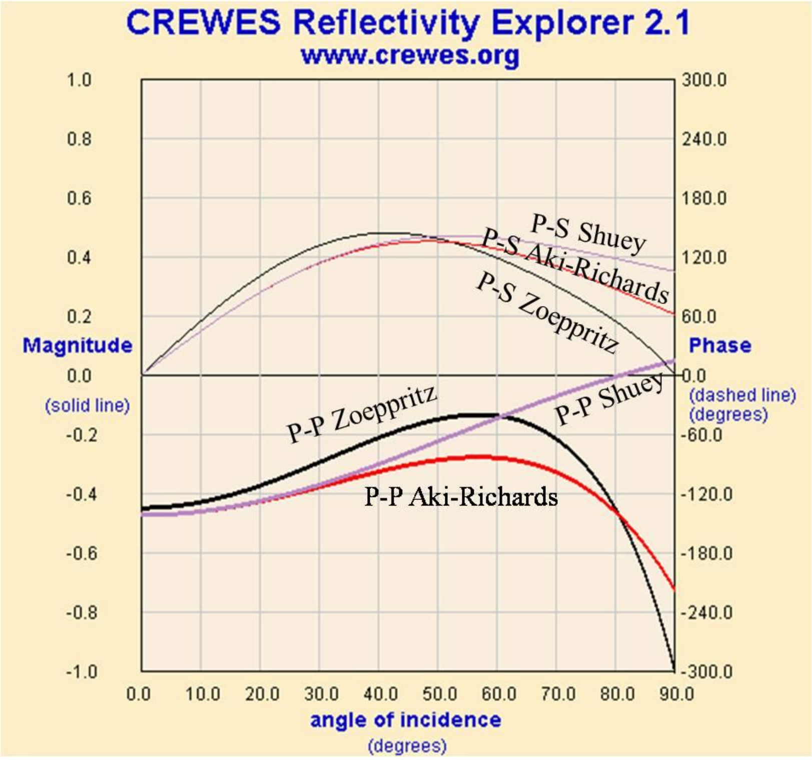

Figure 3.7: Zoeppritz reflection coefficients with Aki Richards and Shuey approximations for the top of the Mannville B Coal based on Table 4.1. The Zoeppritz reflection is in black, the Shuey two term is in plum and the Aki Richards approximation is in red.

Considering Figure 3.7, the Shuey and Aki-Richards approximation are compared to the Zoeppritz reflections within a window of angles 0-50 degrees. The Zoeppritz equations are complex and cannot be fitted to seismic data directly. Solutions to the Zoeppritz equations are hard to interpret with different cases. Therefore, analysis such as Amplitude Variation with Offset (AVO) generally deals with approximations to the Zoeppritz equations (Lines and Newrick, 2004). The approximations used in this example are the Aki-Richards approximation and the two term Shuey approximation. The Zoeppritz reflections and the Shuey and Aki-Richards approximations all show a decrease in amplitude for the incident P wave and reflected P wave curves. On the other hand, the Zoeppritz reflection and both approximations show an increase in amplitude with increasing angle of incidence for the incident P wave and reflected S wave. The Aki-Richards approximation closely mimics the Zoeppritz reflections for both cases. The two term Shuey approximation also closely mimics both the Zoeppritz and Aki-Richards approximation to about the 50 degree mark. From the analysis of the Zoeppritz equation behaviour, the result of the decrease of P wave amplitudes and increase of S wave amplitudes with increase of offset is consistent with the Zoeppritz equation result and the approximation results.

3.5 Velocity Profiling

The velocity profile of each offset is derived from the first breaks picked on the raw vertical Z component of that specified offset. With the first break times and the receiver depth, the velocities are inverted on each offset. In addition, the geometry of each of the offsets was revisited to input the replacement velocity for the shallow layers between the surface of the earth and the first shallow receiver. The distance between the source and the shallowest receiver is calculated by Pythagoras theorem using the source-well offset and the depth of the receiver to obtain it. Then the replacement velocity is calculated by dividing the resulting distance by the first break time of the shallowest receiver. Table 3.4 – 3.6 shows the calculated values for all three walkaway lines.

Table 3.4: Calculation of replacement velocity for east walkaway VSP.

VSP Survey	Offset (m)	Shallowest Receiver Depth (m)	Well-Shot Offset (m)	First break time (ms)	Replacement Velocity (m/s)
East	51	463.83	466.63	0.181	2578
East	114	463.83	477.63	0.189	2527
East	249	463.83	526.44	0.206	2556
East	388	463.83	604.72	0.234	2584
East	529	463.83	703.55	0.267	2635
East	667	463.83	812.42	0.309	2629
East	807	463.83	930.80	0.353	2637
East	946	463.83	1053.59	0.398	2647
East	1086	463.83	1180.90	0.433	2727
East	1226	463.83	1310.81	0.469	2795

Table 3.5: Calculation of replacement velocity for southeast walkaway VSP.

VSP Survey	Offset (m)	Shallowest Receiver Depth (m)	Well-Shot Offset (m)	First break time (ms)	Replacement Velocity (m/s)
Southeast	51	463.83	466.63	0.181	2578
Southeast	131	463.83	481.97	0.194	2484
Southeast	270	463.83	536.69	0.217	2473
Southeast	431	463.83	633.17	0.250	2533
Southeast	551	463.83	720.24	0.280	2572
Southeast	692	463.83	833.07	0.318	2620
Southeast	830	463.83	950.81	0.355	2678
Southeast	970	463.83	1075.19	0.401	2681
Southeast	1100	463.83	1193.79	0.443	2695
Southeast	1250	463.83	1333.28	0.490	2721
Southeast	1391	463.83	1466.29	0.542	2705

Table 3.6: Calculation of replacement velocity for south walkaway VSP.

VSP Survey	Offset (m)	Shallowest Receiver Depth (m)	Well-Shot Offset (m)	First break time (ms)	Replacement Velocity (m/s)
South	51	463.83	466.63	0.181	2578
South	139	463.83	484.21	0.192	2522
South	240	463.83	522.24	0.208	2511
South	379	463.83	598.98	0.236	2538
South	518	463.83	695.31	0.272	2556
South	647	463.83	796.08	0.301	2645
South	802	463.83	926.47	0.355	2610
South	938	463.83	1046.41	0.392	2669
South	1079	463.83	1174.47	0.440	2669
South	1214	463.83	1299.59	0.476	2730
South	1346	463.83	1423.68	0.516	2759

After assessment of the interval velocities from the analysis of the first break times, it was noticed that there were shot static problems. These shot static problems occur between different receiver settings and due to a different shot being fired to each tool setting. The corrections occur between depths 690.63 - 705.62 meters, 932.42 - 947.36 meters and 1174.16-1189.08 meters corresponding to the changes in tool settings. The only exceptions from this shot static problem are the near offsets of each walkaway line. In other words the exceptions are the east walkaway offset -51, southeast walkaway offset -51, and the south walkaway offset 51. The shot static problem was resolved using the following flow illustrated in Figure 3.8.

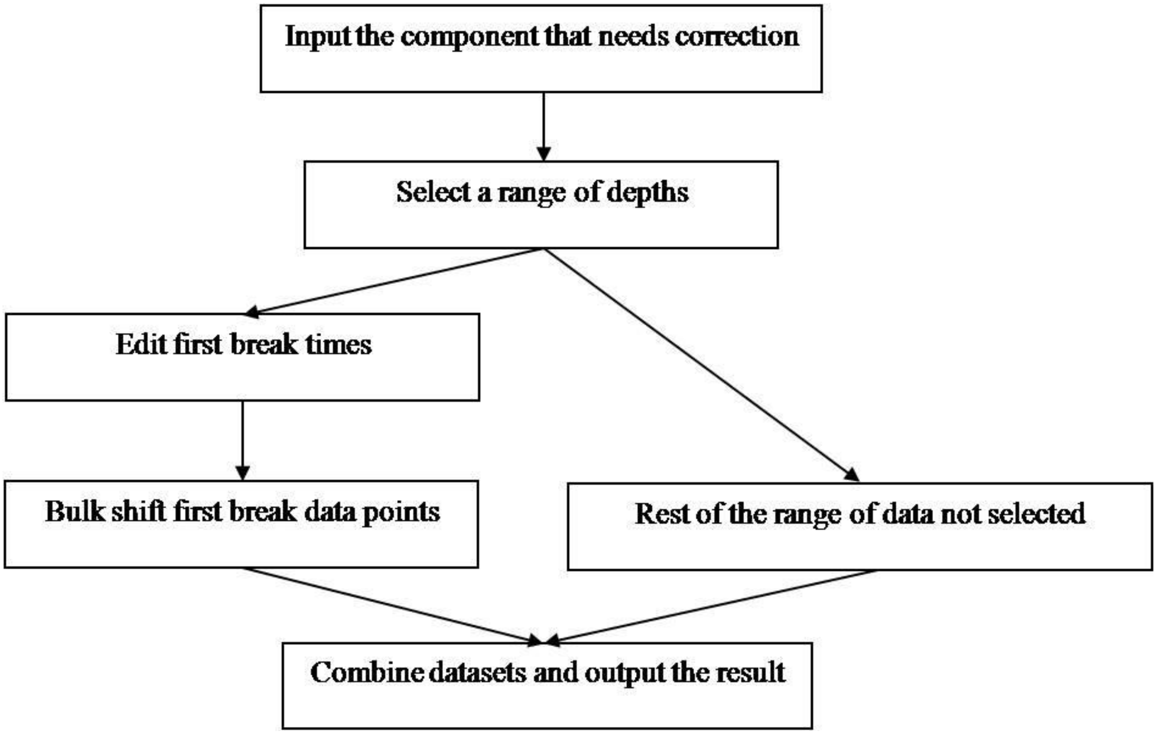

Figure 3.8: Shot static correction flow for walkaway VSP first breaks.

The inputs to Figure 3.8 flow are the individual are the raw X, Y and Z components. A range of depths are selected greater than 705.62, 947.36 and 1189.08 meters representing the ends of each receiver tool for each offset for all three depth ranges. Each range is passed on one branch of the flow and all the lower depths are considered “Failed” and are passed on unmodified. For the data that is passed, a constant time and a time static bulk shift is added for the receivers over the range of depths selected. Then the “Pass” and “Fail” data are combined to give the corrected result at that specific range of data. The result then becomes the input of the same flow with the next selection of depths until the final corrected component is reached. Tables 3.7 – 3.9 gives the numbers used for both the first break constant addition and the time bulk shift applied to each range of depth for each component. Note that a bad first break pick on the east walkaway was deleted at receiver depth 539.43 meters.

Table 3.7: First break constant time and bulk shift for east walkaway shot static correction.

Offset (m)	Depth Criteria (m)	FB Correction Time (ms)	Shot Bulk Shifting (m)
East 114	Greater than 700	1	1
	Greater than 940	1	1
	Greater than 1180	-1	-1
East 249	Greater than 700	1	1
	Greater than 940	1.25	1.25
	Greater than 1180	1.25	1.25
East 388	Greater than 940	1.75	1.75
	Greater than 1180	1	1
East 529	Greater than 940	4	4
	Greater than 700	1	1
	Greater than 1180	2	2
East 667	Greater Than 700	2	2
	Greater than 940	3	3
	Greater than 1180	1	1
East 807	Greater than 940	3.5	3.5
	Greater Than 700	1.5	1.5
	Greater Than 1180	2.5	2.5
East 946	Greater Than 940	5.5	5.5
	Greater Than 700	4.5	4.5
	Greater Than 1180	1	1
East 1086	Greater Than 940	4	4
	Greater Than 700	-0.25	-0.25
	Greater Than 1180	1.25	1.25
East 1226	Greater Than 940	3.75	3.75
	Greater Than 700	1.25	1.25
	Greater Than 1180	1.5	1.5

Table 3.8: First break constant time and bulk shift for southeast walkaway shot static correction.

Offset (m)	Depth Criteria (m)	FB Correction Time (ms)	Shot Bulk Shifting (m)
Southeast 131	Greater than 700	1	1
	Greater than 940	2	2
	Greater than 1180	1	1
Southeast 270	Greater Than 700	1.5	1.5
	Greater than 940	1.5	1.5
	Greater Than 1180	2.25	2.25
Southeast 431	Greater than 700	1.5	1.5
	Greater Than 940	1.75	1.75
	Greater Than 1180	0.5	0.5
Southeast 551	Greater Than 700	0.5	0.5
	Greater than 940	2	2
	Greater than 1180	2	2
Southeast 692	Greater Than 700	1.5	1.5
	Greater than 940	2	2
	Greater Than 1180	1.25	1.25
Southeast 830	Greater Than 700	-2	-2
	Greater Than 940	2.5	2.5
	Greater Than 1180	1.75	1.75
Southeast 970	Greater Than 700	2	2
	Greater Than 940	1.75	1.75
	Greater Than 1180	2	2
Southeast 1100	Greater Than 1180	4.25	4.25
	Greater Than 940	1	1
Southeast 1250	Greater Than 700	2	2
	Greater Than 940	2	2
	Greater Than 1180	1.25	1.25
Southeast 1391	Greater Than 940	3.75	3.75
	Greater Than 700	0.5	0.5
	Greater Than 1180	1	1

Table 3.9: First break constant time and bulk shift for south walkaway shot static correction.

Offset (m)	**Depth Criteria (m)**	**FB Correction Time (ms)**	**Shot Bulk Shifting (m)**
South -139	Greater than 940	1	1
	Greater than 1180	0.75	0.75
South -240	Greater than 940	3	3
	Greater Than 700	0.5	0.5
	Greater Than 1180	1	1
South -379	Greater than 700	1.5	1.5
	Greater Than 940	1.75	1.75
	Greater Than 1180	1	1
South -518	Greater Than 700	0.25	0.25
	Greater than 940	1.5	1.5
	Greater than 1180	2.25	2.25
South -647	Greater Than 700	1	1
	Greater than 940	3	3
	Greater Than 1180	1.5	1.5
South -802	Greater Than 700	0.5	0.5
	Greater Than 940	2	2
	Greater Than 1180	2.5	2.5
South -938	Greater Than 940	5	5
	Greater Than 1180	2	2
South -1079	Greater Than 700	1.25	1.25
	Greater Than 940	4	4
	Greater Than 1180	1.75	1.75
South -1214	Greater Than 700	1.25	1.25
	Greater Than 940	3	3
	Greater Than 1180	0.5	0.5
South -1346	Greater Than 700	1.75	1.75
	Greater Than 940	2	2
	Greater Than 1180	1.5	1.5

Figure 3.9 show the difference between the first break line and interval velocities before and after the shot static correction for the east walkaway VSP at 114 m, 529 m and 946 m offsets shown in Figure 3.9a, 3.9b and 3.9c respectively. The left side of the figure shows a blue first break line representing the shot static corrected time depth line while the green show the first break line before shot static corrections. The right side of the figure shows the green interval velocities before shots static correction whereas the red interval velocities represents the true velocities after shot static correction. There is a first break miss-pick on the east walkaway offset 114 Z component at approximately 539 m depth. Note that since the first break picks were picked on the raw Z component, only the velocities concerning the Z component are shown on the figures.

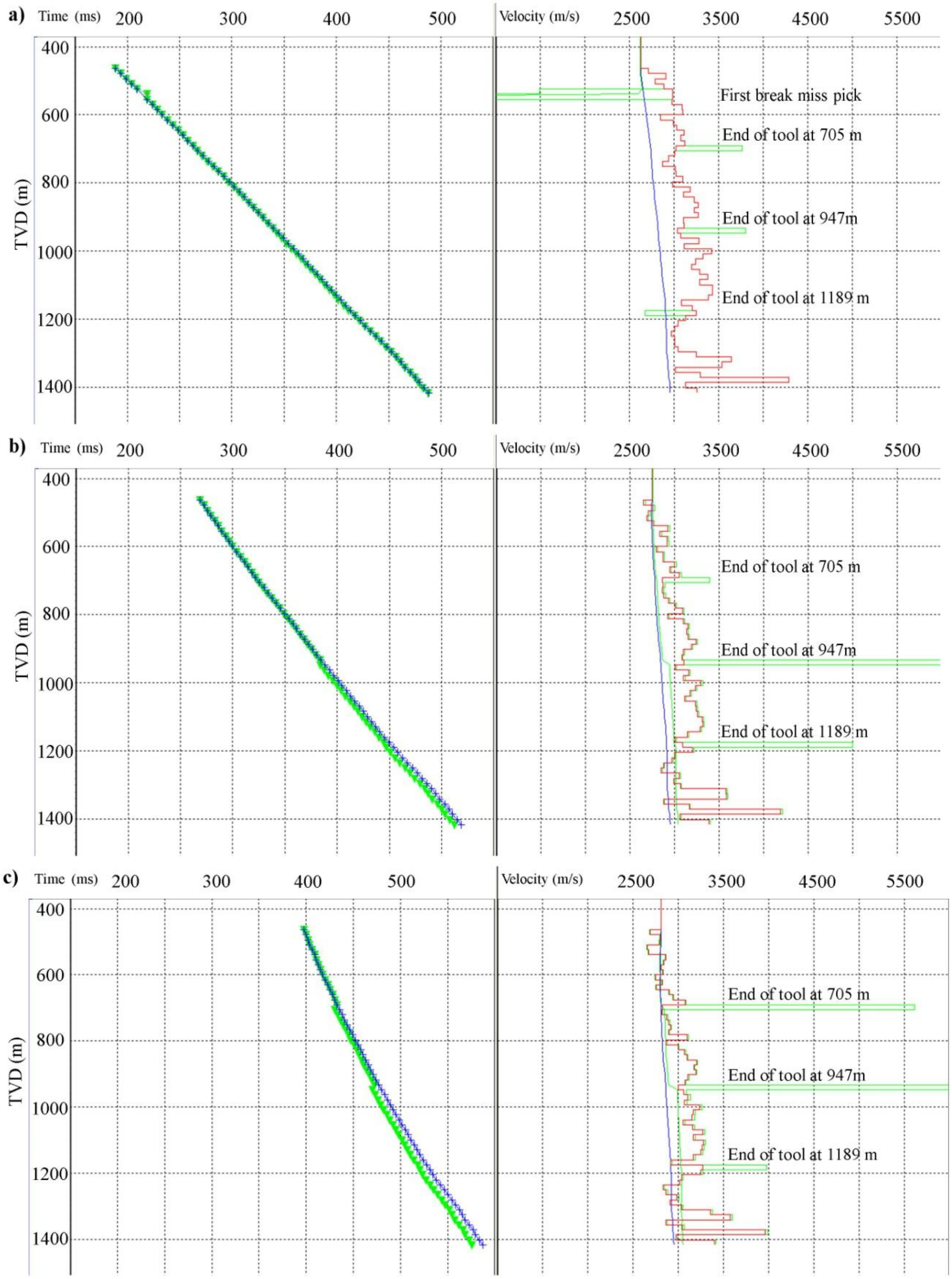

Figure 3.9: First break line and interval velocity before and after shot static correction for east walkaway offset a) 114 m b) 529 m c) 946 m Z component.

As the velocity profile figures illustrate, there was a consistent error in almost all the shot records at depths corresponding to the ends of the receiver tools. It is noticed that as the offset increases for these specific three offsets, the more static correction is needed for each tool setting. The recommendation is to have at least one receiver overlap between the tools in order to eliminate the data problem in future surveys of this type.

3.6 Hodogram analysis

The random orientation of the two horizontal components of the three component geophones needed to be corrected to a consistent pattern. Hodogram analysis was used to analyze the amplitude, polarization and relative orientation of the seismogram components. The hodogram plots X versus Y amplitude components. In this hodogram analysis, the first arrival data show a linear trend. The horizontal components are therefore rotated to maximize the energy of the component towards the source within the time window provided (DiSiena et al., 1984).

The direct linear polarized particle velocity is taken as a reference to orient the data. The two horizontal components are rotated to a new coordinate in which the direct energy is maximized into one component. If X’ is considered to be the maximized energy component, Y’ is the transverse component and ϑ is the angle between the horizontal component X, that is to be rotated, and the maximum energy component X’. The X’ and Y’ components are related to the X and Y horizontal components with the following equations (Disiena et al, 1984):

$$X' = X cos\vartheta + Y sin\vartheta$$

$$Y' = -X sin\vartheta + Y cos\vartheta$$

The maximized energy is expressed in the as follows (Disiena et al., 1984):

$$Energy\ (\vartheta) = E(\vartheta) = \sum_{t=start}^{t=end} (X(t)cos\vartheta + Y(t)sin\vartheta)^2$$

There are two hodogram rotations that are applied to the data. The first hodogram rotation is performed on the two horizontal components X and Y to orient the data towards the source and result in Hmax and Hmin. Ideally, Hmax would contain the Primary (P) and Shear Vertical (SV) wavefields while the Hmin component would contain the Shear horizontal (SH) wavefield. The second hodogram rotation orients the data in the plane formed by the source and well. Inputting Hmax and Z components for the second rotation results in Hmax' and Z' wavefields. In theory, the Hmax' component would contain the downgoing P and upgoing SV while Z' would contain the downgoing SV and upgoing P wavefields (VISTA help and Hinds et al., 1999). The hodogram plots between the X and Y components show a cross plot of the amplitudes of the two input wavefields on the left. The center windows show from top to bottom: the Y component input, the X component input, the Hmax output and lastly the Hmin input. The small window covering the first arrivals of the X and Y components consist of the first break data that will be used for hodogram computation.

The hodograms displayed in Figures 3.10 – 3.12 show the amplitudes of the X and Y traces around the first breaks plotted against each other for offsets 114 m, 529 m and 946 m of the east walkaway VSP survey. The slope of the best fit line through the amplitudes produces the polarization angle. The figures also show the X and Y component energy around the first breaks and then show the energy shift to Hmax while

Hmin is minimum energy after rotation. Notice that the figures highlight the analysis window around the first breaks that is used for the hodogram analysis.

It is obvious from Figures 3.10 -3.12 that the first hodogram rotation polarizes most of the P and SV wave energy in the Hmax components. The downgoing and upgoing P waves are especially strong events when analyzing the Hmax component. The Hmin component shows some residual S wave events but virtually all the P wave energy is contained in Hmax. The Hmin component contains the SH downgoing waves that are more obvious as the offset increases.

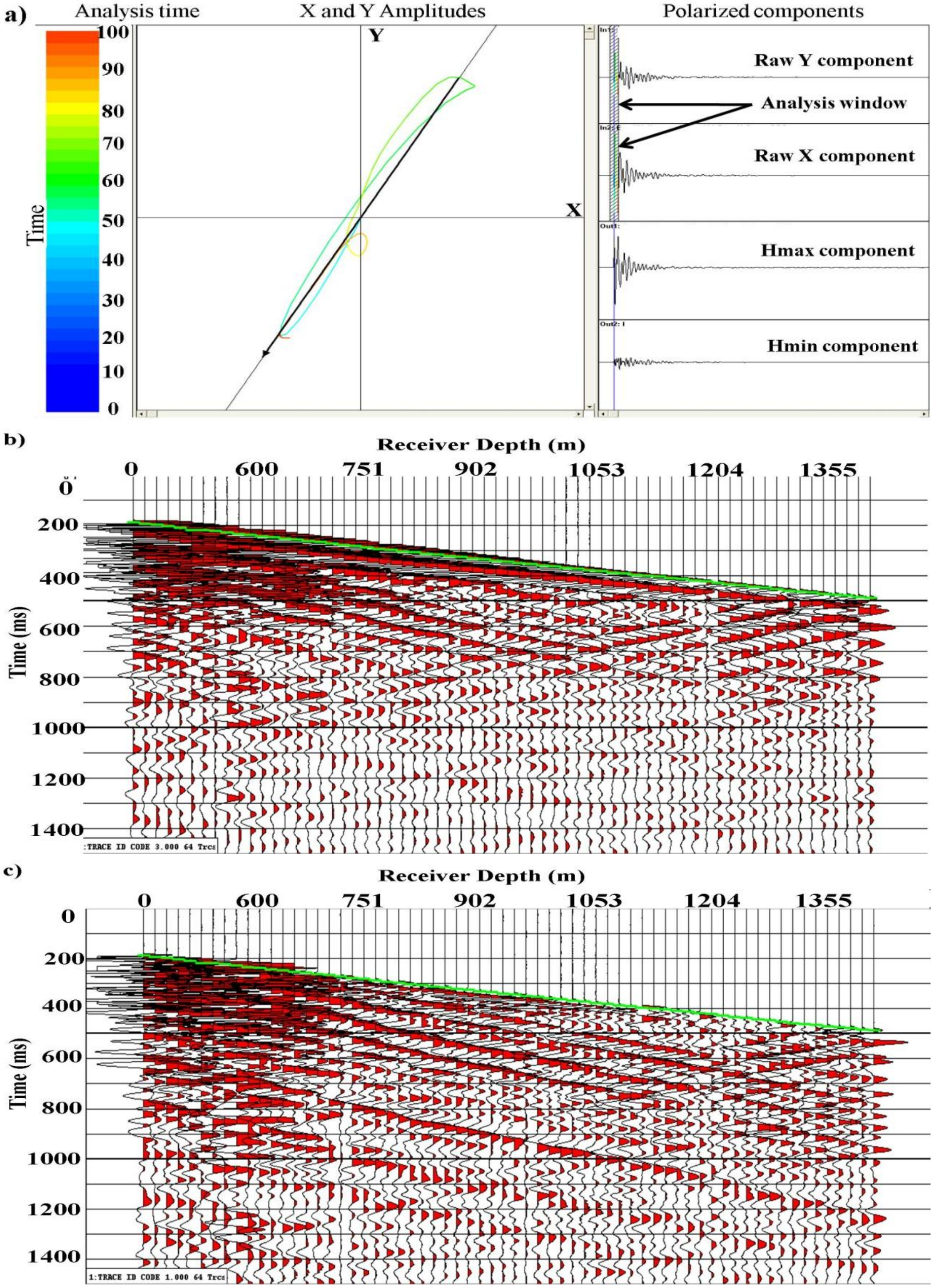

Figure 3.10: a) The hodogram rotation of X and Y components for east walkaway offset 114 m. b) Hmax component c) Hmin component.

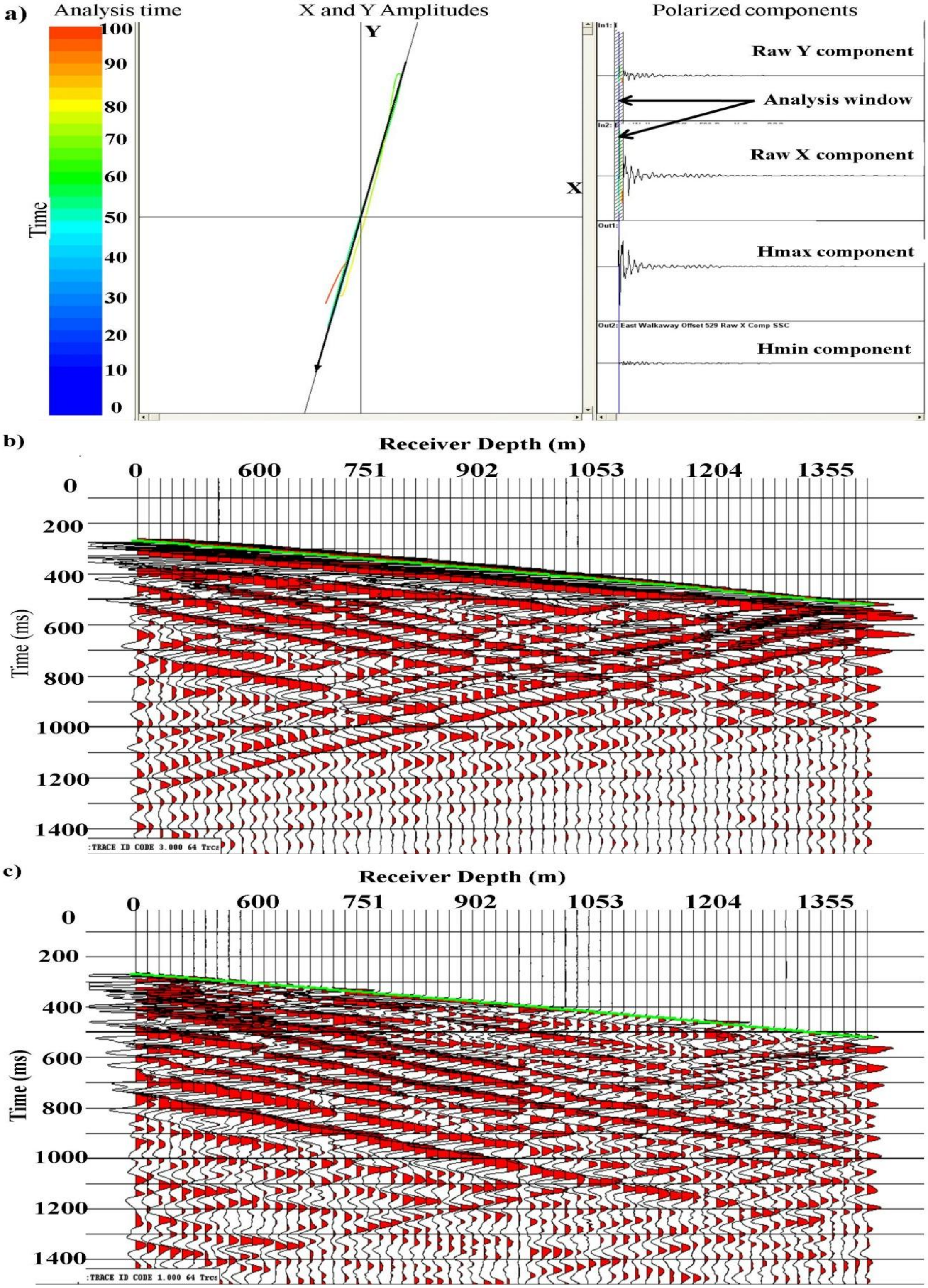

Figure 3.11: a) The hodogram rotation of X and Y components for east walkaway offset 529 m. b) Hmax component c) Hmin component.

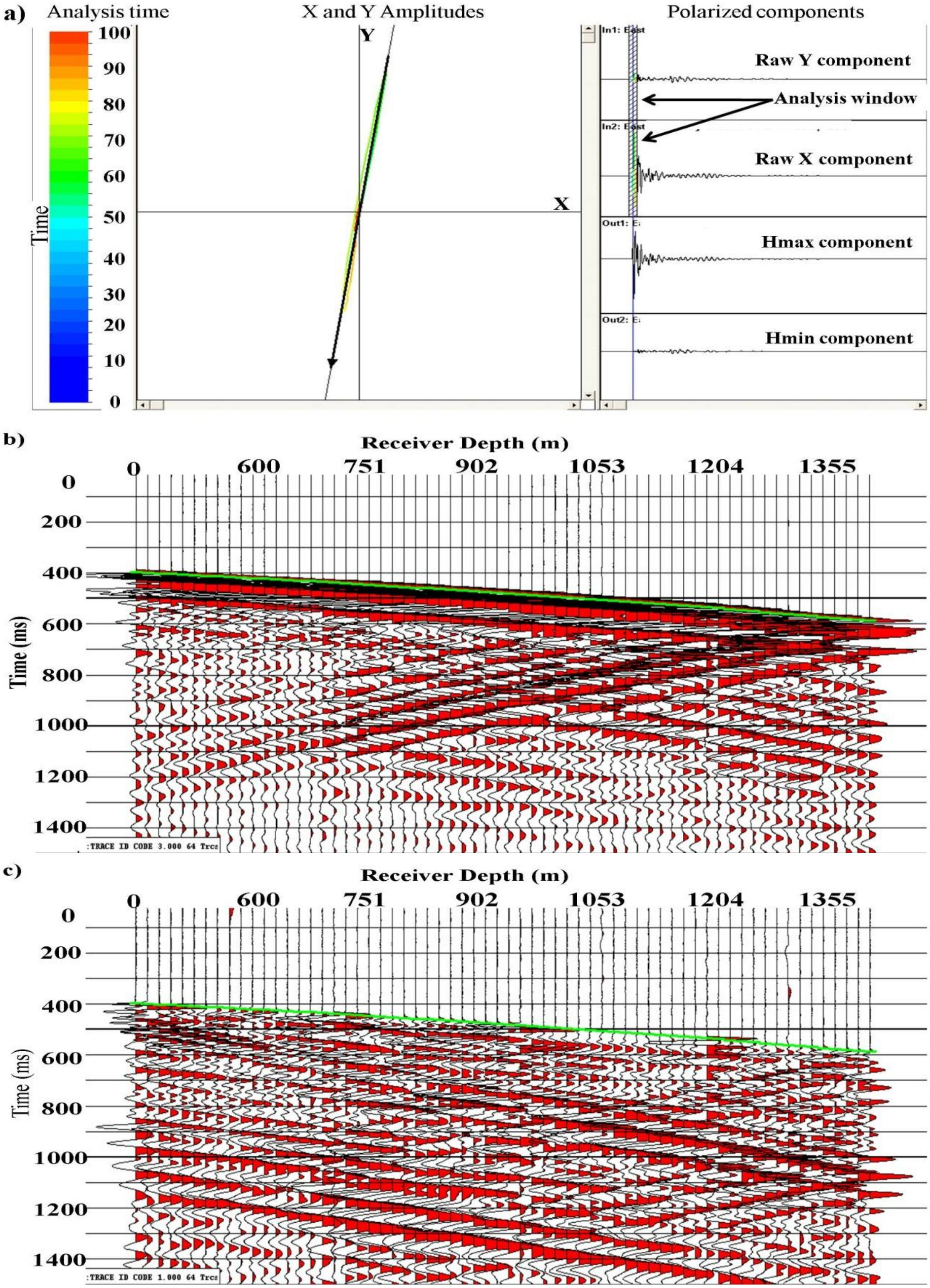

Figure 3.12: a) The hodogram rotation of X and Y components for east walkaway offset 946 m. b) Hmax component c) Hmin component.

The second hodogram rotation operates on the Z component and the Hmax component to output the Z’ and Hmax’ components. The only difference between these hodogram rotations than the previous ones is that this rotation deals with Hmax and the raw Z component. Ideally, the rotation of Hmax and the raw Z component isolates the upgoing waves in the plane of the well and the source. After this hodogram rotation, the downgoing P and upgoing SV are isolated in the Hmax’ component while the downgoing SV and the upgoing P are isolated in the Z’ component (VISTA Help, Hinds et al., 1999). Figures 3.13 and 3.14 illustrate the rays that are shown in the Hmax’ and Z’ components respectively.

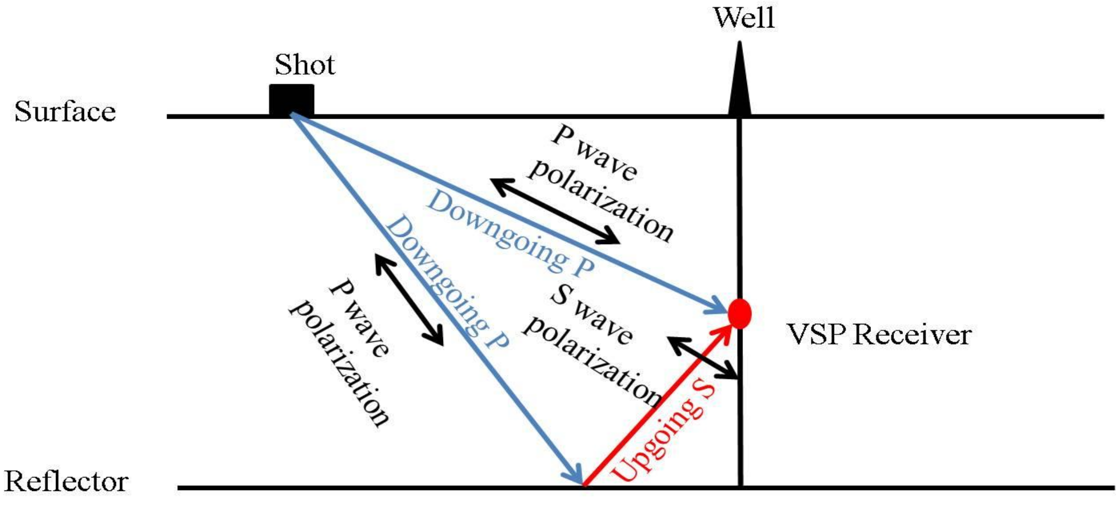

Figure 3.13: Illustration of downgoing waves shown in Hmax’ components.

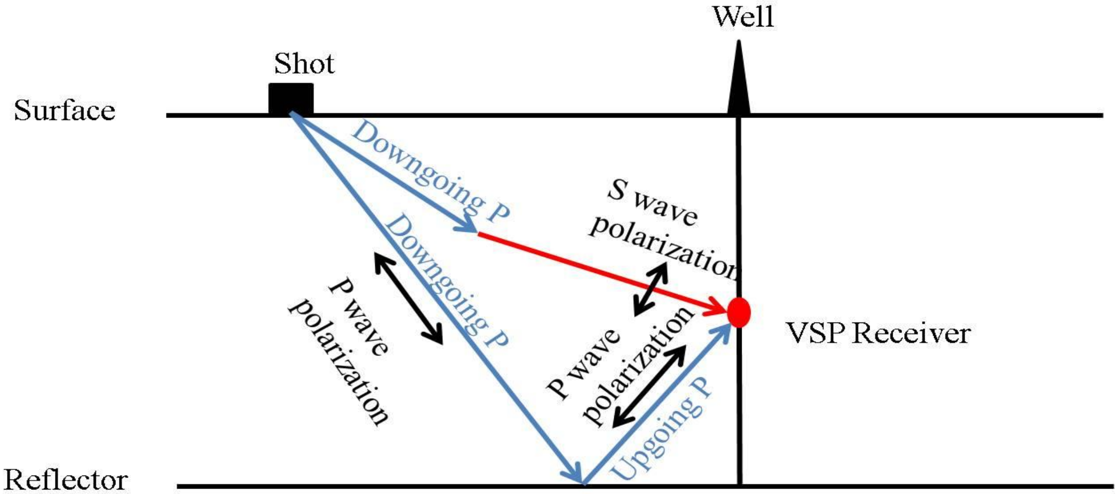

Figure 3.14: Illustration of downgoing waves shown in Z’ components.

Figure 3.13 shows the rays that are recorded in the Hmax’ component. In the figure, it is noticed that the direct downgoing wave going straight to the receiver has a particle motion in the direction of the wave propagation and effects the horizontal component of the receiver. On the other hand, the upgoing S wave has a particle motion perpendicular to the direction of wave propagation and also effects the horizontal component of the receiver since its particle motion is the same as that of the direct downgoing P wave. The total effect of the downgoing P and upgoing S waves effect the horizontal component of the receiver and therefore are recorded both on the Hmax’ component.

Figure 3.14 shows the rays that are recorded by the Z’ component. The downgoing P is converted to downgoing S and effect the vertical component of the receiver because of its perpendicular particle motion. Also, the upgoing P wave effects the vertical component of the receiver since the particle motion of the wave is parallel to the direction of wave propagation. The total effect of the downgoing S wave and upgoing P wave effect the vertical component of the receiver and is therefore recorded by the Z’ component. Figures 3.15 – 3.17 show the Hmax' and the Z' component for the three selected offsets of the east walkaway VSP survey.

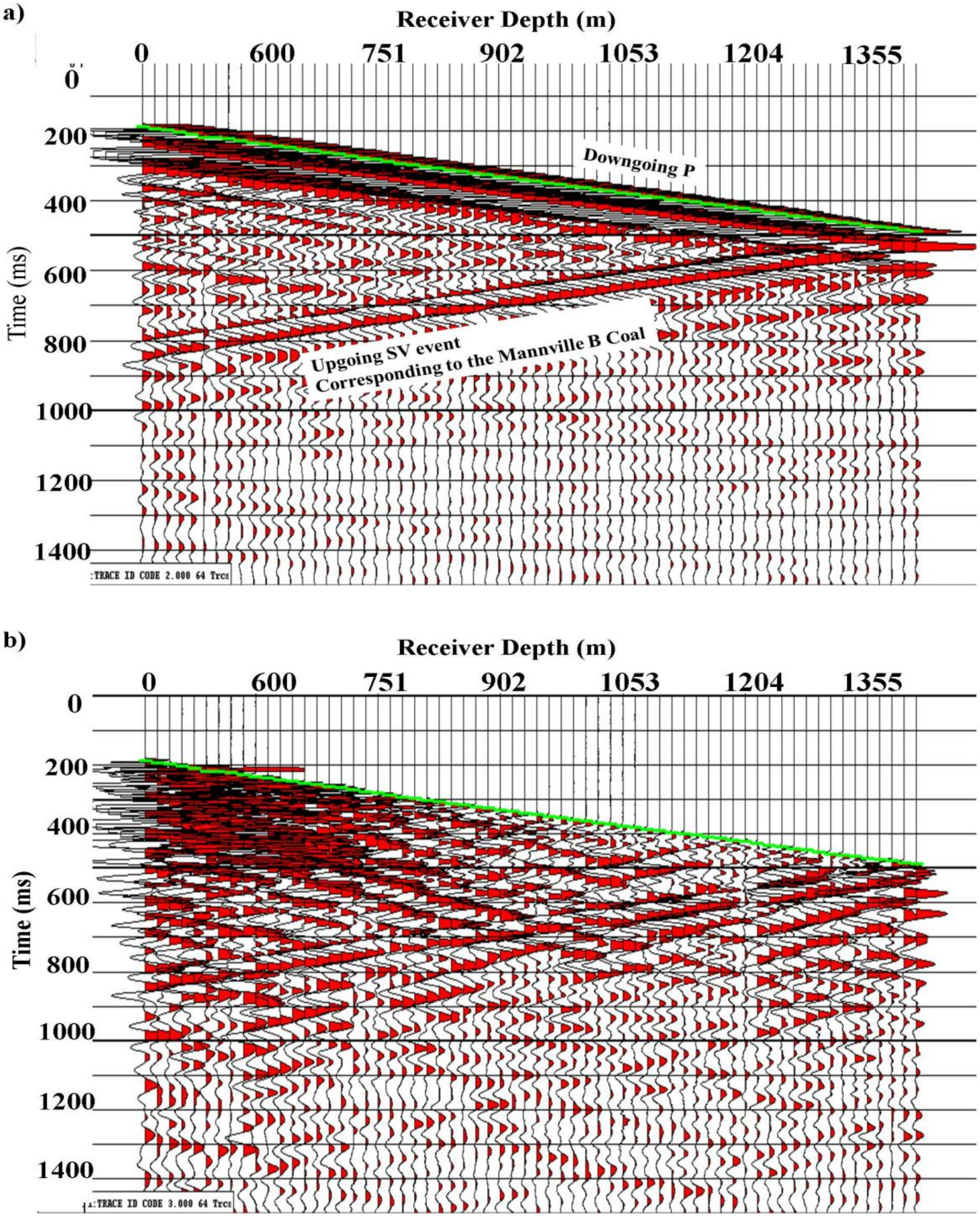

Figure 3.15: East walkaway offset 114 m a) Hmax' component b) Z' component.

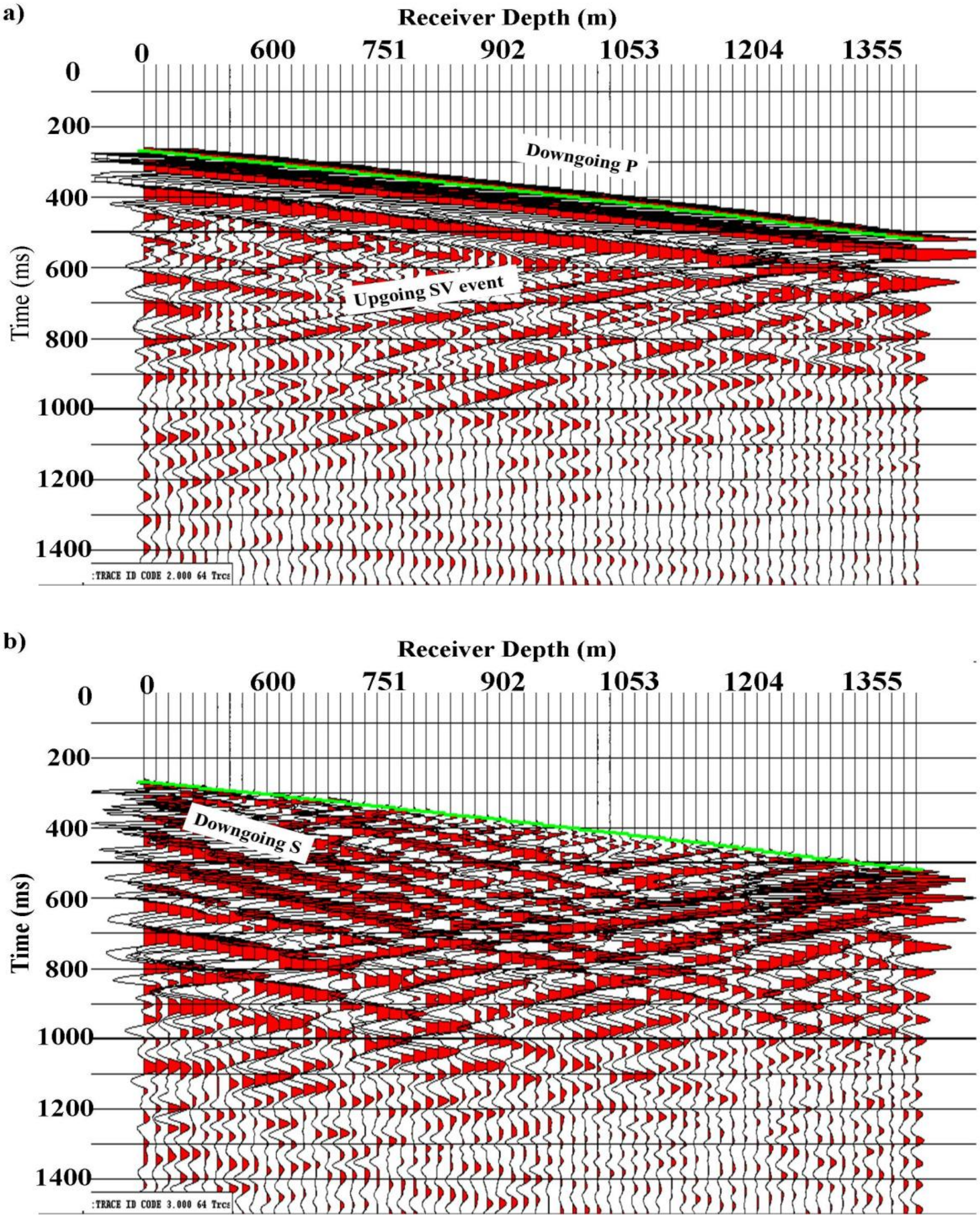

Figure 3.16: East walkaway offset 529 m a) Hmax' component b) Z' component.

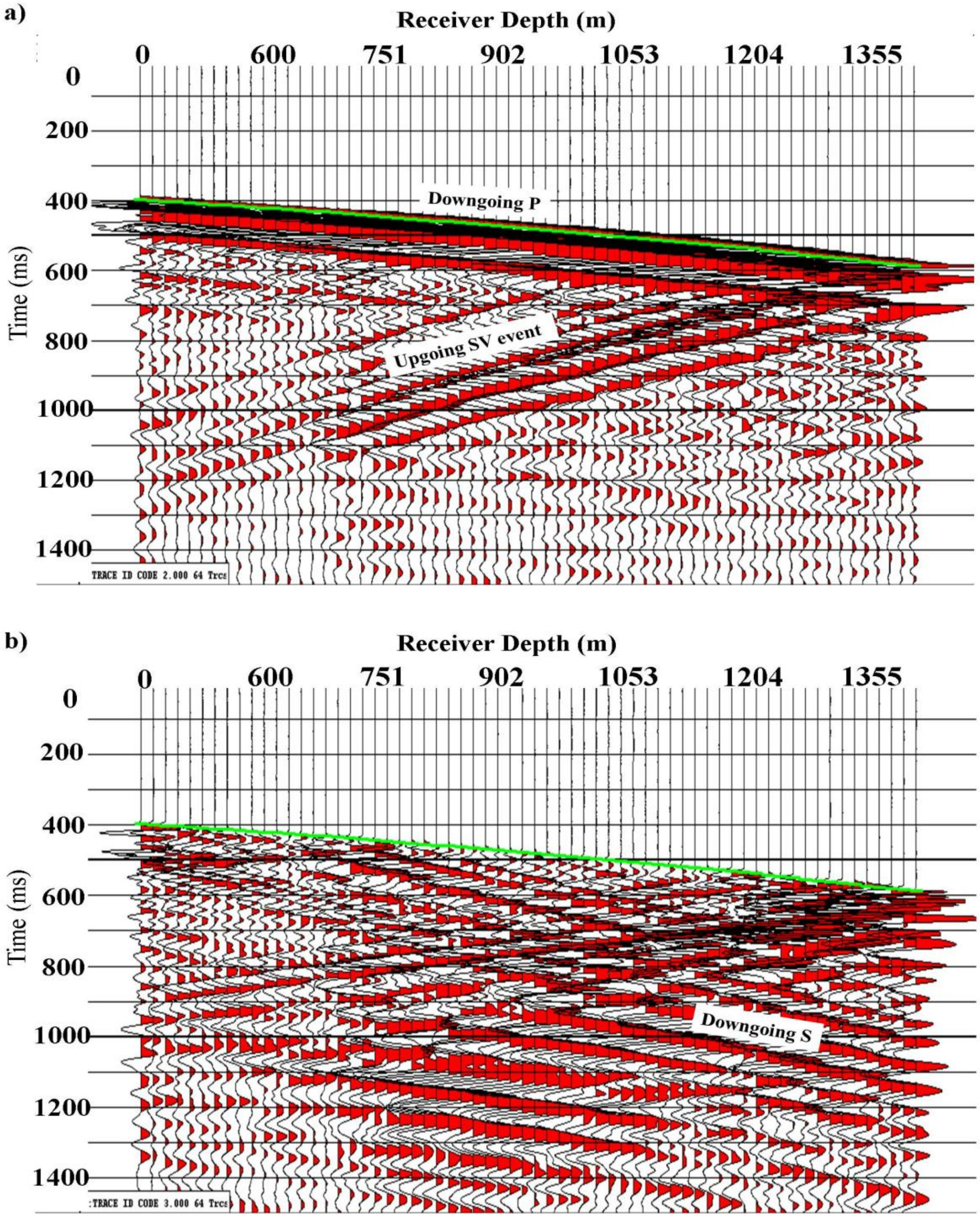

Figure 3.17: East walkaway offset 946 m a) Hmax' component b) Z' component.

The Hmax’ component clearly has dominant downgoing P waves when compared to the Z’ component. As the offset increases, the Hmax’ SV upgoing waves increase in amplitude. Starting from the offset 114 Hmax’ component, the most dominant reflection is the Mannville B coal and increases in amplitude at lower depths and offset.

On the other hand, the Z’ component has a different response with offset. The Z’ shows good downgoing SV waves and upgoing P waves at near offsets but shows a more mixed wavefield at farther offsets. As offset increases, the upgoing P waves become more difficult to distinguish since the dominant downgoing SV waves are superimposed on it. In addition, as offset increases, more shear waves come at later times of the VSP record.

3.7 Wavefield separation

The three component separation and two hodogram rotations yield the upgoing and downgoing P and SV wavefields. In a VSP survey, where data are expressed in time and depth of the receiver, seismic downgoing and upgoing waves interfere and overlay. Converting the data to FK domain, the upgoing and downgoing waves are separated (Hinds et al., 1999). The Hmax’ is used to obtain downgoing P waves, the Z’ component is used to obtain the downgoing SV waves and the Z and Hmax components are used to obtain the mixed P and SV upgoing waves (Hinds et al., 1999). To do all this, all the components are flattened to a 100 ms datum, which aligns the downgoing P waves along the zero wave number line in the FK domain making it all the more easier to separate the different wavefields since they plot in different areas of the FK domain. The flattened data plots the downgoing waves as horizontal events on the 100 ms datum. Also, the FK domain displays the upgoing and downgoing events as linear events with different slopes with the direct downgoing P waves aligned on the zero wave number vertical line. Figures 3.18 – 3.20 show the downgoing Hmax' also known as downgoing P.

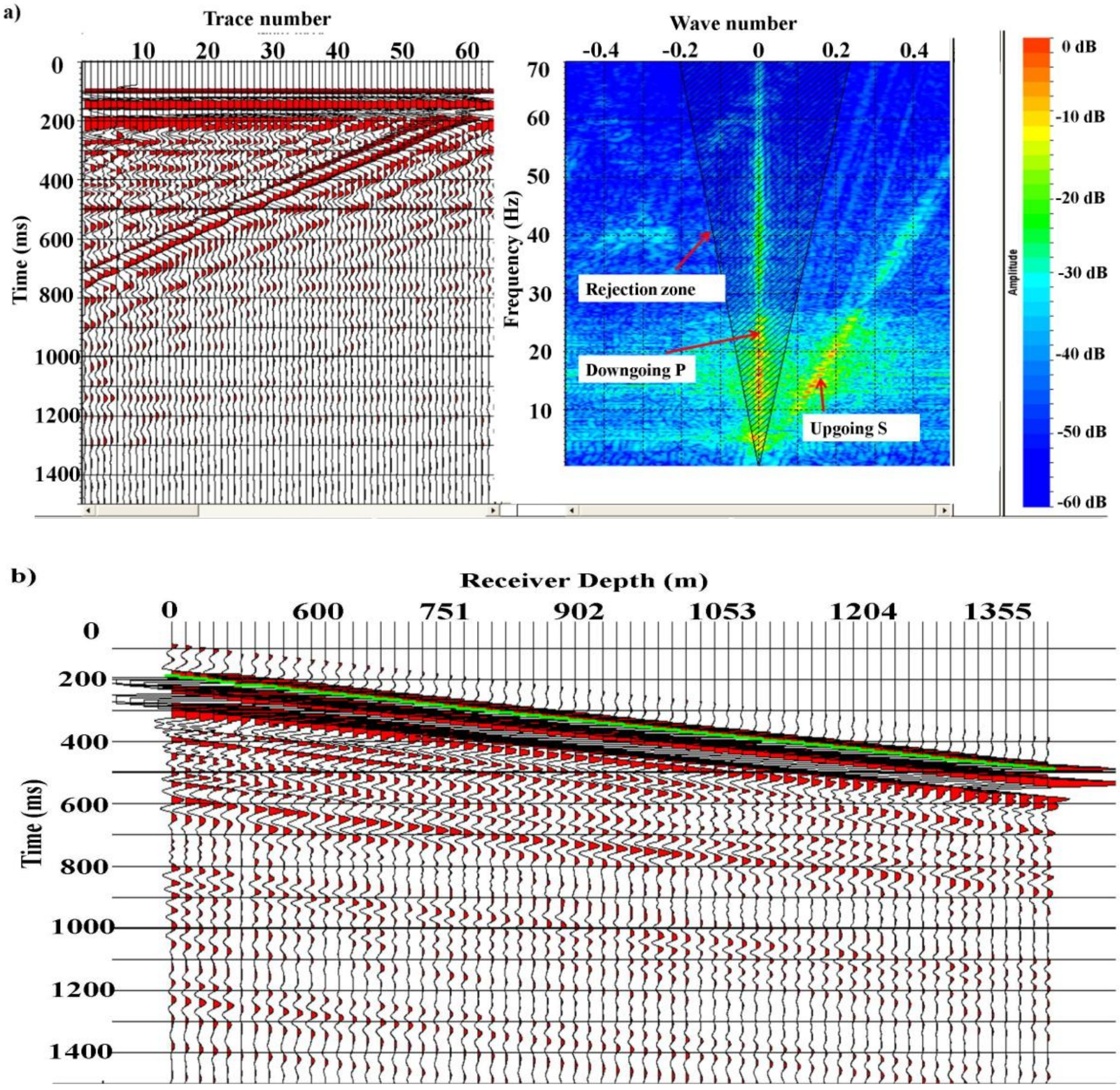

Figure 3.18: East Walkaway Offset 114 m Hmax' a) FK wavefield separation. The left window indicates the input flattened and padded wavefield. The right window shows the same input in the FK domain with the rejection filter around the downgoing P waves. b) downgoing P waves.

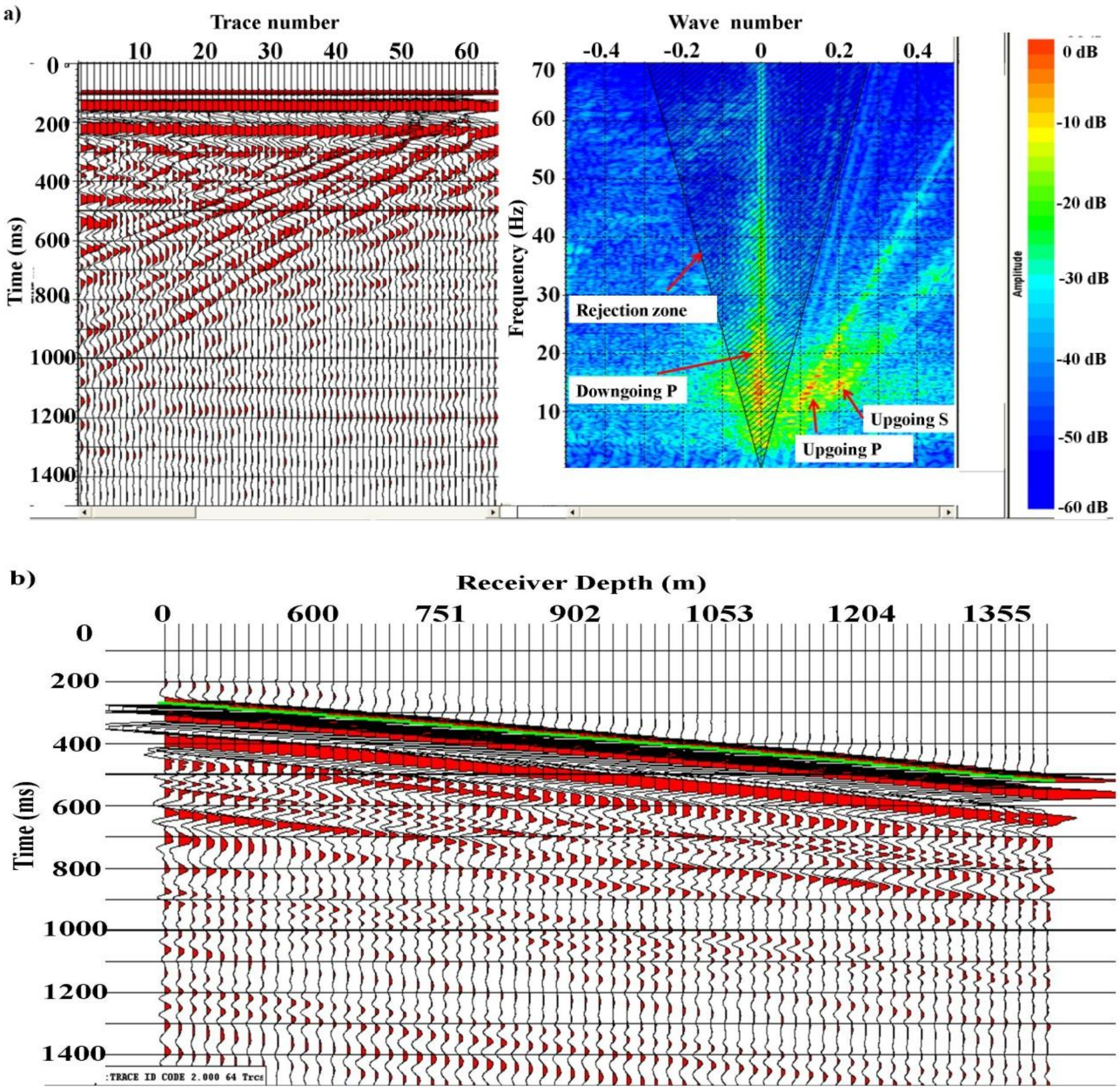

Figure 3.19: East Walkaway Offset 529 m Hmax’ a) FK wavefield separation. The left window indicates the input flattened and padded wavefield. The right window shows the same input in the FK domain with the rejection filter around the downgoing P waves.
b) downgoing P waves.

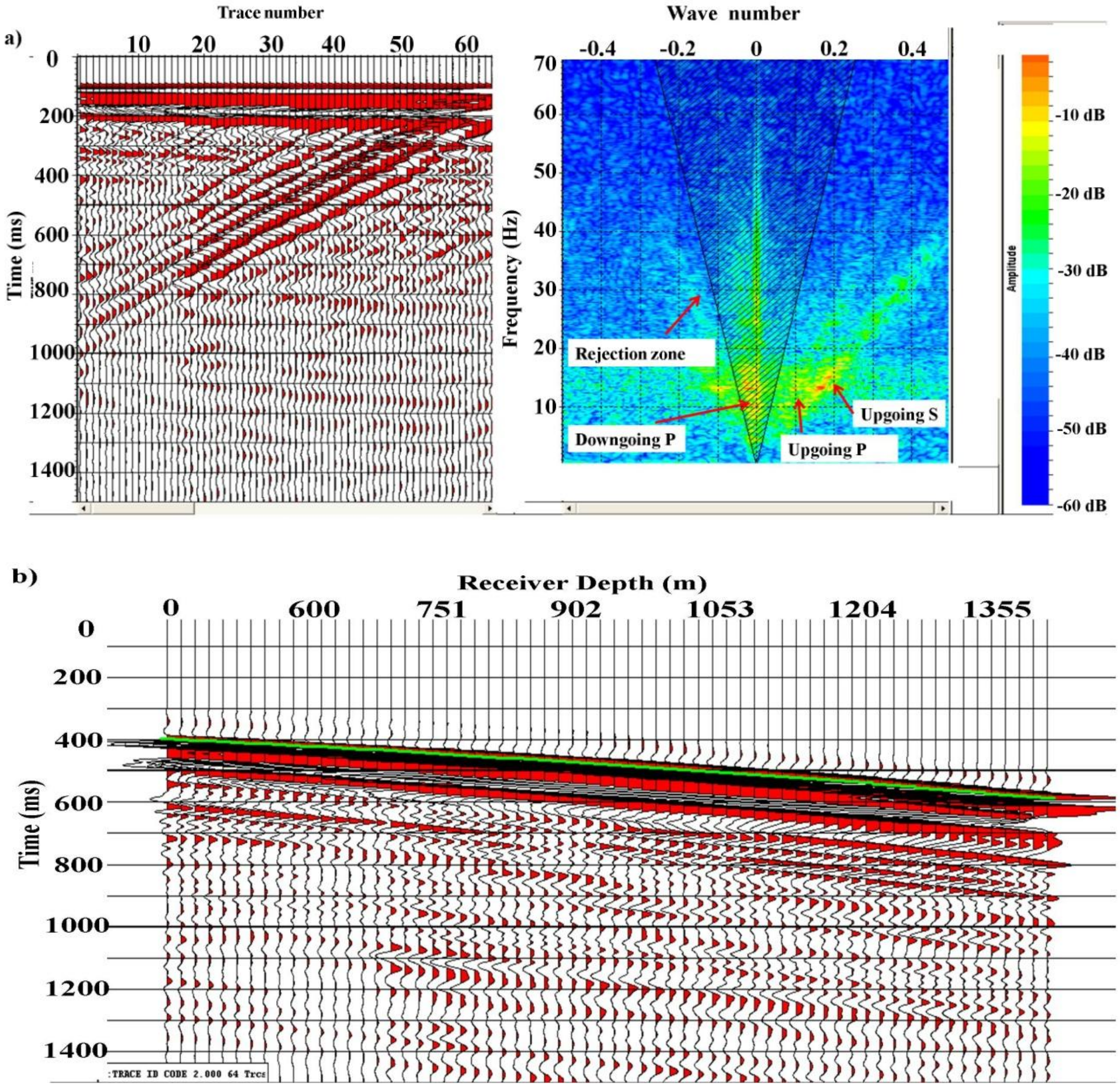

Figure 3.20: East Walkaway Offset 946 m Hmax’ a) FK wavefield separation. The left window indicates the input flattened and padded wavefield. The right window shows the same input in the FK domain with the rejection filter around the downgoing P waves.
b) downgoing P waves.

From Figures 3.18 to 3.20 it is clear that the FK wavefield separation did an excellent job of obtaining the downgoing P waves. The figures display the P downgoing waves and rejection zone. In addition, the figures show the upgoing P and SV waves.

Similar to the Hmax’, the Z’ component was also FK separated and the downgoing SV waves for the three east walkaway VSP are shown in Figures 3.21 – 3.23.

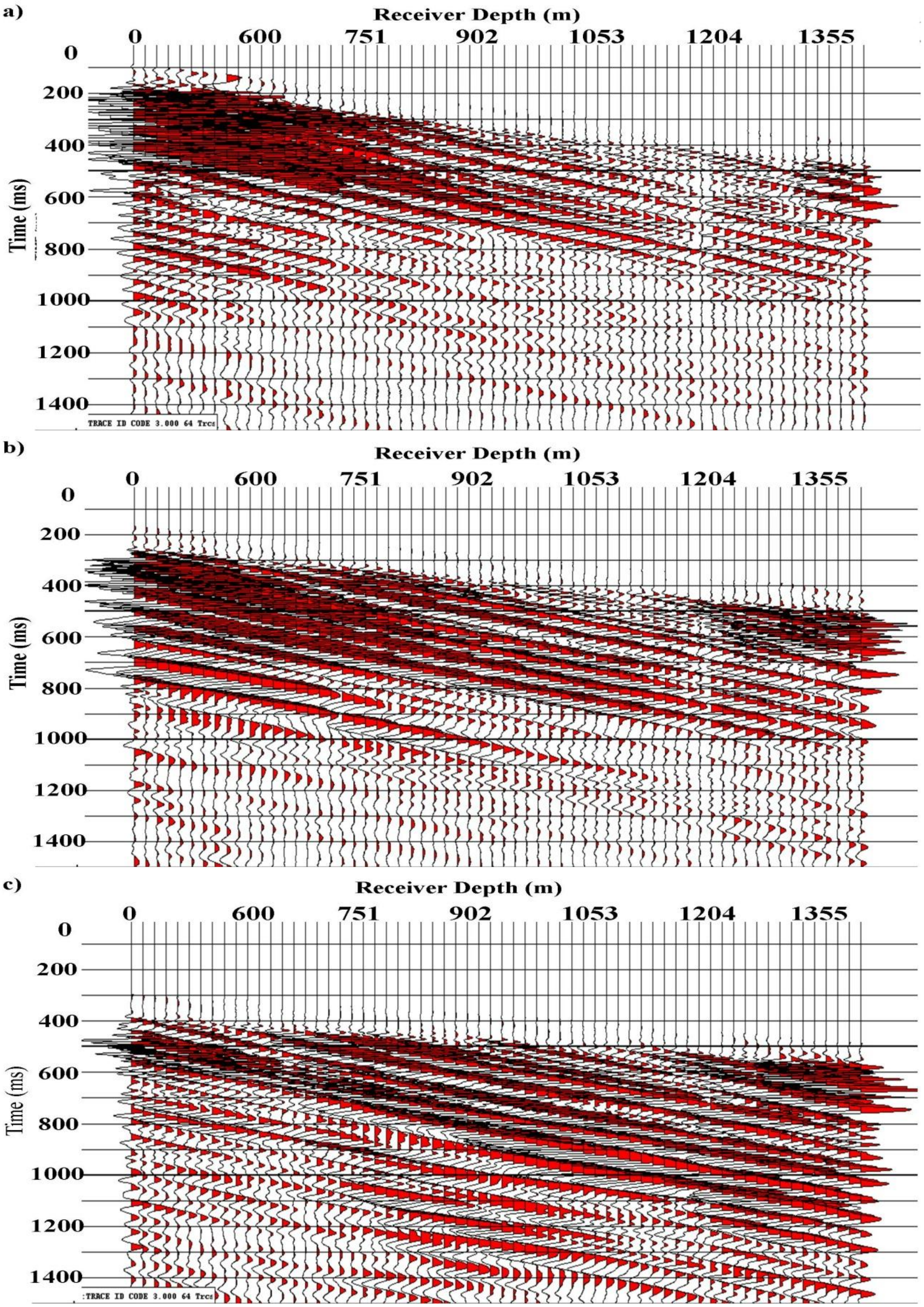

Figure 3.21: East walkaway offset SV downgoing wavefield for offsets a) 114 m b) 529 m and c) 946 m.

The SV waves were extracted successfully from the *Z’* component with FK filtering. The downgoing SV waves increase in amplitude as offset increases. In addition, shear waves are more noticeable at lower receiver depths as offset increases. This is because the lower receivers are closer to the reflectors. The shallow receivers do not record these high amplitude SV waves due to the attenuation of the waves as they travel to shallower depths.

3.8 Time Variant Rotation (TVR)

The upgoing waves were also separated using FK filtering. After wavefield separation, SV upgoing and P upgoing wavefields are input for time variant rotation. This step polarizes P waves on one component and SV waves on the other. The need for time variant rotation for P and SV isolation is due to the change of incident and reflection angle of different layers below a particular geophone. As a result, the angles of incidence from the reflected reflector to the upper geophone changes with time and therefore one angle of rotation is not adequate to isolate the P and SV waves (Hinds et al., 1999). Time variant rotation is undertaken after ray tracing for upgoing P and SV waves. Both the SV and P waves are used as input for time variant rotation for each offset. It is noted that in the time variant rotation, the upgoing P waves are reversed in polarity since in some cases the polarity is incorrect after hodogram rotations such as the one performed on Hmax in this case. Figures 3.22 – 3.24 show the FK filtered, time variant rotated upgoing P and SV waves.

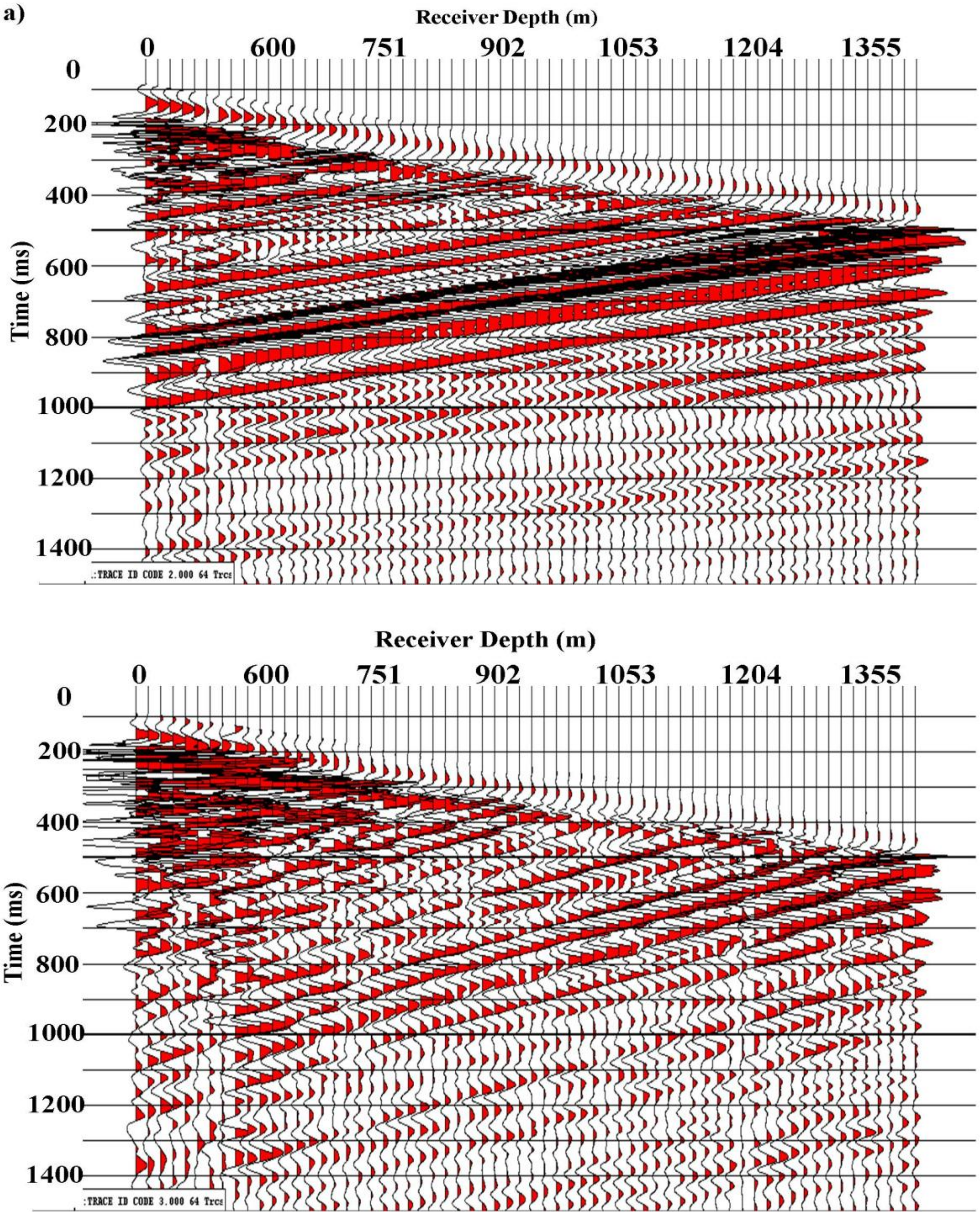

Figure 3.22: East walkaway time variant rotation at offset 114 m a) upgoing P. b) upgoing SV.

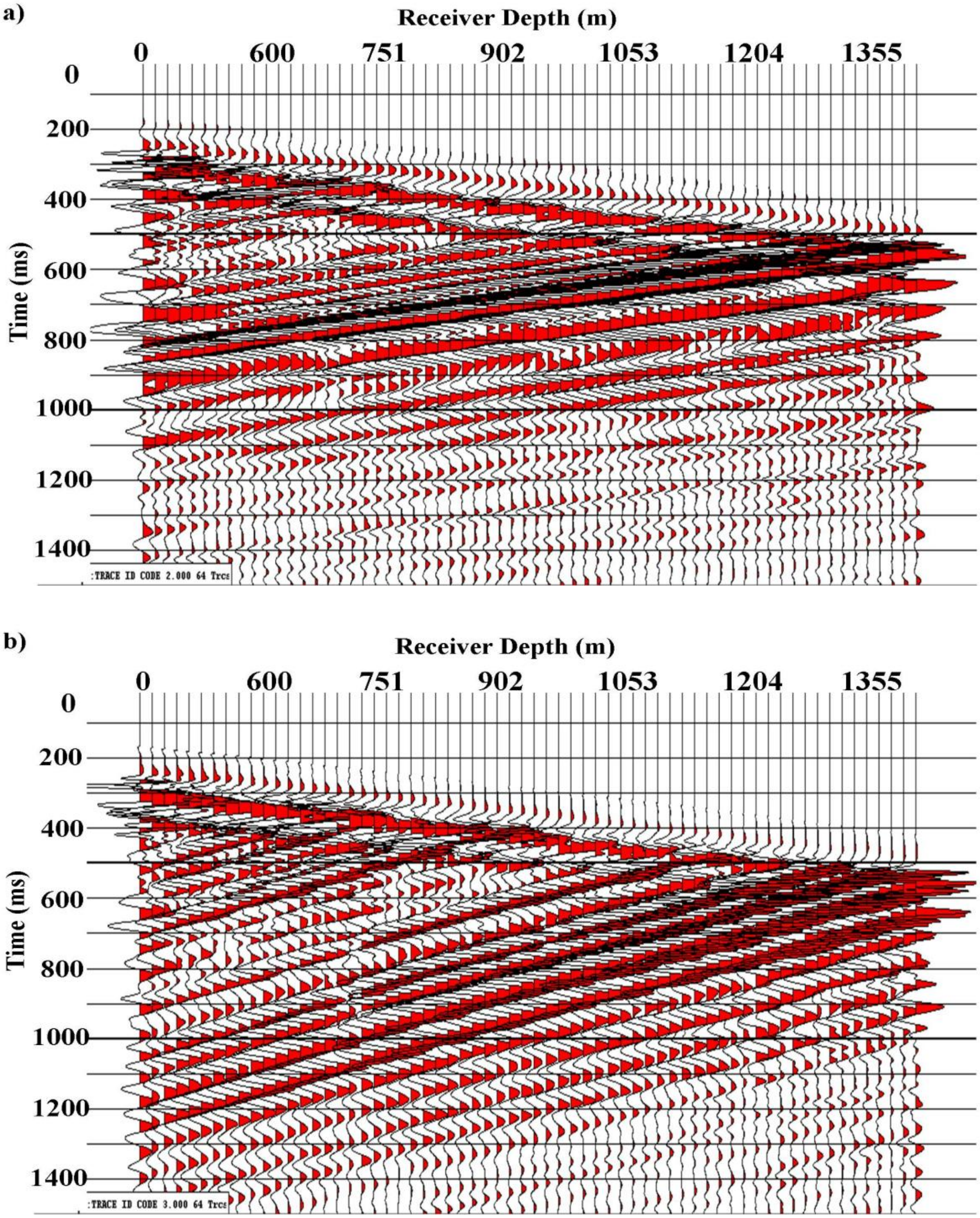

Figure 3.23: East walkaway time variant rotation at offset 529 m a) upgoing P. b) upgoing SV.

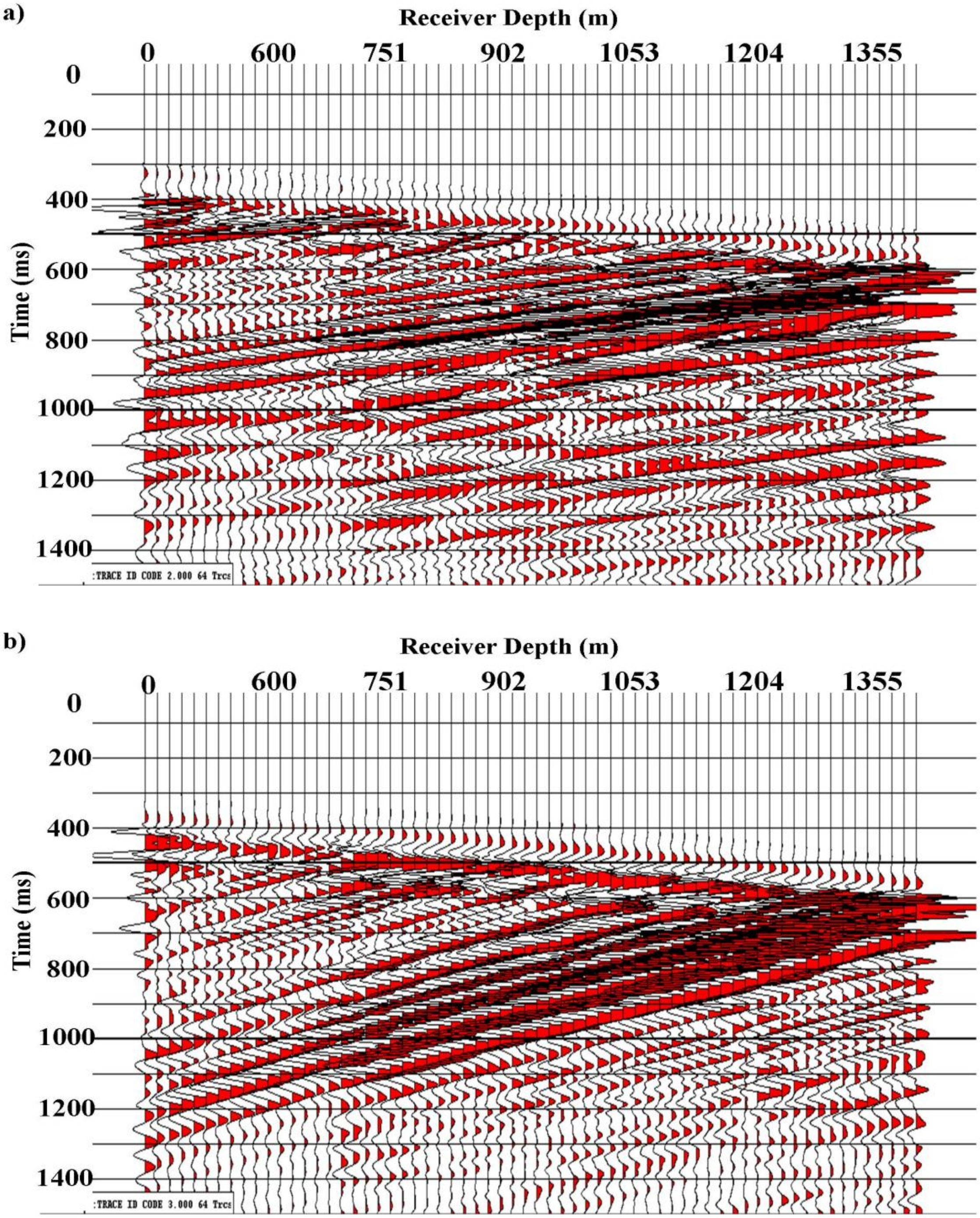

Figure 3.24: East walkaway time variant rotation at offset 946 m a) upgoing P. b) upgoing SV.

Figures 3.22 to 3.24 show that the time variant rotation has successfully separated the upgoing P and SV waves. The upgoing P waves now have better defined reflections at shallow receivers and smaller offsets. As offset increases, the P wave reflections decrease in amplitude and become less well defined at deeper receivers.

On the other hand, the SV wave reflections increase in magnitude as offset increases. This increase in magnitude is consistent with the Zoeppritz model results shown in Figure 3.7 where the PS reflection increases in reflection coefficient with the increase of incident angle. Also, the SV waves increase in amplitude for the lower receivers. The lower receivers are closer to the reflectors and record these waves while the S upgoing waves are attenuated as they propagate to shallower depths.

3.9 Deconvolution

After separation of both P and SV upgoing wavefields, deconvolution was applied. Deconvolution is performed in order to obtain the reflectivity of each layer. This is done by removing the source wavelet from the seismic trace. This wavelet is estimated since the downgoing waves are considered to represent the source wavelet. A deconvolution window of 250 ms was chosen to apply to both the downgoing and upgoing wavefields. As with the zero offset VSP deconvolution, the deconvolution operator is designed on the downgoing P waves and applied to the upgoing waves. A filter of 5-10-70-80 Hz was applied to the output of the deconvolution. Figures 3.25 – 3.27 show the result of deconvolving a near, mid and far offset of the east walkaway P and SV upgoing waves.

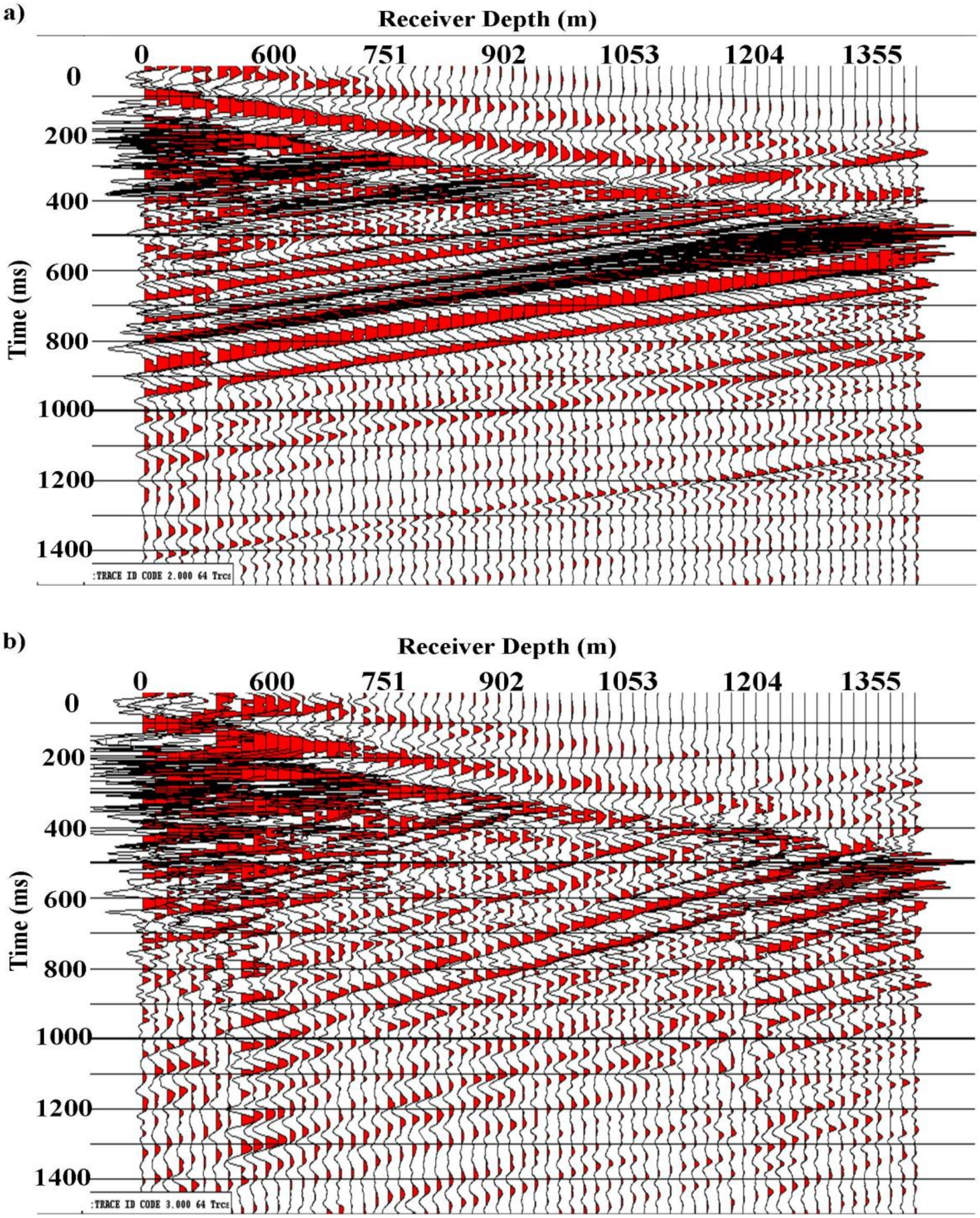

Figure 3.25: East walkaway offset 114 m deconvolved upgoing a) P waves. b) SV waves.

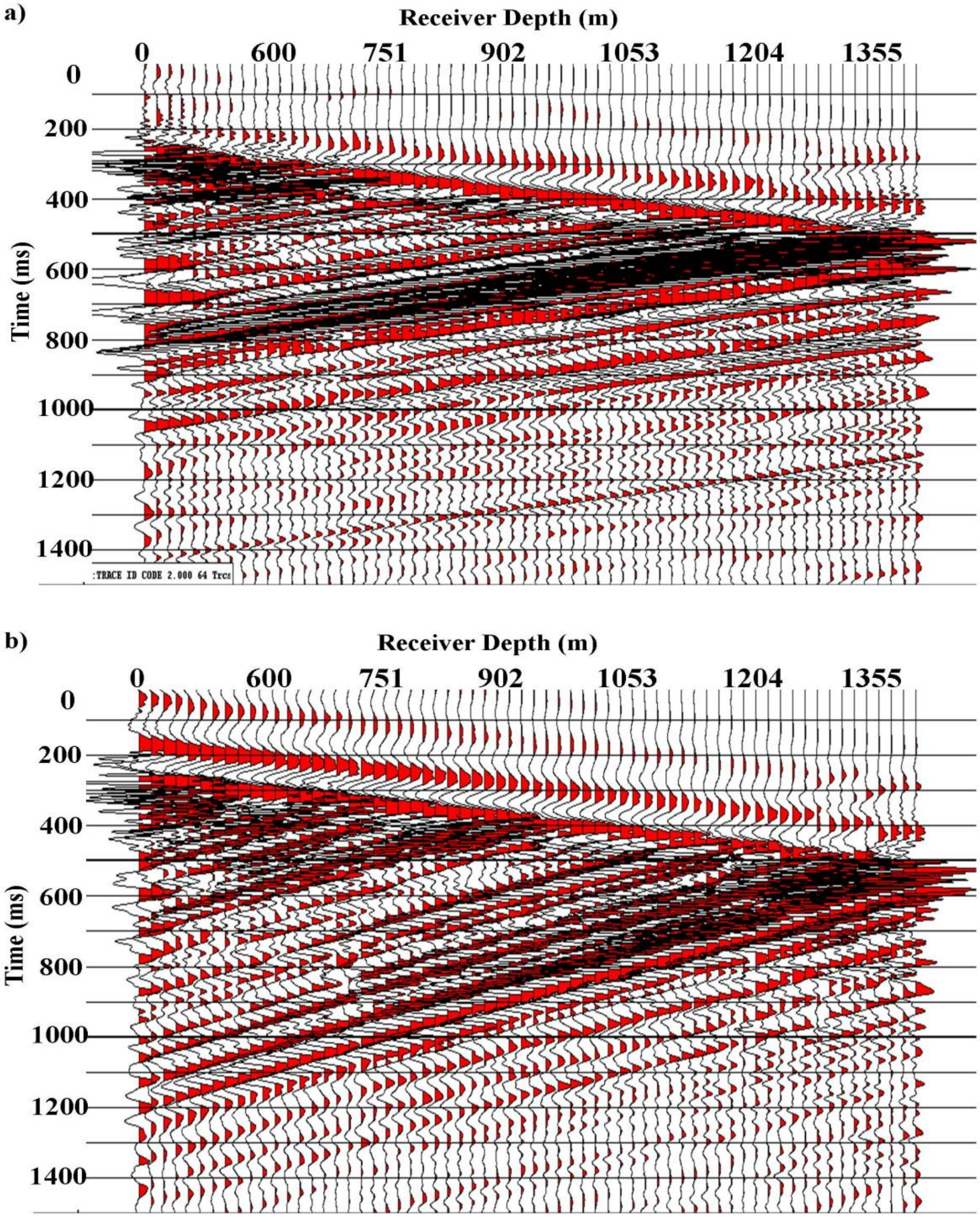

Figure 3.26: East walkaway offset 529 m deconvolved upgoing a) P waves. b) SV waves.

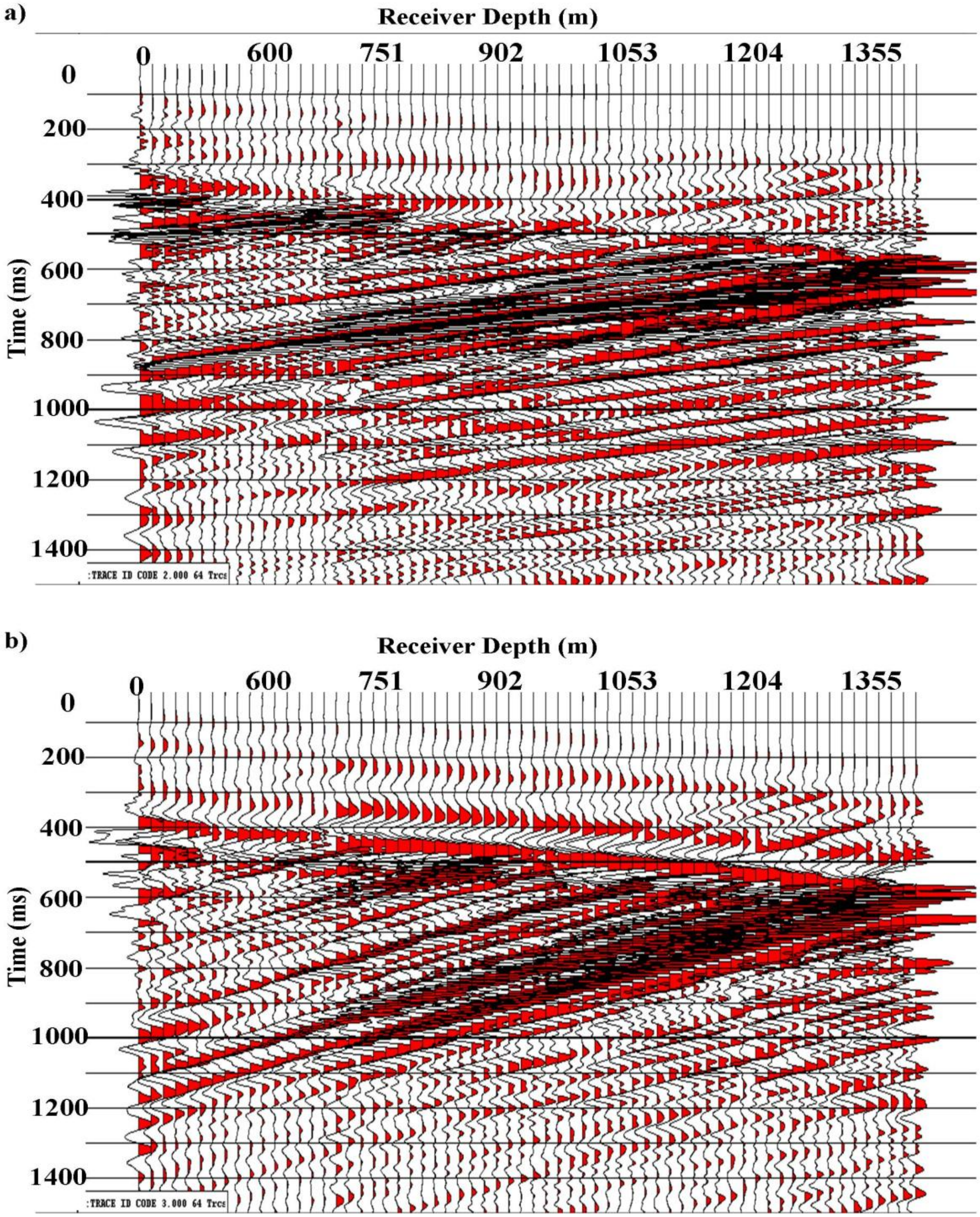

Figure 3.27: East walkaway offset 946 m deconvolved upgoing a) P waves. b) SV waves.

The upgoing deconvolved P waves show a consistent behavior with offset. As offset increases, the P wave amplitudes decrease. However, after deconvolution, the upgoing events are much better defined and have a higher bandwidth than those after the Time Variant Rotation (TVR) for the same offsets. Some noise is also introduced to the deconvolved data.

For the deconvolved upgoing SV waves, the amplitudes of the SV waves increase as offset increases. The deconvolved upgoing SV waves are better defined after deconvolution especially with increasing offset. At near offsets, there is little SV energy in the shallow receivers and not much in the deeper receivers. However, the amplitudes of the SV waves increase at deeper receivers as offset increases. As mentioned earlier, the deeper receivers are closer to the reflected SV waves and therefore record the SV wavefield. The reflected SV wavefield attenuates as it propagates back towards the surface. Similar to the deconvolved upgoing P waves, some noise is introduced as a result of the deconvolution process.

3.10 VSPCDP and VSPCCP

The terms VSPCDP and VSPCCP stand for Vertical Seismic Profile Common Depth Point and Vertical Seismic Profile Common Conversion Point. The last processing steps to be applied to the upgoing P and SV wavefields was Normal Moveout (NMO) correction, followed by VSPCDP and VSPCCP stacking. VSPCDP stacking essentially maps the upgoing VSP reflections into a psuedoseismic section that relates the VSP data to offset instead of receiver depth, from the farthest point of reflection determined by VSP geometry and velocity to the borehole (Hinds et al., 1999). A succession of reflection points can be mapped laterally (Hardage, 1985). The VSPCCP mapping is similar to that of the VSPCDP mapping. The difference between the two mappings is that the VSPCCP mapping deals with converted P-SV waves which have different raypaths than the P-P waves (Stewart, 1991). Figure 3.28 shows an illustration of the lateral reflection point coverage of a VSP survey.

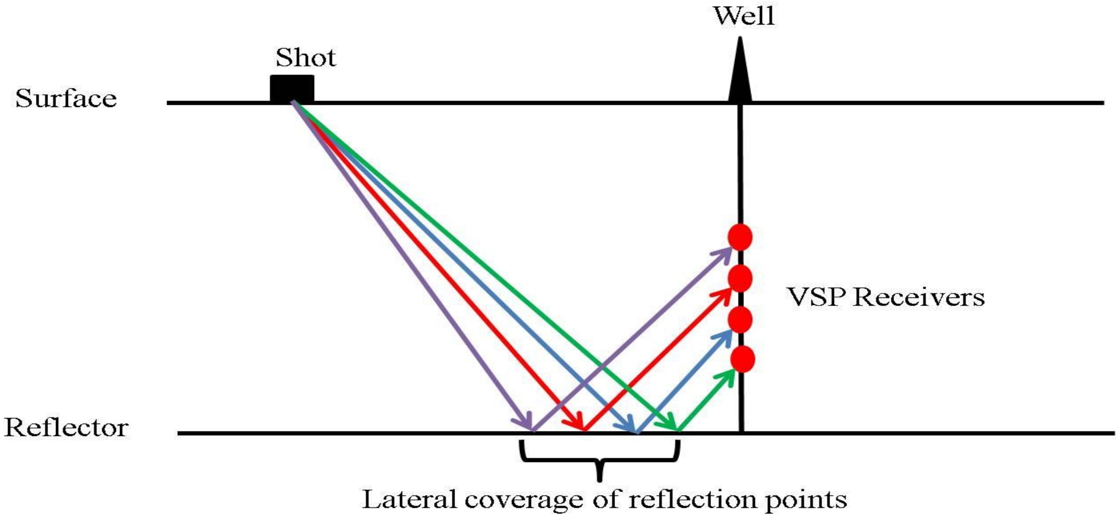

Figure 3.28: An offset VSP survey highlighting the lateral coverage of reflection points used in VSPCDP or VSPCCP stacking (Modified from Hartse and Knapp, 1990).

The lateral offset coverage obtained from a VSP survey depends on the geometry of acquisition of the survey. The lateral coverage increases as the wellbore-shot offset increases. In addition, the lateral coverage of a VSP survey increases and becomes closer to the wellbore as the receiver depths are closer to the target reflection event (Hartse and Knapp, 1990). In addition, as the reflector depth of a multi layer reflectors increase, the horizontal reflection points approach the midpoint between the source and receiver assuming horizontal isotropic layers and vertical borehole (Dillon and Thomson, 1984).

All of the upgoing P and SV waves were used as input to the VSPCDP and VSPCCP mapping process. The upgoing P and SV wavefields were corrected for gain and then NMO corrected using the zero offset VSP interval velocities calculated from the zero offset VSP Z raw data. The wavefields were then filtered with a 5-10-70-80 Hz filter to reduce noise. Next a median filter of 4 points was applied to enhance signal to noise ratio. Another bandpass filter of 5, 10, 70, 80 Hz was applied before the data was CDP or CCP mapped.

In VSPCDP, the times of the events on VSP traces are correlated to the common depth points in the subsurface and these points are stacked together. The stacked common depth points are related to a subsurface event and displayed in two way time that can be related to surface seismic data (Wyatt and Wyatt, 1984).

The VSPCDP and VSPCCP sections obtained from the three walkaway VSP datasets are shown in figures 3.29 – 3.31.

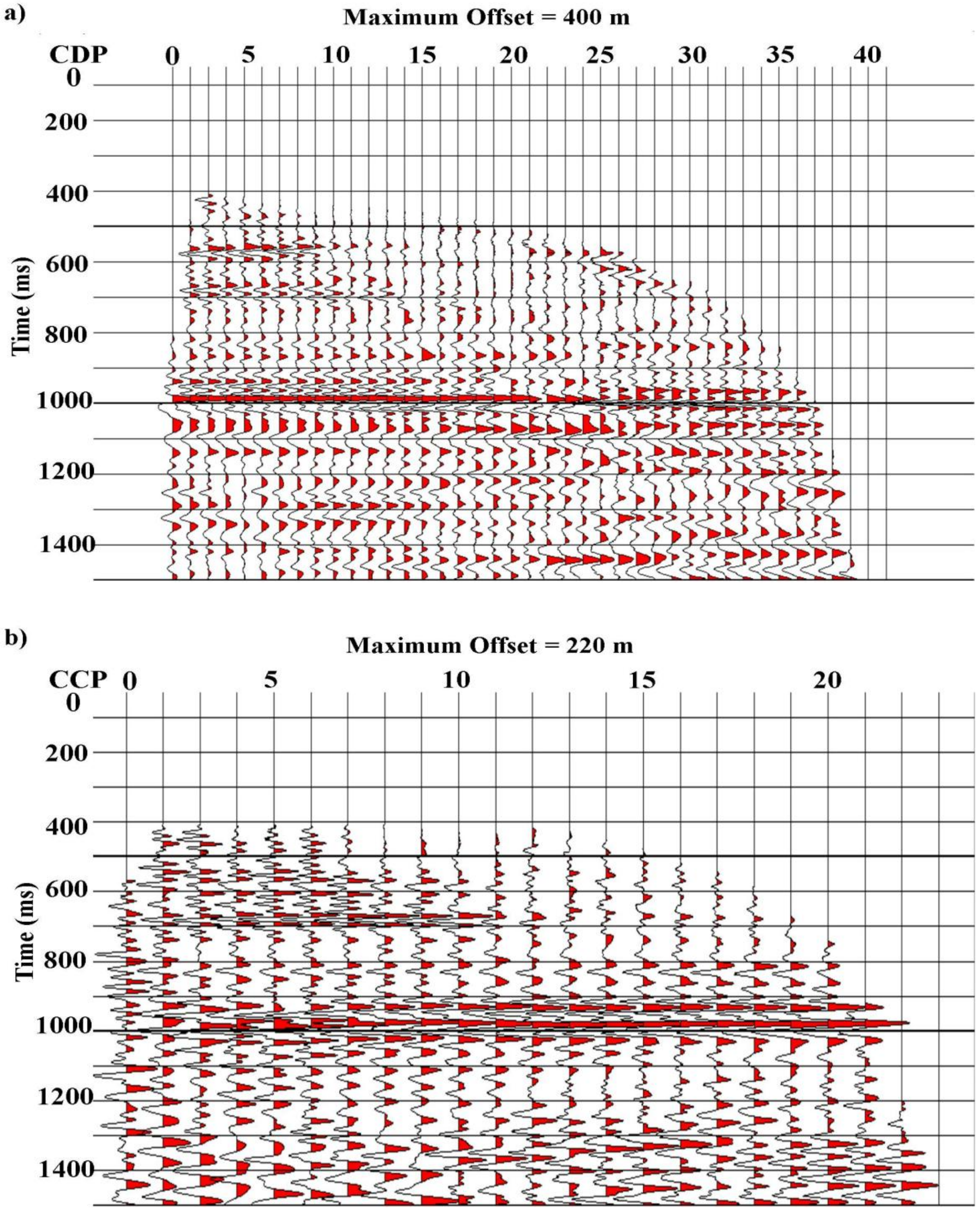

Figure 3.29: East walkaway multi offset a) VSPCDP. b) VSPCCP.

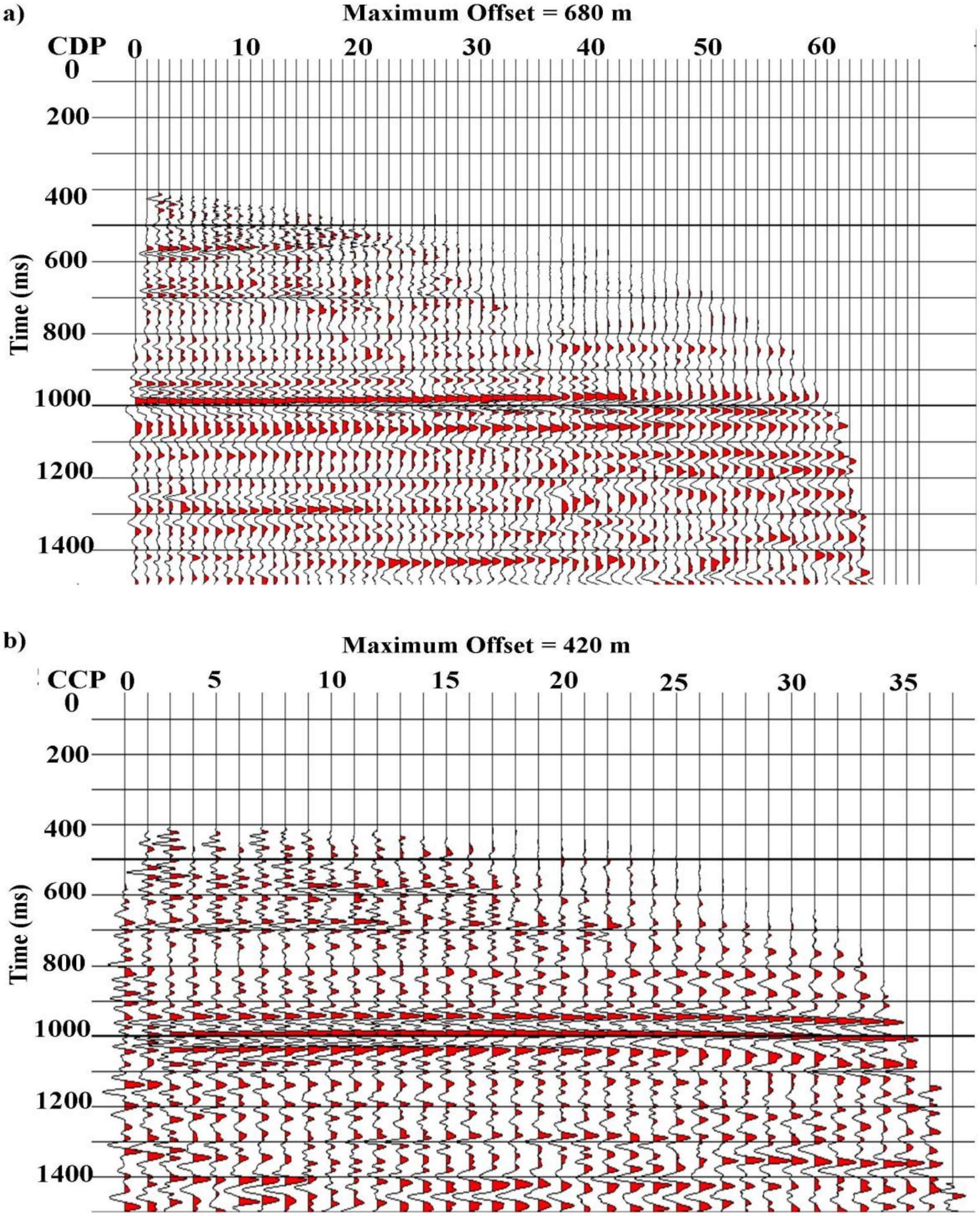

Figure 3.30: Southeast walkaway multi offset a) VSPCDP. b) VSPCCP.

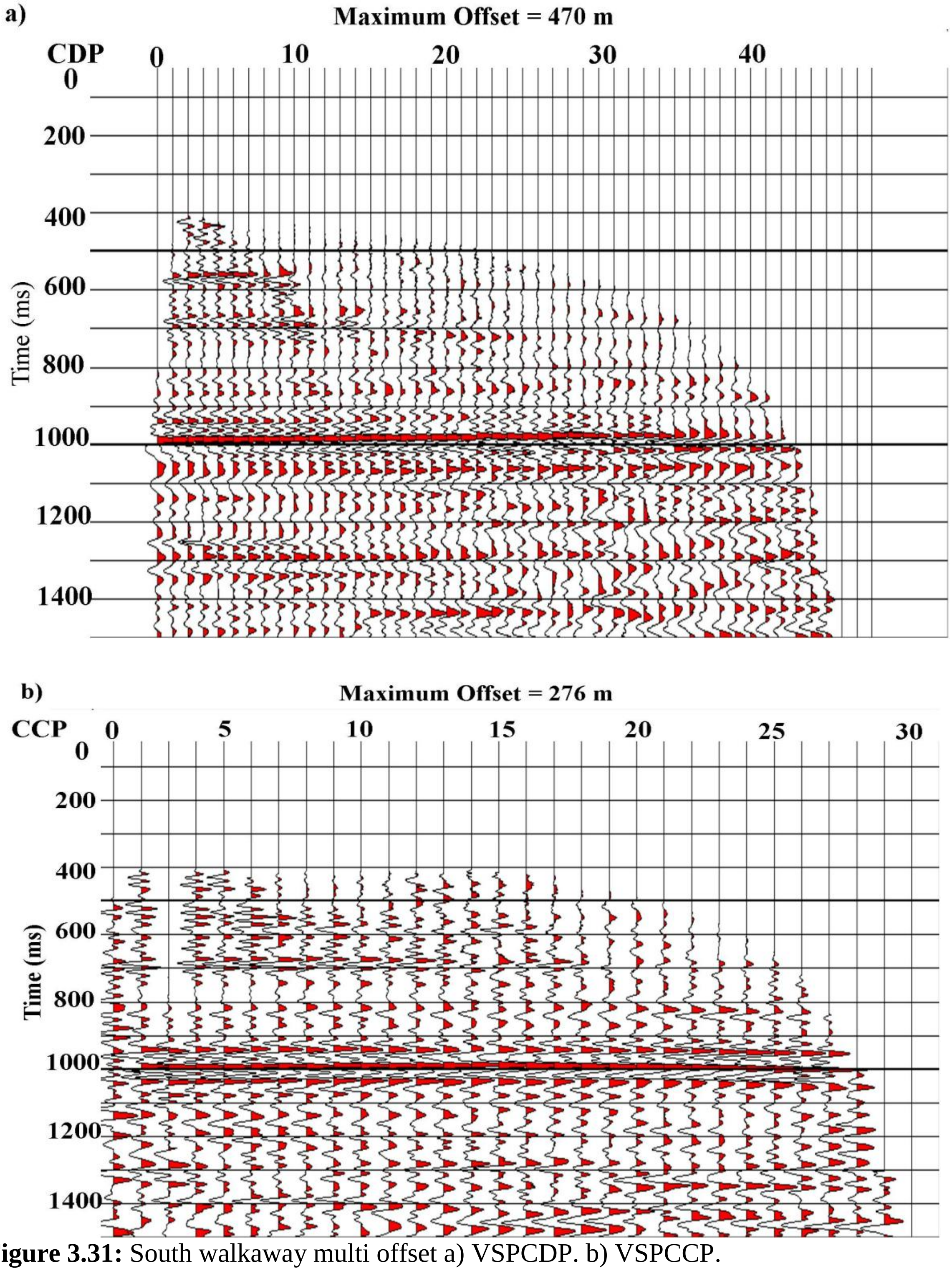

Figure 3.31: South walkaway multi offset a) VSPCDP. b) VSPCCP.

The VSPCDP and the VSPCCP stacks that the most dominant reflection is that from the Mannville coals at 1000 ms. Another obvious conclusion is that the VSPCDP wave reflection stacks have high amplitudes at near offsets and grow weaker at far offsets. The south and southeast VSPCDPs show slightly more sharper reflections from the Mannville B coals. In contrast, the SV wave reflections from the Mannville B coals increase in amplitude as the offsets increase.

3.11 Discussion

The first break picking of the offset VSP data lead to the development of the offset interval velocity models, which showed initially that there was a shot static problem between each placement of the receiver tools. The problem was solved by adding constant times and bulk shifting a range or first break receiver data. A recommendation is made to have an overlap of at least one receiver to remove this problem in the future.

Two hodogram rotations were performed to isolate the downgoing wavefields in the plane of the source and well. The focus was to isolate the downgoing P waves in the Hmax' component and to isolate the downgoing S waves in the Z' component. In order to separate the different wavefields, FK filtering was chosen as a method of separation. Flattening the components to their first break times aligned the downgoing P on the zero wave number axis and this allowed the separation of the different wavefields. The FK filter was successful in isolating the downgoing P and downgoing S waves.

Time variant rotation is taken in order to isolate the upgoing P waves and upgoing S waves from the Z and Hmax components respectively. This is because the reflection angle varies with increasing depths for upgoing reflections. The upgoing P waves have larger amplitudes and coherent reflections at shallow depths and near offsets, and amplitudes decreased with offset. On the other hand, the upgoing S waves had better coherency and higher amplitudes at larger offsets and greater depths. Both the upgoing P and upgoing S waves showed a high amplitude reflection from the Mannville B coals.

After separating the different wavefields, a deconvolution operator was designed on the downgoing waves and applied to upgoing waves. The VSP surveys give an advantage of measuring the source wavelet from downgoing waves to give a better deconvolved result for the upgoing waves. The upgoing waves showed a sharper reflection after deconvolution and eliminated, if any, significant multiples.

Finally the process of VSPCDP and VSPCCP mapping gave the P-P and P-SV reflection response of the Mannville B coals with offset from the well. All of the VSPCDP and VSPCCP mapping showed high amplitude reflections at 1000 ms corresponding to the Mannville B coals. The VSPCDP reflection showed stronger amplitudes in near offsets and decreased as the offset increased. On the other hand, the VSPCCP reflection showed a weak reflection in the near offsets and increased in amplitude with far offsets because of more converted energy.

CHAPTER 4: AVO ANALYSIS

4.1 Introduction

In exploration seismology, the ultimate goal is to image the subsurface using geophysical methods in the search of hydrocarbons. However, a risk exists in finding hydrocarbons in the subsurface or not. Therefore, geoscientists look for Direct Hydrocarbon Indicators (DHI) as guidance for indications of the existence of hydrocarbons. For example, the term “Bright Spots” suggests high seismic amplitudes in seismic sections that could indicate the presence of gas in the section. However, wells were drilled on the basis of these bright spots and the results were dry holes. In these cases, the bright spots existed because of lignites, carbonates and hard streaks, wet sands and igneous intrusions. Ostrander (1984) discovered that seismic reflections from gas-bearing sands produced amplitude anomalies with increasing offset, and he later paved the way to analyze these anomalies as a DHI. The study was later labelled as Amplitude Variation with Offset (AVO) (Lines and Newrick, 2004).

In AVO analysis, the amplitudes of seismic waves are assessed in Common Midpoint Gathers (CMP). One aspect of AVO in clastic rocks focuses on the differences in reflected P wave and converted S wave velocities from a gas bearing sand over shale in contrast with a gas bearing sand over a wet bearing sand formation (Lines and Newrick, 2004).

P wave and S wave velocities are linked closely to rock properties. Of course, rock properties are of interest because of geoscientists’ desire to link wavefield velocities to reservoir zones. Such reservoir properties are the Lame parameters λ and μ which represent a rock’s incompressibility and rigidity respectively. Incompressibility determines how susceptible a rock is to be compressed. Generally, clastic rocks become more incompressible with oil and water in the pore-fluid spaces than if gas is in the pore spaces. Rigidity on the other hand relates a rocks ability to withstand shear stress. In theory, shearing of a rock leaves the pore spaces relatively unaffected and therefore is independent of pore fluid types and can be used for lithological characterization. An additional property of density ρ is needed to arrive at the equations relating the P and S wave velocities to the Lame parameters (Lines and Newrick, 2004).

$$V_P^2 = \frac{(\lambda + 2\,\mu)}{\rho}$$

$$V_S^2 = \frac{\mu}{\rho}$$

The basic relationships between impedances and Lame parameters are as follows (Goodway 2001):

$$\lambda = \rho V_P^2 - 2\rho V_S^2$$

$$\mu = \rho V_S^2$$

$$\lambda\rho = I_P^2 - 2I_S^2$$

$$\mu\rho = I_S^2$$

Where:

λ = incompressibility

μ = rigidity

ρ = density

Ip = P wave impedance

Is = S wave impedance

4.2 Crossplotting

A common way of interpreting AVO data is via crossplotting. AVO crossplotting includes a variety of attributes one of which is the AVO intercept versus AVO gradient plots. The point of these attributes is to find anomalies in the data. The amplitude variation with offsets for upgoing seismic data is plotted as points with color coding to distinguish different anomalies at different times of the data. These data points can then be used to deduce information on seismic sections (Simm et al, 2000). The (A) AVO intercept and (B) AVO gradient are attributes that are obtained from approximations of the Zoeppritz equations. The gradient (B) is calculated through the rate of change of the amplitude across a gather. While the intercept term (A) is the zero offset amplitude obtained from extrapolating the AVO gradient (Ross, 2009). In other words, the (A) intercept is the normal incidence P wave reflection coefficient. The intercept (A) and gradient (B) are inversely correlated for background rocks but may be positively correlated for shallow sediments with high Vp/Vs ratios (Castagna et al, 1998).

The (A) intercept and (B) gradient are related to the Shuey approximation given by the following equation (Li et al., 2007):

$$R(\theta) = R_p + G\, sin^2(\theta) + C\, (tan^2(\theta) - sin^2(\theta))$$

Where R_p is the normal incidence zero offset P wave reflectivity. The variable G corresponds to the gradient measuring the change in seismic impedance from one time sample to another from each angle of incidence. Then dependant angle θ is the incident angle and R(θ) is the reflectivity dependent on the incidence angle. This three term Shuey equation represents a normal incidence term, a near incidence term and a far incidence term and is directly related to rock properties through Poisson's ratio (Lines and Newrick, 2004). The third term is neglected for angles over 25 degrees to become the two term Shuey equation (Li et al, 2007). In the equation above the R_p term corresponds to the A intercept and the G term corresponds to the B gradient term. The AVO attributes are normally plotted quadrants to distinguish their anomaly type. Figure 4.1 shows the AVO quadrants and crossplot classes.

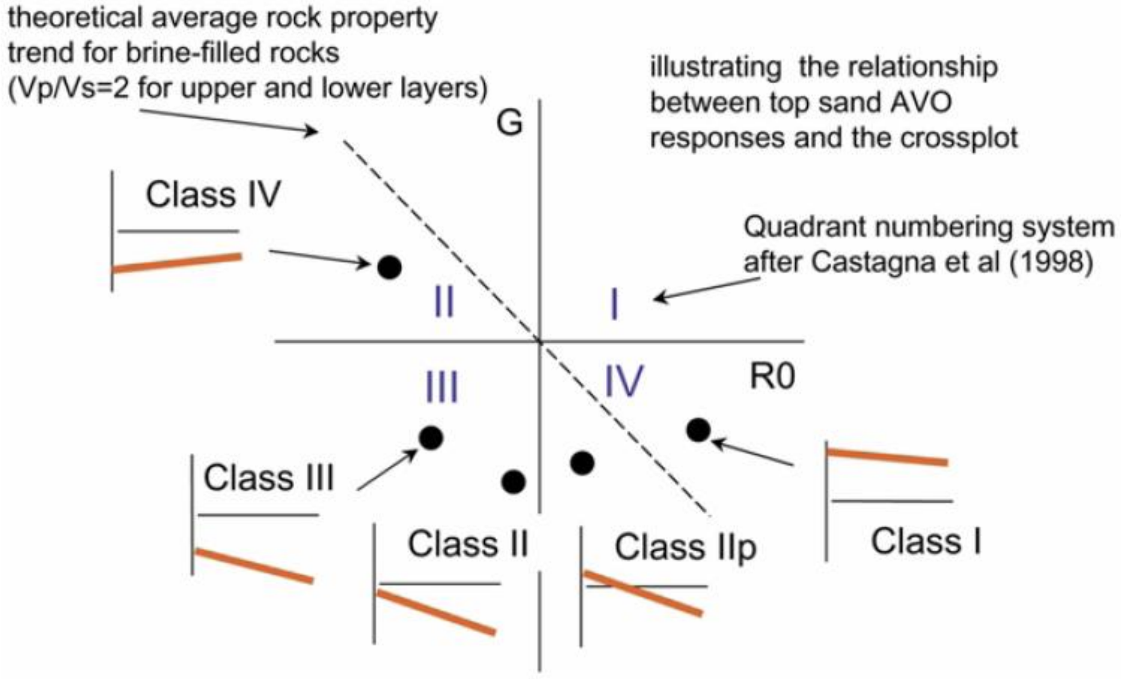

Figure 4.1 AVO quadrants and AVO classes (from Simm et al, 2000).

Figure 4.1, a hypothetical line is calculated based on brine filled rock properties called the “fluid line”. Later realizations indicated that hydrocarbon bearing data points plot to the left of this line. The hydrocarbon bearing data creates a cluster of data and not a trend left of the brine bearing formation data (Simm et al, 2000). Table 4.1 indicates the classification of the AVO anomalies.

Table 4.1: AVO classifications, quadrants and signs (modified from Castagna and Swan, 1997).

Class	Relative Impedance	Quadrant	A	B	Amplitude vs Offset
I	Higher than overlaying unit	IV	Positive	Negative	Decreases
II	About the same as the overlying unit	II, III or IV	Positive or Negative	Negative	Increase or decrease; may change signs
III	Lower than the overlying unit	III	Negative	Negative	Increases
IV	Lower than the overlying unit	II	Negative	Positive	Decreases

In AVO crossplotting of intercept versus gradient curves, the AVO trend lines are assumed to be relatively tight in compacted rocks with a low Vp/Vs ratio and may be rotated in unconsolidated rocks with high Vp/Vs ratios (Pelletier, 2008 and Castagna et al. 1998). In practice, most seismic data does not behave in a tight background trend because of seismic processing algorithms that produce the AVO gathers (Pelletier, 2008). Modeling of data and crossplotting is an aids the locating of hydrocarbon anomalies in the data (Ross, 2000). Crossplotting trends behave as expected in well consolidated rock with Vp/Vs ratios between 1.6 - 2.4 (Pelletier, 2008). In theory, the larger the effect hydrocarbons have on the Vp/Vs ratio, the farther away the hydrocarbon cluster is plotted from the background trend (Simm et al, 2000).

4.3 Converting to angle gathers

In AVO analysis, offset gathers are converted to angle gathers to relate the data to Zoeppritz equation approximations. Angle gathers are obtained by converting offset gathers to incident angle gathers (Hampson-Russell Assistant). The angles of the VSP offset gathers were calculated using a derived simple trigonometric relationship that can be seen in Appendix B. Figure 4.2 shows the east walkaway angle gather.

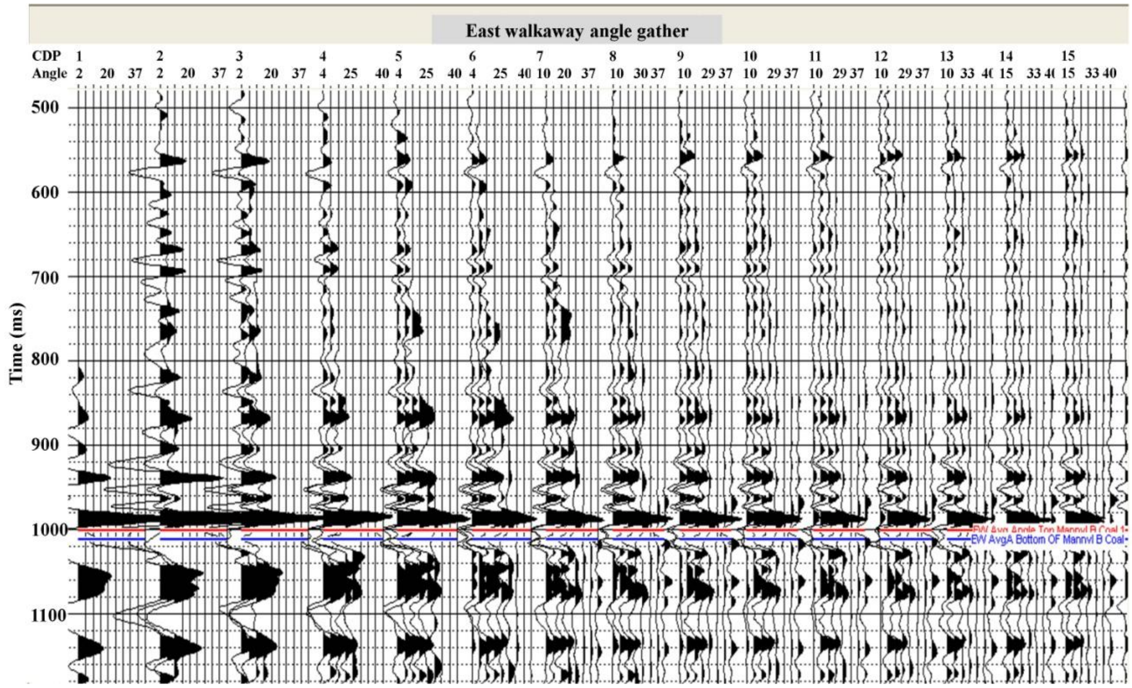

Figure 4.2: The east walkaway angle gather.

The seismic wave incidence angles of reflections for the four deepest receivers of each survey were calculated. These are the receivers closest to the Mannville B coals. These depths correspond to 1370.52 m, 1385.64 m, 1400.76 m and 1415.88 m. Ultimately an average of all these incident angles was calculated for each offset of each walkaway VSPCDP gather and these are shown in Tables 4.2 – 4.4. The angles are then input into the headers to convert the VSPCDP offset gathers to average angle gathers.

Table 4.2: East walkaway average angle calculation.

Walkaway	Offset (m)	Angle Of Incidence (Degrees)
East	51	2.01
	114	4.49
	249	9.73
	388	14.95
	529	20.01
	667	24.66
	807	29.05
	946	33.07
	1086	36.78
	1226	40.16

Table 4.3: Southeast walkaway average angle calculation.

Walkaway	Offset (m)	Angle Of Incidence (Degrees)
Southeast	51	2.01
	131	5.15
	270	10.53
	431	16.53
	551	20.77
	692	25.47
	830	29.74
	970	33.73
	1100	37.13
	1250	40.71
	1391	43.76

Table 4.4: South walkaway average angle calculation.

Walkaway	Offset (m)	Angle Of Incidence (Degrees)
South	51	2.01
	139	5.47
	240	9.38
	379	14.62
	518	19.63
	647	24.01
	802	28.90
	938	32.85
	1079	36.60
	1214	39.89
	1346	42.82

4.4 AVO Analysis

The P wave and density logs were used as input for the process. The AVO package requires an input S wave to the program. Since the S wave log does not exist, an S wave log is created using Castagna's equation of the form:

$$V_s = C1 \times V_p + C2$$

The variables C1 and C2 here are constants (Hampson-Russell Assistant). The C1 constant was set to 0.86190 and C2 was set to -1172 km/s. These values of C1 and C2 were assigned for the S wave velocity in order for it to be in accord with Castagna's mudrock line (Pelletier, 2008).

Next, the angle gathers are correlated to the logs and synthetics. First, three extracted statistical constant phase wavelets are generated for three angle ranges. A near range wavelet for 0-15 degrees, a mid range wavelet for 15-30 degrees and a far range wavelet for 30-45 degrees were generated to be used further into the AVO analysis. This grouping of angles is to relate to the three term Shuey approximation mentioned earlier in Section 4.2. Next, the P wave and density logs are used to calculate seismic impedance and be convolved with the extracted statistical wavelets. It should be noted that the first 3 CDPs of the south walkaway gathers and southeast walkaway gathers were excluded from the study because of their abnormal amplitudes. These abnormal amplitudes prevented proper stacking and correlation of amplitudes. Figure 4.3 shows the east walkaway angle gathers being correlated with the well logs and synthetic seismogram using the near range wavelet.

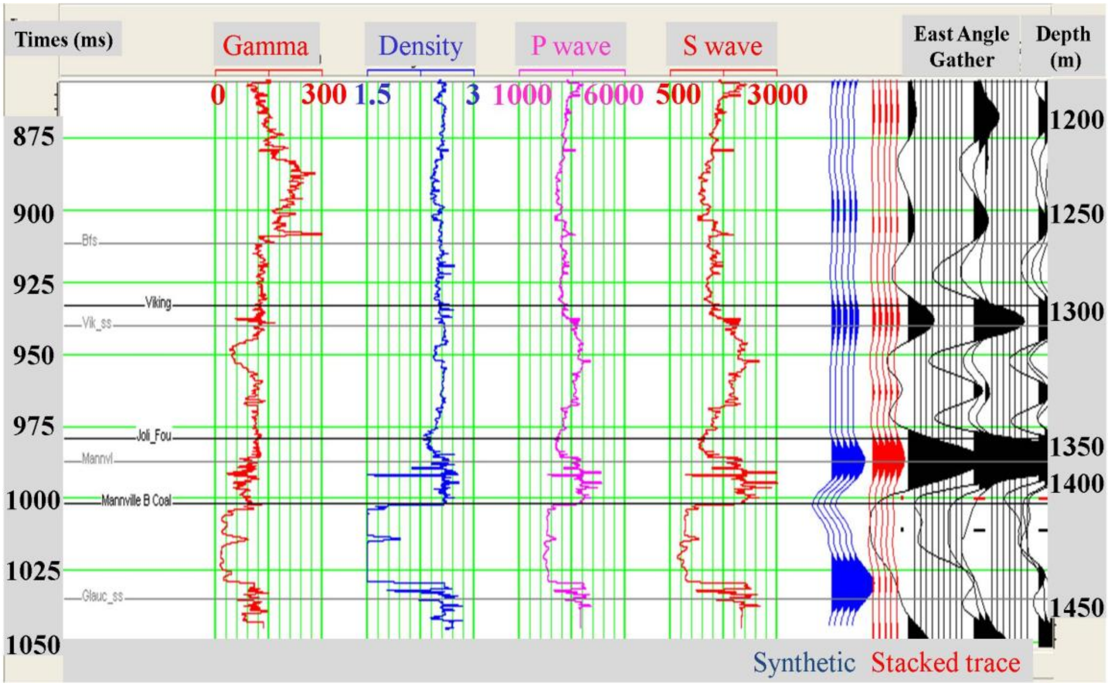

Figure 4.3: East walkaway angle gathers correlated with the well logs and synthetic. From left to right: Formation tops, gamma ray log (red), density log (blue), P wave velocity log (magenta), S wave velocity log (red), synthetic seismogram (blue), stacked trace (red), angle gather (black).

Figure 4.3 shows that the decrease in density, P wave velocity and S wave velocity at 1423 m TVD, at the top of the Mannville B coal zone. In addition, all the angular gathers had excellent correlation with the synthetic seismogram generated from the well log data. Figure 4.4 shows the extracted statistical wavelet that was used for the correlation and Figure 4.5 shows its corresponding amplitude spectrum.

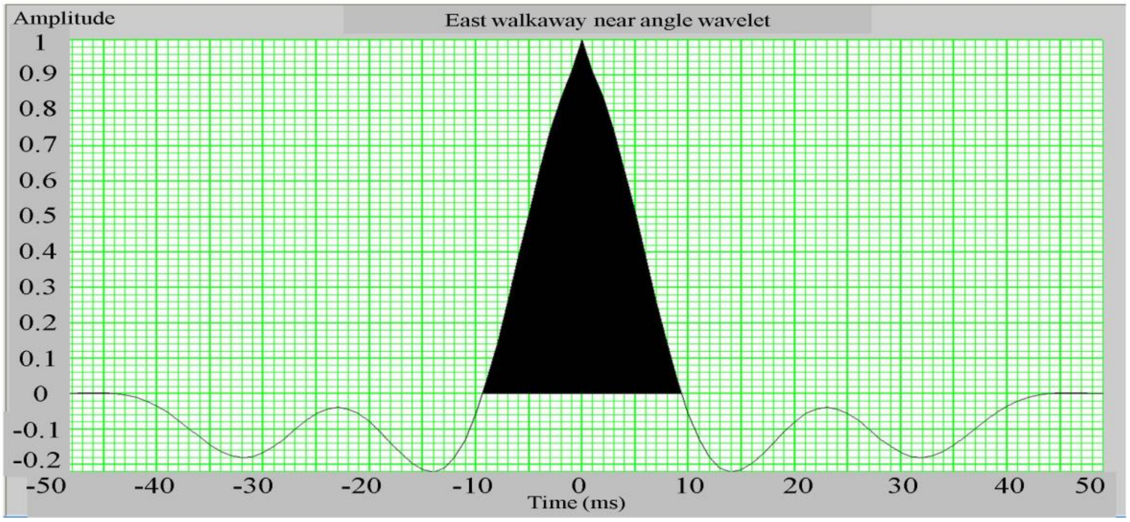

Figure 4.4: Extracted statistical constant phase near angle wavelet from the east walkaway angle gathers.

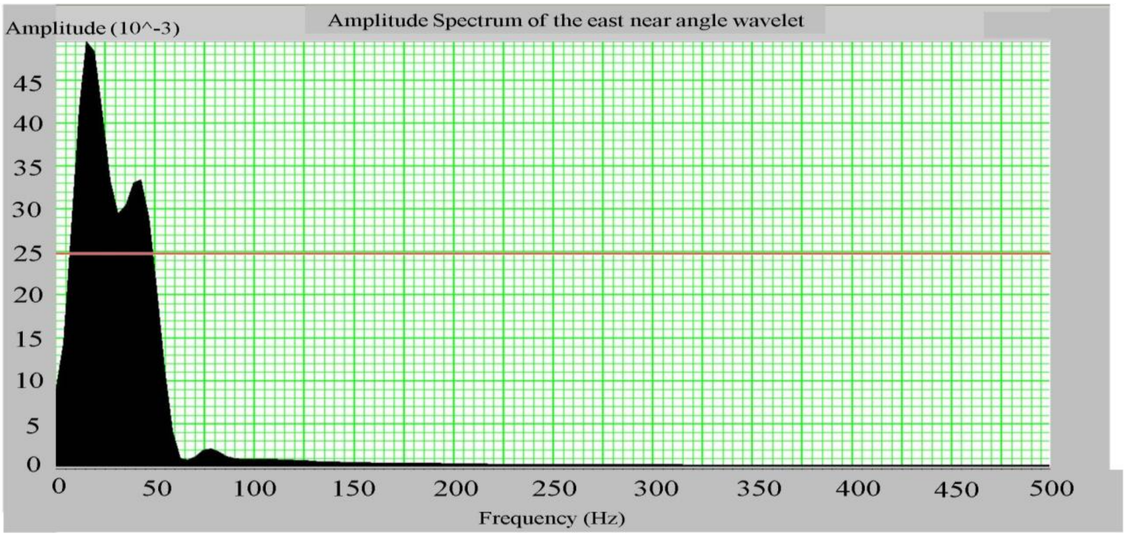

Figure 4.5: Amplitude spectrum of the extracted statistical constant phase near angel wavelet from the east walkaway angular gather. The wavelet has a dominant amplitude spectrum of 15 Hz.

After correlation, the top and bottom of the Mannville B coals are picked on all the angle gathers. The top of the Mannville B coal lies on a strong trough at depth 1423 m TVD corresponding to a time of 1000 ms. The bottom of the Mannville B zone is picked on the very next peak at 1434 m TVD corresponding to 1018 ms in time. Both horizons will be used further into this section when inversion will be performed on the data.

A window slice of the data is analyzed based on a 100 ms window around the top of the Mannville B coal zone. Figures 4.6- 4.8 show the results of crossplotting.

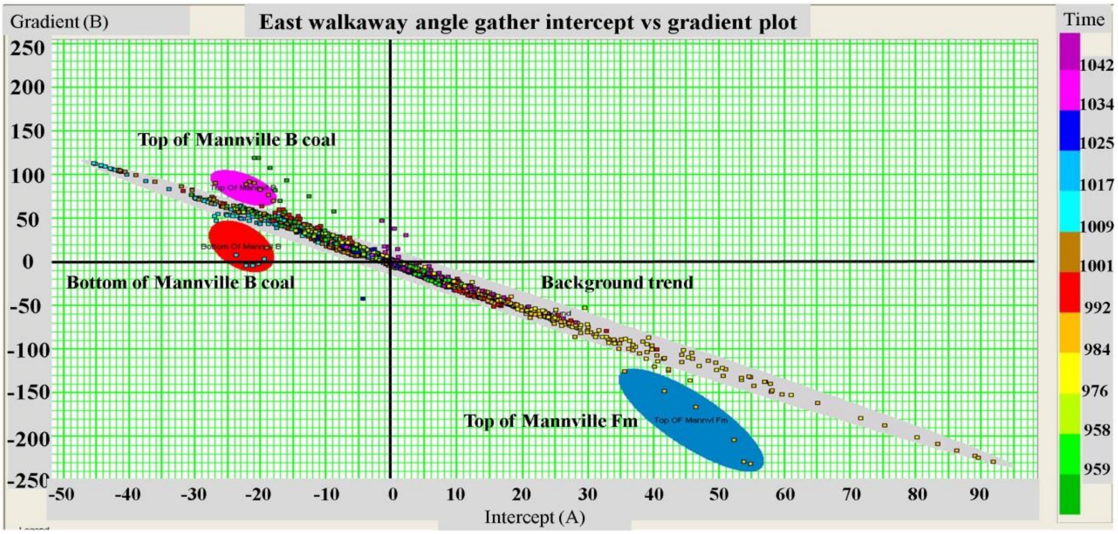

Figure 4.6: Intercept A versus gradient B plot of the east walkaway angle gather with four zones highlighted. The gray zone indicates the background trend, the blue zone indicating the top of the Mannville Fm trend, the magenta zone indicates the top of the Mannville B coal and the red zone indicates the bottom of the Mannville B coals.

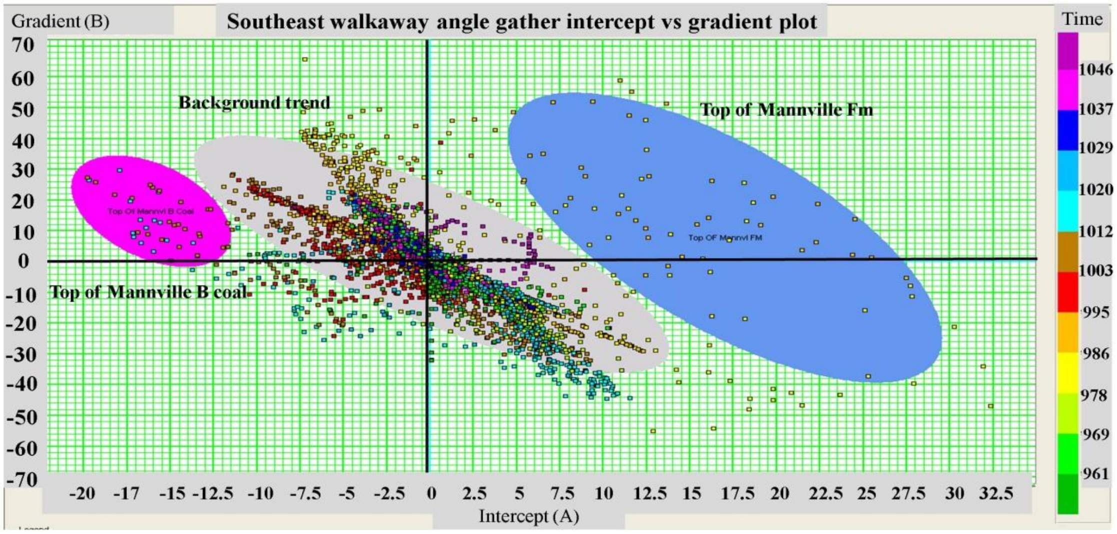

Figure 4.7: Intercept A versus gradient B plot of the southeast walkaway angle gathers with three zones highlighted. The gray zone indicates the background trend, the blue zone indicates the top of the Mannville Fm trend and the magenta zone indicates the top of the Mannville B coal.

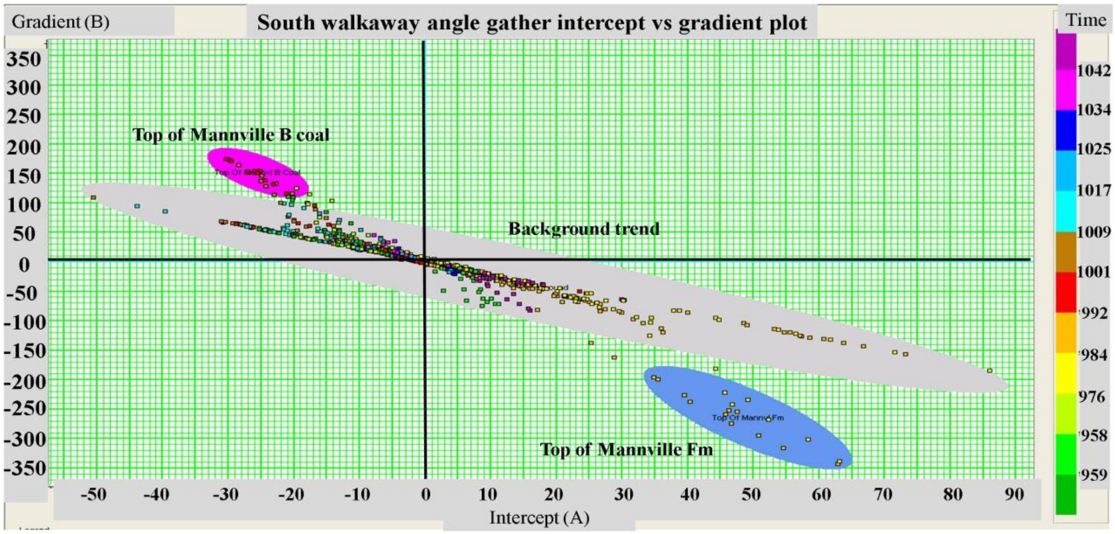

Figure 4.8: Intercept A versus gradient B plot of the south walkaway angle gather with three zones highlighted. The gray zone indicates the background trend, the blue zone indicates the top of the Mannville Fm trend and the magenta zone indicates the top of the Mannville B coal.

The analysis of the intercept A versus gradient B plots for the VSP data show different zones lying in different quadrants. The gray zone denotes the background trend of the data while the blue and magenta zones highlight the anomalies produced by the top of the Mannville Fm and the top of the Mannville B coals respectively. For the east walkaway, a red zone was added for the slight anomaly that the event from the base of the Mannville B coals produced.

For the east and south angle gathers, the top of the Mannville Fm is located in quadrant IV below the background trend. On the other hand, the top of the Mannville Fm is located between quadrant I and IV for the southeast walkaway over the trend.

The Mannville B coal is located in quadrant II for all three angle gathers. However, for the east and south angle gathers the Mannville B coal anomaly plots over the background trend, indicating no free gas in the coals. For the southeast angle gather, the top of the Mannville B coal plots below the trend. This anomaly in the southeast angle gather shows an indication of gas bearing coals. The top of the Mannville B coal for all three angle gathers is consistent with the expectation that it has a strong negative AVO intercept. The east angle gather showed a slight anomaly at the bottom of the Mannville B coal but was very slight.

4.5 Inversion

Generally, inversion is performed to yield petrophysical attributes, such as P and S impedances, LambdaRho ($\lambda\rho$) and MuRho ($\mu\rho$) that are in turn entered into crossplots that better aid in distinguishing lithology and fluid content. The goal is to generate $\lambda\rho$ versus $\mu\rho$ crossplots for each of the walkaway angle gathers.

The inversion process starts by using the well logs as input to generate an initial model. In the inversion process, it is desirable to choose more than one wavelet for a range of angles similar to the near, mid and far angle wavelets discussed earlier. This is because frequency-dependant absorption and NMO tuning could cause the far offset angle gathers to be of lower frequencies (Hampson-Russell).

The initial model is based on the P wave, calculated Castagna S wave and density log. The initial model is built with a high frequency limit of 10 to 15 Hz. The frequency is limited so that the low frequencies that are missing from the seismic data are provided from this model. Figure 4.9 shows the generated initial model for the southeast walkaway angular gathers.

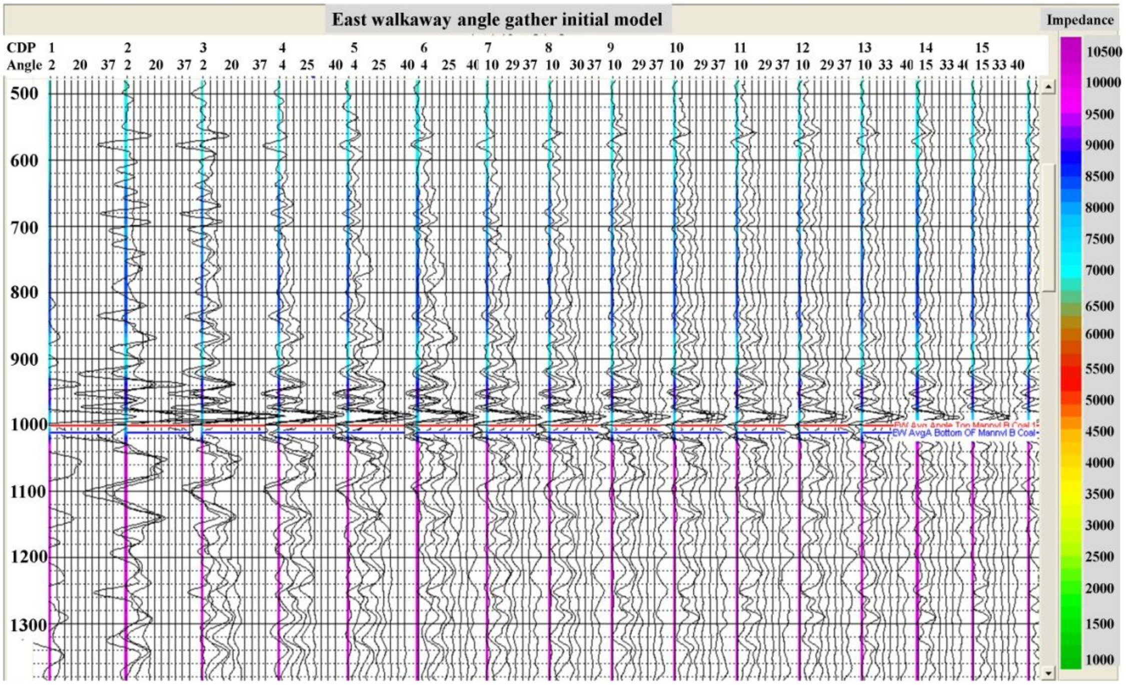

Figure 4.9: The initial model created from well logs to match angular gathers from the east walkaway angle gathers. The small colored strip on the side of the gathers represents the P wave impedance.

Figure 4.9 illustrates the initial model created that will be iterated to match the east walkaway angle gathers with a small thin column representing the P wave impedance beside it in color. Figures 4.10 and 4.11 show the full P and S wave initial impedance models, respectively.

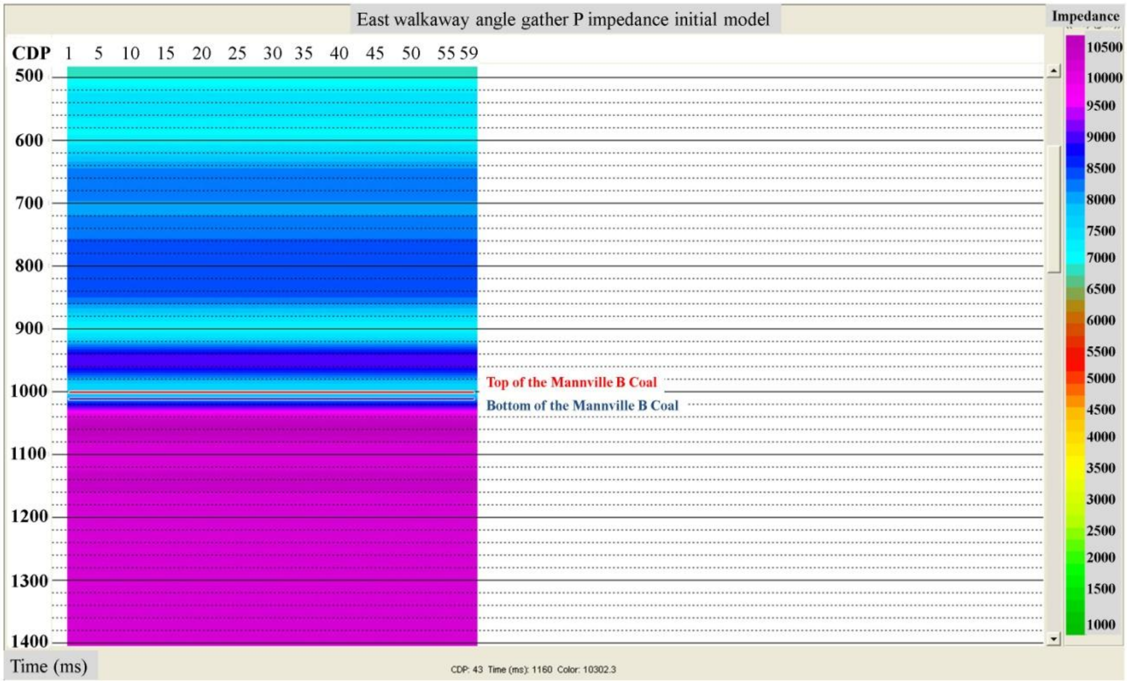

Figure 4.10: The initial model created to match the east walkaway VSP data. The colors represent the P wave impedance.

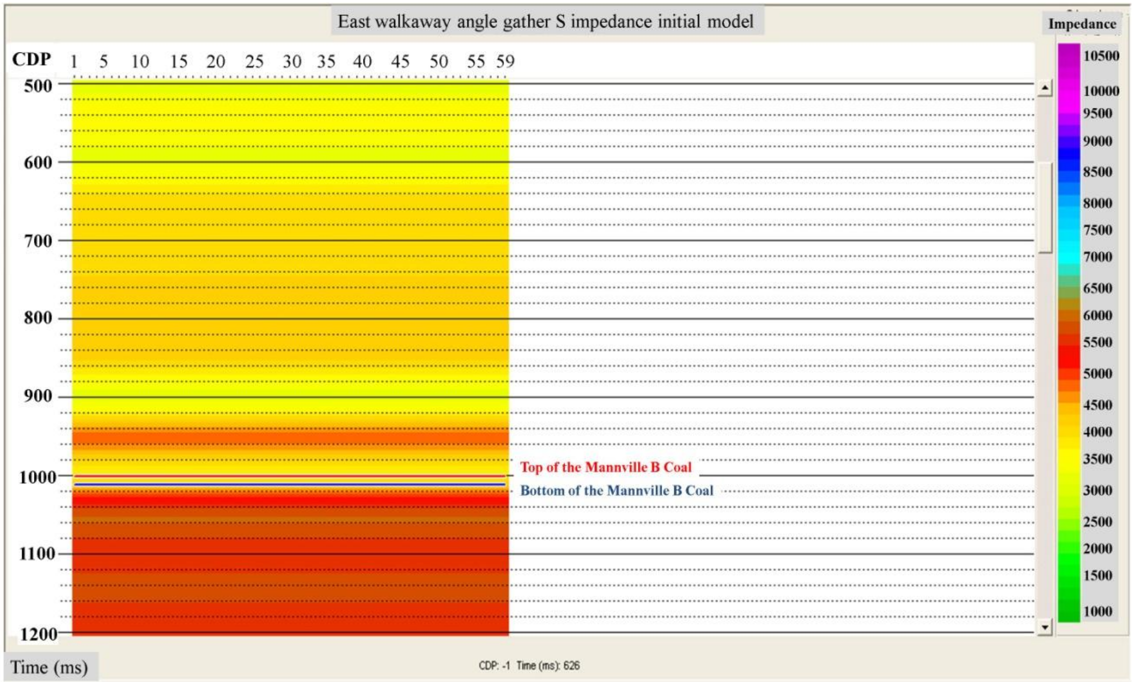

Figure 4.11: The initial model created to match the east walkaway VSP data. The colors represent the S wave impedance.

Now that the initial models for all three VSP angular data has been created, the modeling parameters have to be determined for the inversion. The angles for all wavelets are specified as 7.5, 22.5 and 35 degrees for the near, mid and far angle wavelets, respectively. In addition, the generated P and S impedances from the model are used for the analysis along with the density log. The inversion coefficients are obtained using linear regression. The following relationships are assumed (Hampson-Russell Assistant):

$$\ln(Z_S) = k\, ln(Z_P) + k_c + \Delta L_S$$

$$\ln(\rho) = m\, ln(Z_P) + m_c + \Delta L_D$$

Where

Zp = P wave impedance.

Zs = S wave impedance.

ρ = density.

k, m, kc and mc = constant coefficients determined by inversion analysis shown later in this section.

ΔL_S and ΔL_D = the effect when the fluid contained is not water. Otherwise will be zero. These are the best fit lines through the plotted ln(Zp) versus ln(Zs) and the ln(Zp) versus ln(ρ) in the inversion coefficient analysis shown later.

The assumption is that there is a linear relationship between P wave and S wave impedance and density. The coefficients k, kc, m, mc are analyzed from well logs data and regression process. Figure 4.12 shows the ln(Zp) versus ln(Zs) and the ln(Zp) versus ln(ρ) plots in which the coefficients are estimated for the southeast walkaway angle gathers. The inversion process was iterated 50 times, each time updating the P and S wave impedances. The density is not iterated in the inversion process since it is hard to estimate it for angles less than 45 degrees. Two global scalars are estimated making the RMS amplitude of the real data equal to those of the synthetic data. The Vs/Vp ratio is kept to 0.5.

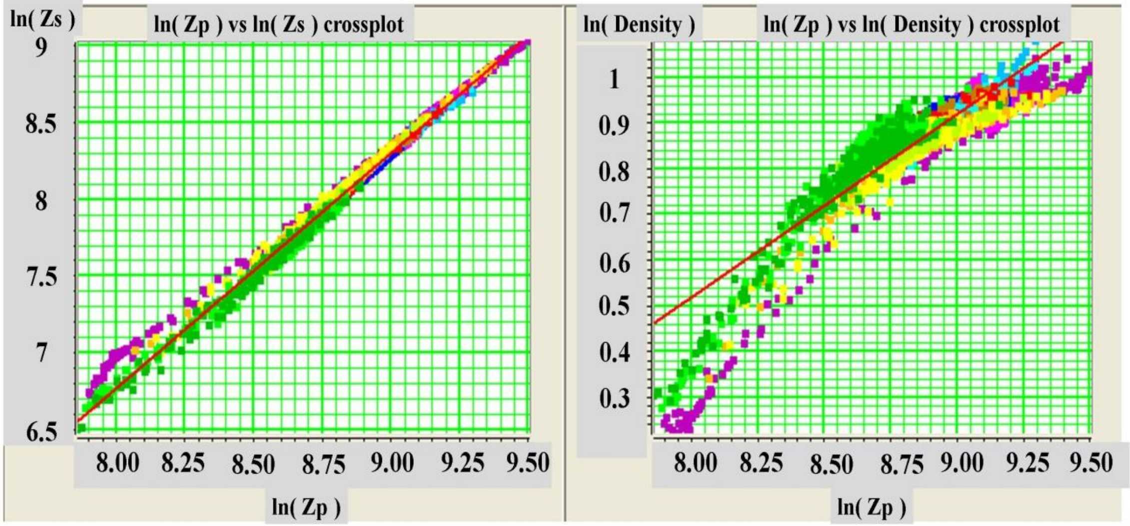

Figure 4.12: Plots of ln(Zp) versus ln(Zs) and ln(density) for inversion coefficients using well log data and linear regression for the east walkaway angular data. Notice the red line in the plots is used for linear regression and can be altered manually.

After the inversion analysis, it can be checked how the inversion performed. Figure 4.13 shows the inversion analysis result compared to the real east walkaway angle gathers.

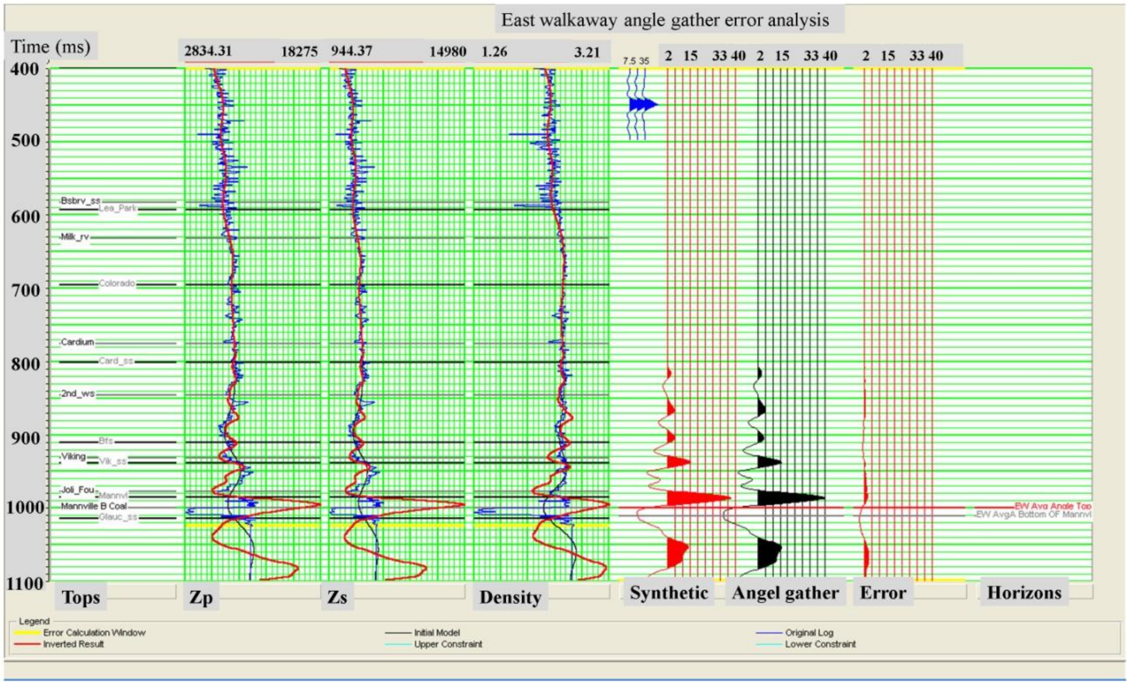

Figure 4.13: The result of the inversion analysis performed on the east walkaway angular gather. The logs are in blue with the superimposed red curves as a result of the inversion analysis. The seismic data from left to right: inverted synthetic in red, actual angular data in black, the error between the real data and inverted data.

The inversion analysis in Figure 4.13 indicates very little error between the synthetic data in red against the angle gathers in black. The error between the model synthetic and the angular seismic data is shown in the last track on the right. Through the analysis of all three angular gathers, most of the error existed in the near offset angle gathers. The modeled logs mimic the well logs very well above the Mannville Fm but has some error at the top of the Mannville Fm.

After analysis, the inversion process can be performed on the volume of data and the inverted P and S impedances can be calculated over the range of the data. Figure 4.14 shows the difference between the east walkaway angular gathers and the synthetic modeled data. This tool shows where most of the residual error is.

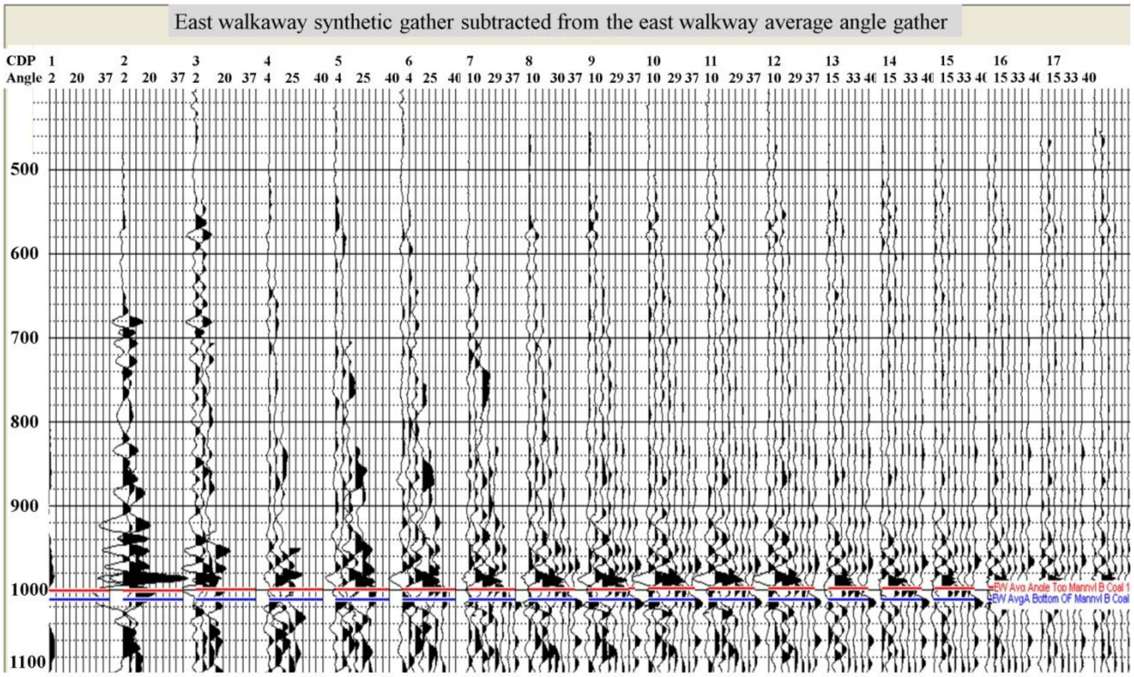

Figure 4.14: Residual seismic error from subtracting the synthetic inverted data from the original east walkaway angular gathers.

In Figure 4.14, it is apparent that most of the residual error in the case of the east walkaway angular gather is around the top of the Mannville Fm. However, no consistent error is noticeable around the Mannville B coals, which is our target zone. Eventually the errors in the near angle gathers fade with increasing angular gathers.

Figures 4.15 and Figure 4.16 show the inverted S and P wave impedances.

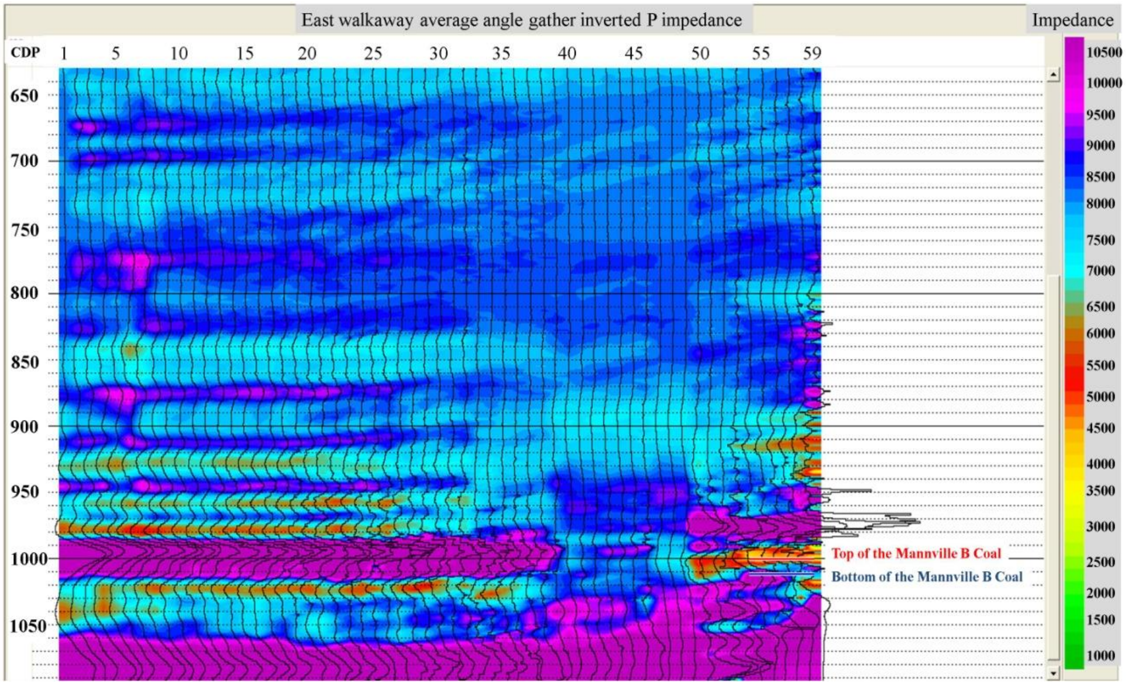

Figure 4.15: Inverted P wave impedance from the east walkaway angular gathers.

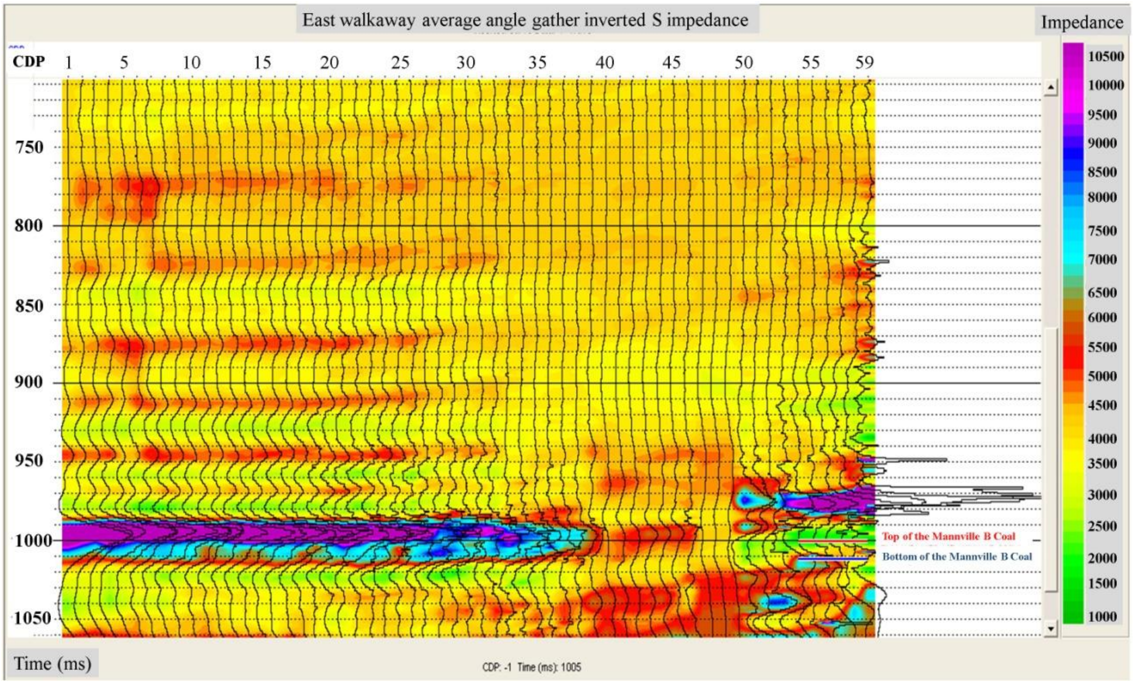

Figure 4.16: Inverted S wave impedance from the east walkaway angular gathers.

In the P and S wave impedance plots there are strong impedances just over 1000 ms representing the top of the Mannville Fm. No real impedance anomalies were discovered around the top of the Mannville B coals since it was masked by the strong impedance of the Mannville Fm.

4.6 Lame parameters

The Lame parameters are sometimes utilized as an aid to identify pore fluid or lithologies discrimination (Dumitrescu and Lines, 2007). Lambda and Mu are directly related to rock properties and can be related to P wave and S wave velocities (Lines and Newrick, 2004). A further crossplot involved in lithology distinction is the $\lambda\rho$ versus $\mu\rho$ crossplot. This crossplot gives a significant indicator of lithology like sands, shale and carbonates and contributes to gas effect detection. The decrease in Lambda values is sensitive to fluid effect when using the $\lambda\rho$ versus $\mu\rho$ crossplot (Goodway, 2001).

The $\lambda\rho$ and $\mu\rho$ crossplot is desired since it tends to isolate different lithology and gas bearing rock types into different clusters. The advantage being that most conventional crossplots such as Vp versus Vs or P and S wave impedances share the rigidity parameter where as the $\lambda\rho$ and $\mu\rho$ parameters are more orthogonal (Goodway, 2001). A general guide for interpretation of the $\lambda\rho$ versus $\mu\rho$ crossplot is taken from (Goodway, 2001) in Figure 4.17. Another guide that includes where the coals should plot is in Figure 4.18.

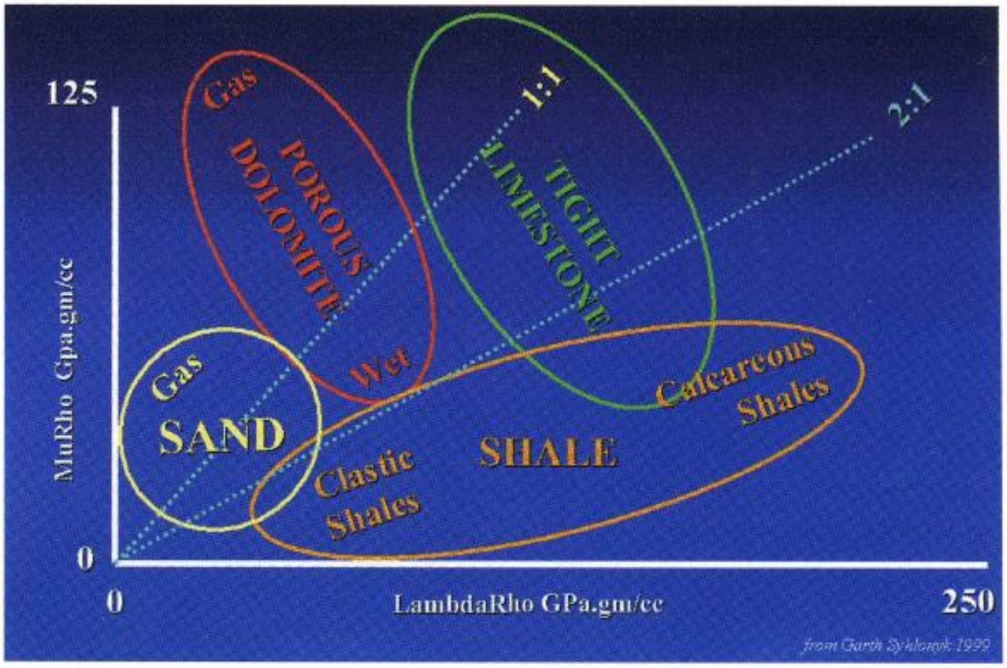

Figure 4.17: A general interpretation of the LambdaRho versus MuRho crossplot (from Goodway, 2001).

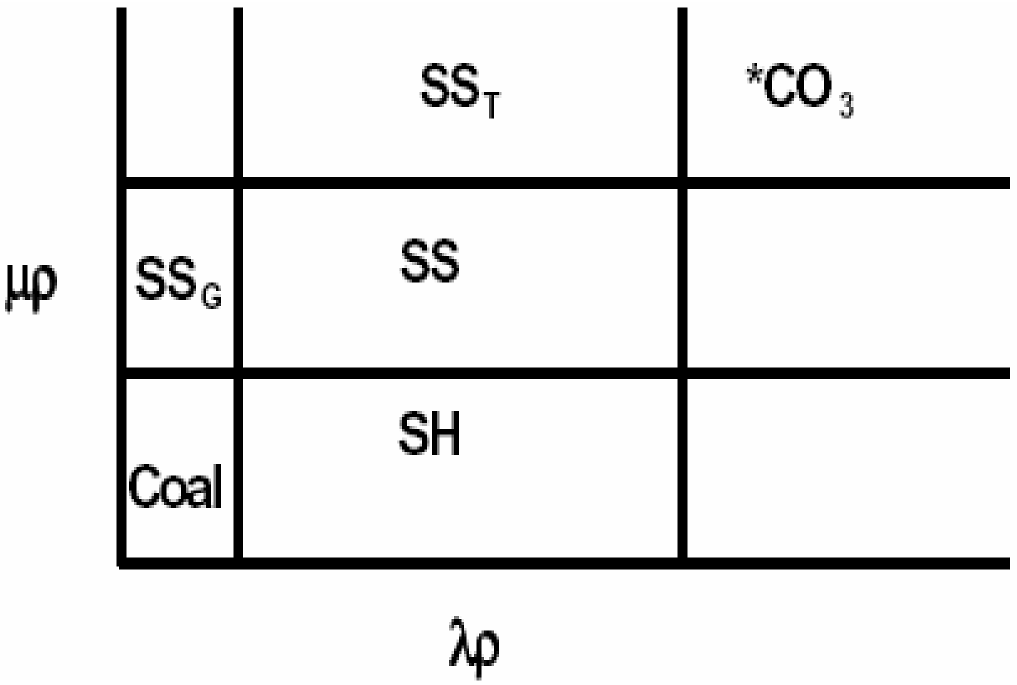

Figure 4.18: A general interpretation of the LambdaRho versus MuRho crossplot (from Anderson and Gray, 2001).

In Figure 4.18, the SS_G is gas saturated sandstone, SS is sandstone, SS_T is cemented sandstone, and CO_3 is carbonates. Notice that the coals plot in the lower left corner near the origin of the plot. This plot location is consistent for coals in both (Goodway, 2001) and (Anderson and Gray, 2001).

Figures 4.19 to 4.21 show the Lambda Rho versus Mu Rho plots for the three angle gathers representing the walkaway VSP data.

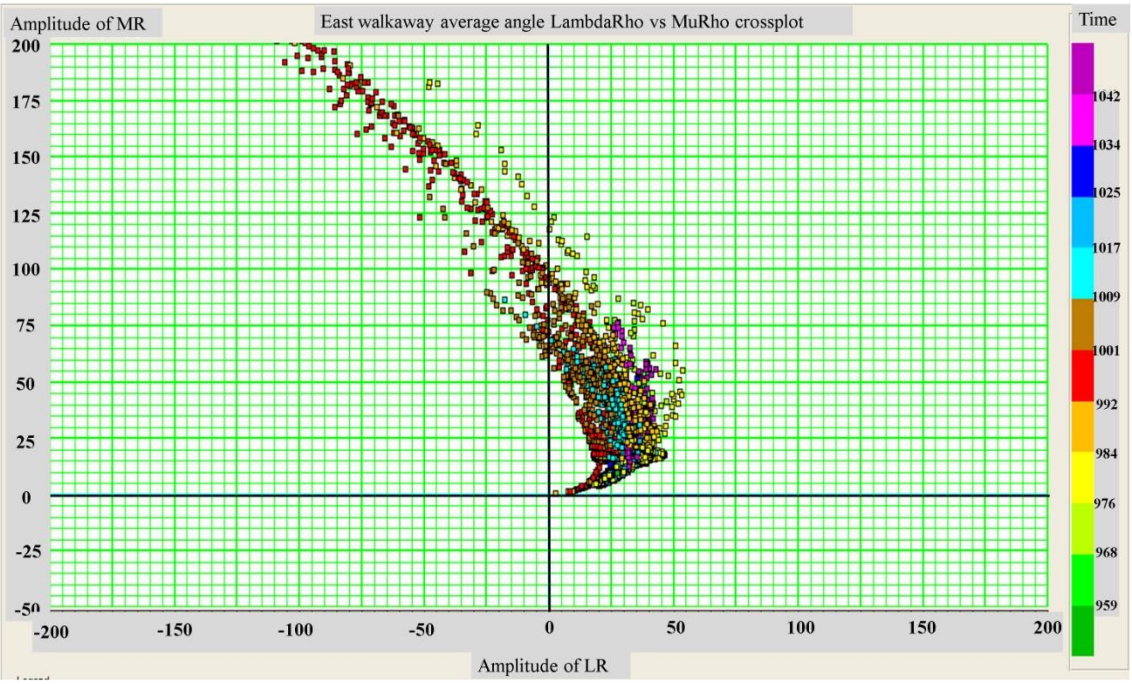

Figure 4.19: LambdaRho vs MuRho plot taken from the east walkaway angular gathers centered around the top of the Mannville B Coal.

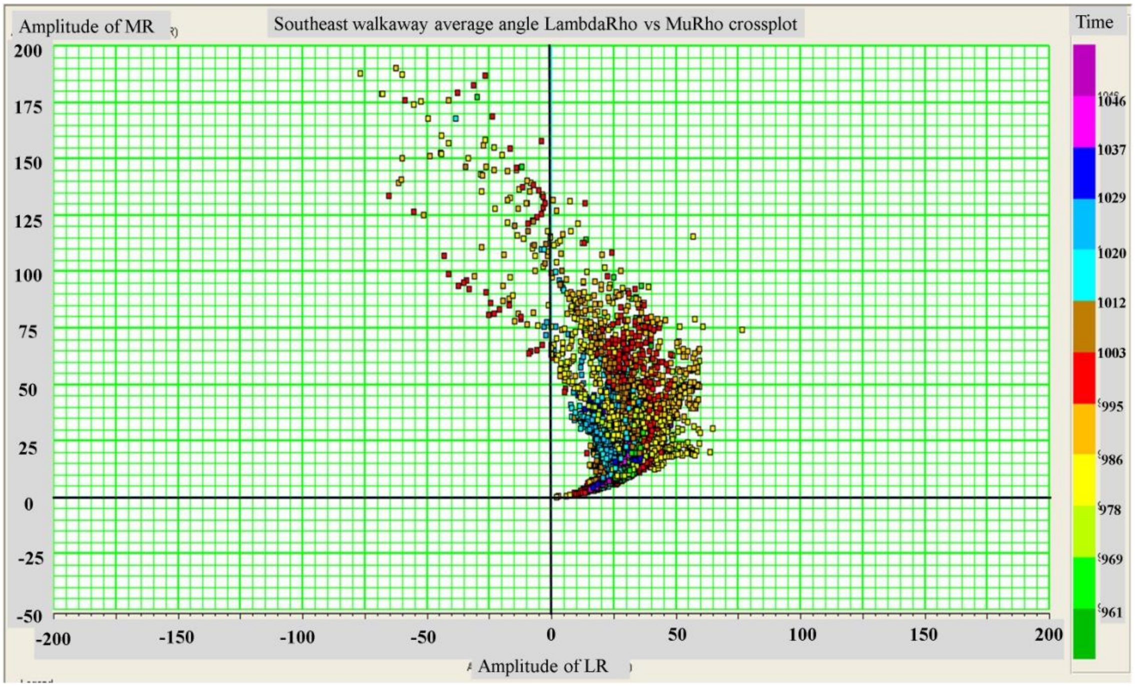

Figure 4.20: LambdaRho vs MuRho plot taken from the southeast walkaway angular gathers centered around the top of the Mannville B Coal.

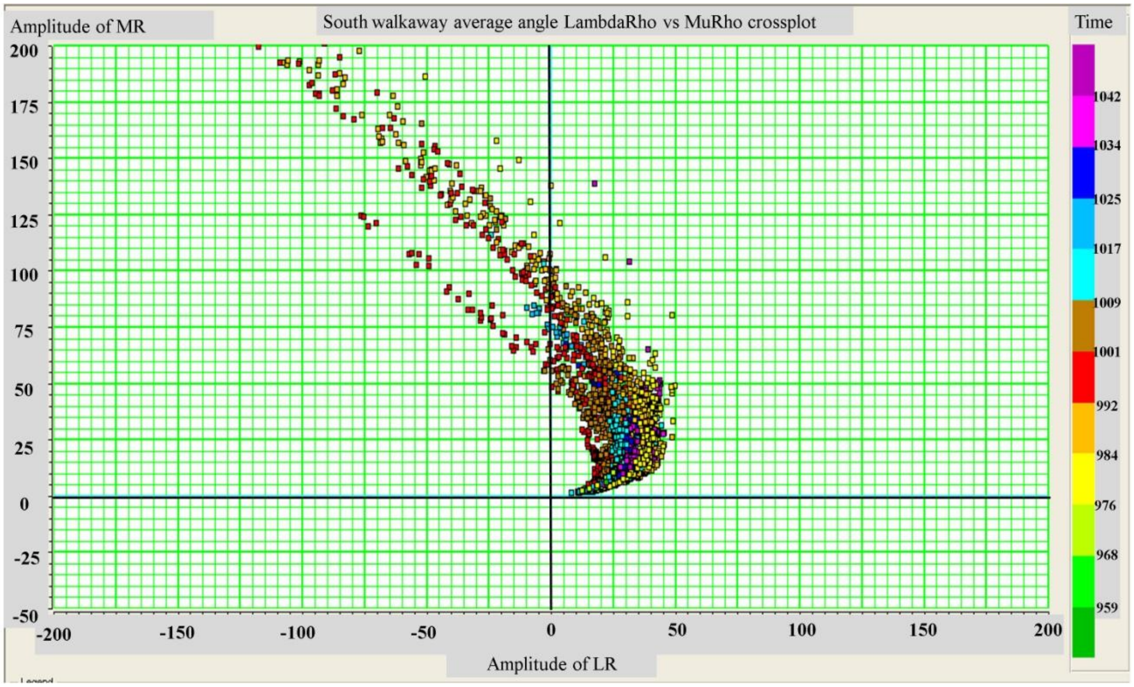

Figure 4.21: LambdaRho vs MuRho plot taken from the south walkaway angular gathers centered around the top of the Mannville B Coal.

In Figures 4.19 – 4.21, the Lambda Rho versus Mu Rho plots indicate that the coals plot as expected in the lower left corner of the Lambda Rho versus Mu Rho near the origin. The coals are indicated in light blue and dark brown colors and are consistent with both (Anderson and Gray, 2001) and (Goodway, 2001). However, there is not clear separation between the coals and the other lithology indicating that probably the anomaly does not exist and therefore little or no free gas is in the Mannville B coals.

From Figures 4.19 – 4.21, it is noticeable that there are inconsistent negative Lambda Rho values appear at the top of the Mannville Fm. I believe that this might have to do with the abnormal impedances of the top of the Mannville Fm that the inversions performed did have some error in modeling. This could have to do with the near offset time variant rotations of the southeast and south walkaway lines in which some difficulty was found. Note however that our target zone of the Mannville B coals plotted the coals in the right place in all of the walkaway angle gathers near the origin of the Lambda Rho versus Mu Rho crossplot. To investigate this further, I have calculated Lambda Rho values from the inverted data using P and S impedances. The results of these calculations are given in Tables 4.5 – 4.7.

Table 4.5: Calculated Lambda Rho values form the impedances of the inverted P and S impedances of the east walkaway angle gathers.

Walkaway	P Impedance (Squared)	S Impedance (Squared)	Lambda Rho
East CDP 2	274465489	161366209	-48266929
East CDP 20	292136464	178944129	-65751794
East CDP 30	199515625	103938025	-8360425
East CDP 40	65011969	19820304	25371361

Table 4.6: Calculated Lambda Rho values form the impedances of the inverted P and S impedances of the southeast walkaway angle gathers.

Walkaway	P Impedance (Squared)	S Impedance (Squared)	Lambda Rho
Southeast CDP 2	331240000	189420169	-47600338
Southeast CDP 20	137288089	44582329	48123431
Southeast CDP 30	75342400	18757561	37827278
Southeast CDP 40	40106889	6140484	27825921

Table 4.7: Calculated Lambda Rho values form the impedances of the inverted P and S impedances of the south walkaway angle gathers.

Walkaway	P Impedance (Squared)	S Impedance (Squared)	Lambda Rho
South CDP 2	258984649	153512100	-48039551
South CDP 20	163149529	80748196	1653137
South CDP 30	114918400	42133081	30652238
South CDP 40	121616784	57365476	6885832

From Tables 4.5 – 4.7, show the Lambda Rho values in the inverted model at the top of the Mannville Fm. This has to do with the errors in inverting the top of the Mannville Fm. In some instances, the S wave impedances is larger than the P wave impedances resulting in a negative Lambda Rho values. This is especially the case in the near offsets where the error is larger.

Goodway (2001) gave an example of negative Lambda Rho values in an example of a shale. The author explains that because of the various definitions of the parameters and moduli and ratios, this generates some inconsistencies for sedimentary rocks. For instance, Poisson's ratio is negative for negative lambdas until $-\lambda = \mu$ and then it goes to positive. In addition, the bulk modulus is positive for negative Lambdas until $-\lambda = (2/3)\mu$ and afterwards it is negative. Goodway explains that the nonlinear Poisson ratio, bulk modulus and Lame parameters all contribute to these negative Lambda values. The example that Goodway gives has a negative Lambda and Poisson ratio with positive bulk modulus. This example suggests an impossible material where the material is compressed by stress longitudinally and is laterally contracts in strain. Goodway suggests that Lambda should be more reliable parameter over moduli since it is the true real incompressibility measure and the other moduli is due to mathematical inconsistencies. Negative Lambda values are also associated with abnormal low Vp sonic values in shales (Goodway, 2001).

4.7 Discussion

After crossplotting the intercept A versus gradient B for all three walkaway angle gathers, the southeast angle gathers is the only crossplot indicating the possible existence of gas in the Mannville B coals. The southeast crossplot plotted the top of the Mannville B coal in quadrant II under the background trend. The east and south angle gather crossplot plotted the top of the Mannville B coal in the quadrant II over the background trend that basically indicates no or little free gas in the coals. All three walkaway angle gathers indicated a strong negative AVO intercept.

In addition, plotting all three walkaway angle gathers in the Lambda Rho versus Mu Rho, all the crossplots plotted the Mannville B coals consistently near the bottom left corner of the crossplot which is consistent with (Goodway, 2001) and (Anderson and Gray, 2001). However, the Mannvile B coal data plotted with no cluster separation from the background data. This indicates no or little free gas in all three walkaway angle gathers.

Negative Lambda Rho values in the top of the Mannville Fm have to do with the inversion result that had some errors with the angle gathers. However, the Mannville B coals were not found to significant errors since the data plotted in its proper expected place in the Lambda Rho versus Mu Rho plots.

CHAPTER 5: CONCLUSIONS

In this thesis, a zero offset VSP was processed to corridor stacks, and three walkaway VSPs were processed to CDP and CCP maps for P-P and P-SV reflections, respectively. The zero offset VSP proved to exhibit no significant multiples and an excellent tie to synthetic seismogram from a well log was obtained. The walkaway VSP had a shot static problem and therefore a suggestion to have an overlap of at least one receiver is suggested to avoid this problem in the future. In all three walkaway VSPs, the P wave reflection decrease in amplitude with offset while the S wave reflection amplitude increased with offset, as expected from theory.

After crossplotting the intercept A versus gradient B for all three walkaway angle gathers, the southeast angle gather is the only crossplot that indicated that the coals could contain free gas. The southeast crossplot plotted the top of the Mannville B coals in quadrant II below the background trend. The east and south gathers plotted the top of the Mannville B coal in the quadrant II above the background trend that indicates low free gas content. All three walkaway angle gathers indicated a strong negative AVO intercept.

In addition, all three walkaway angle gathers in the Lambda Rho versus Mu Rho plots, placed the Mannville B coals consistently near the origin of the crossplot which is consistent with the results of (Goodway, 2001) and (Anderson and Gray, 2001). However, the Mannville B coal data plotted with no cluster separation from the background data. This indicates low free gas content in all three walkaway angle gathers.

Negative Lambda Rho values in the top of the Mannville Fm have to do with errors in the inversion result due to noise in the seismic angle gathers.

References

Alduhailan, M., 2008, Field mapping and seismic analysis of fractures, University of Calgary, Ms.c thesis.

Anderson and Gray, 2001, Using LMR for dual attribute lithology identification, SEG expanded abstracts.

Ayers Jr., W.B., 2002, Coalbed gas systems, resources, and production and a review of contrasting cases from the San Juan and Powder River basins, AAPG Bulletin, v. 86, no. 11, pp. 1853-1890.

Bell., J.S., Bachu, S., 2003, In situ stress magnitude and orientation estimates for Cretaceous coal-bearing strata beneath the plains area of central and southern Alberta, Bulletin of Canadian Petroleum Geology, **51**, No. 1, pages 1-28.

Campbell A., Fryer, A., Wakeman, S., 2005, Vertical seismic profiles – more than just a corridor stack, The Leading Edge, July, P. 694 – 697.

Castagna, J.P., Swan, H.W., 1997, Principles of AVO crossplotting, The Leading Edge, April.

Castagna, J.P., Swan, H.W., Forster., D.J., 1998, Framework for AVO gradient and intercept interpretation, Geophysics, Society of Exploration Geophysicists, 63, 948- 956.

Coulombe, C.A., 1993, Amplitude-Versus-Offset analysis using vertical seismic profiling and well log data, Master's Thesis, Department of Geology and Geophysics, The University of Calgary.

Dillon, P.B., Thomson, R.C., 1984, Offset source VSP surveys and their image reconstruction, Geophysical Prospecting 32, P. 790-811.

Dix, C.H., 1955, Seismic velocities from surface measurements, Geophysics, Vol. XX NO.1 January, P. 68-86.

Dumitrescu, C.C., Lines, L.R., 2007, Application of multicomponent data in lithology and fluid discrimination, CSPG CSEG Convention, p 465-468.

Goodway, B., 2001, AVO and Lame constants for rock parameterization and fluid detection, CSEG Recorder, June, p. 39-60.

Hardage, B.A., 1983, Vertical seismic profiling Part A: Principles, volume 14A, Geophysical Press, London-Amsterdam.

Hartse, H.E., 1990, Understanding offset VSP, GEOPHYSICS: The Leading Edge of Exploration, April, P. 30-36.

Hinds, R.C., Anderson, N.L., Kuzmiski, R.D., 1999, VSP Interpretive Processing: Theory and Practice, Society of Exploration Geophysicists.

Hinds, R.C., Kuzmiski, R.D., 2009, Borehole Geophysics: Theory and Practice, SEG Continuing Education Course Notes.

Kalinski, M.E., 2007, Effect of vibroseis arrays on ground vibrations: a numerical study, Journal of Environmental and Engineering Geophysics, P. 281-287.

Lines, L.R., Newrick., R.T., 2004, Fundamentals of Geophysical Interpretation, geophysical monograph series, number 13, society of exploration geophysicists (SEG).

Li, Y., Downton, J., Xu, Y., 2007, Practical aspects of AVO modeling, The Leading Edge, March, p. 295-311.

Margrave, G.F., 2008, Methods of seismic data processing, Geophysics 557 course lecture notes, the department of geology and geophysics, University of Calgary.

Parker, R., Jones, M., 2008, Rig-source VSP/Sonic Calibration/Synthetics/Walkaway VSP Processing Report, Shlumberger, pages 5-14.

Pelletier, H., 2008, AVO Crossplotting Revisited: A Practitioner’s Perspective, CSEG Recorder, December 2008 issue, p. 40-46.

Richardson, S.E., 2003, Multicomponent seismic applications in coalbed methane development, Red Deer, Alberta, University of Calgary Ms.c thesis.

Ross, C.P., 2000, Effective AVO crossplot modeling: A tutorial, Geophysics, vol. 65, No. 3, May-June, P.700-711.

Sheriff, R.E., 1997, Encyclopedic dictionary of exploration geophysics, third edition, Geophysical references series, Society of Exploration Geophysicist.

Shuey, R.T., 1985, A simplification of the Zoeppritz equations, Geophysics Vol. 50, NO. 4, April, P. 609-614.

Simm, R., White, R., Uden, R., 2000, The anatomy of AVO crossplots, The Leading Edge, February 2000.

Schlumberger Oilfield glossary, http://www.glossary.oilfield.slb.com/Display.cfm?Term=kelly%20bushing

Stewart, R.R., 1991, Short note Rapid map and inversion of P-SV waves, Geophysics, VOL. 56, NO. 6, June, P. 859-862.

Stewart., R.R., 2001, VSP: An In Depth Seismic Understanding, Department of Geology and Geophysics, University of Calgary, CSEG Recorder, **26**, No. 7.

Stewart, R.R., Disiena, J.P., 1989, The values of VSP in interpretation, Seismic Interpretation 20, The Leading Edge of Exploration, December.

Wyatt, K.D., Wyatt, S.B., 1984, Determining subsurface structure using the vertical seismic profile, in Tokzos, M.N., and Stewart, R.R., Vertical Seismic Profiling Part B: Advance concepts, Geophysical Press, P. 148-177.

Encana Corp.

Hampson-Russell Assistant.

VISTA Help and Tutorials

APPENDIX A: EAST WALKAWAY VSP RAW THREE COMPONENT DATA

In this appendix, the raw X, Y and Z components of the east walkaway VSP are shown.

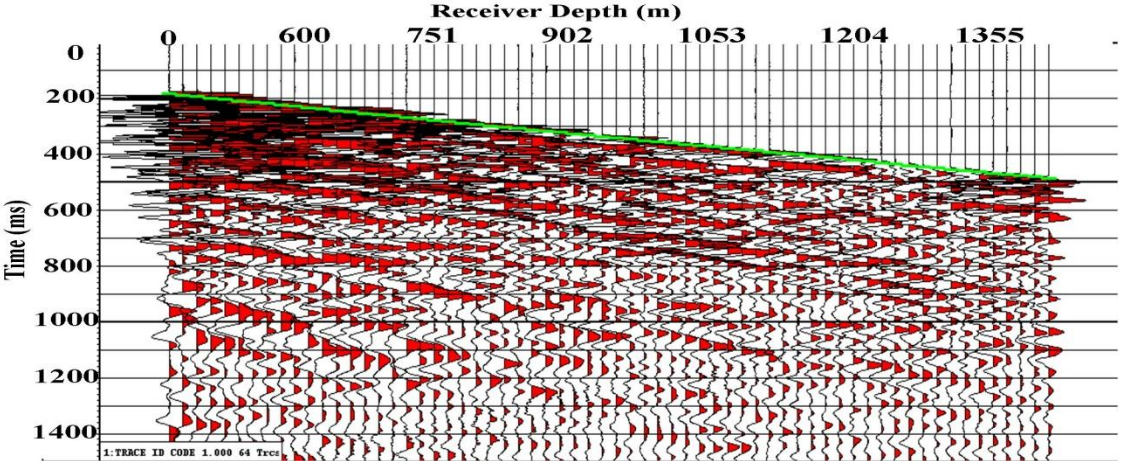

Figure A.1: East walkaway offset -51 X component with first break.

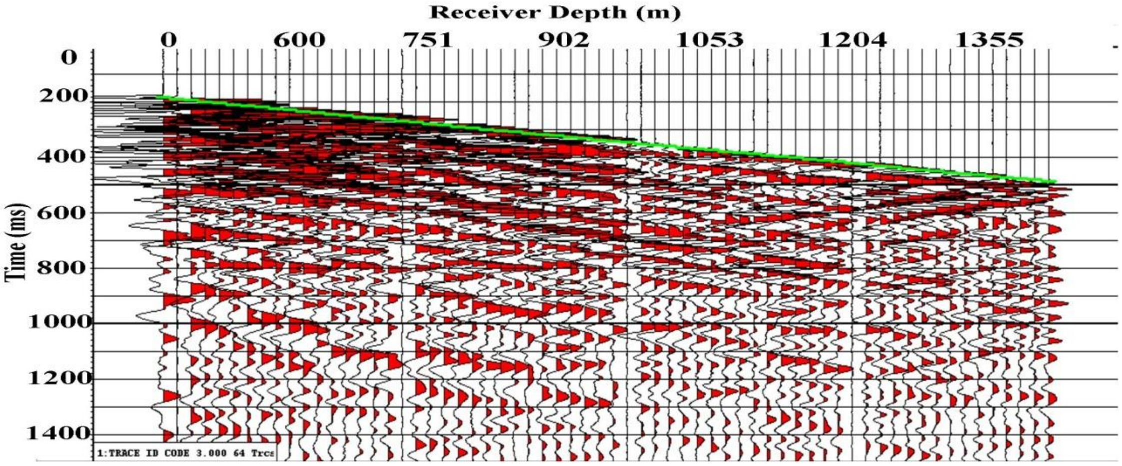

Figure A.2: East walkaway offset -51 Y component with first break.

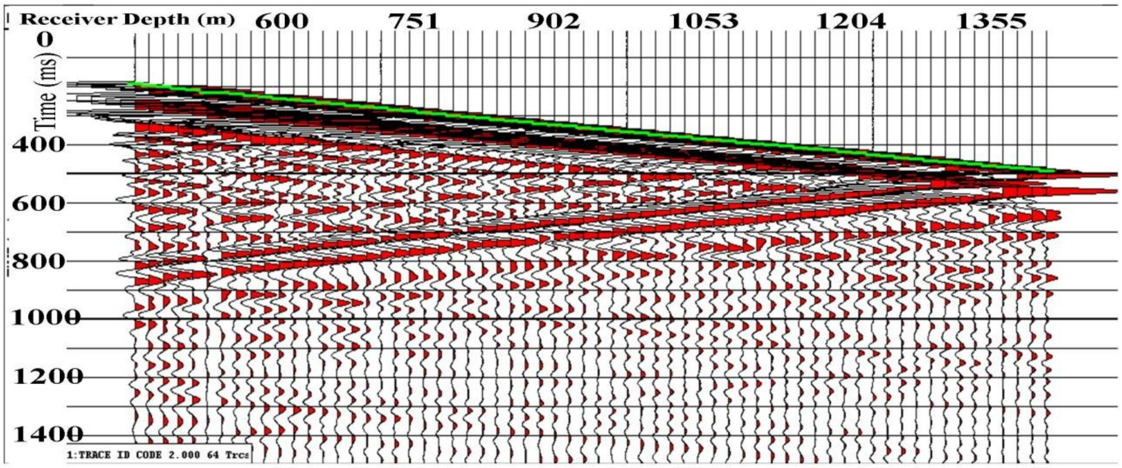

Figure A.3: East walkaway offset -51 Z component with first break.

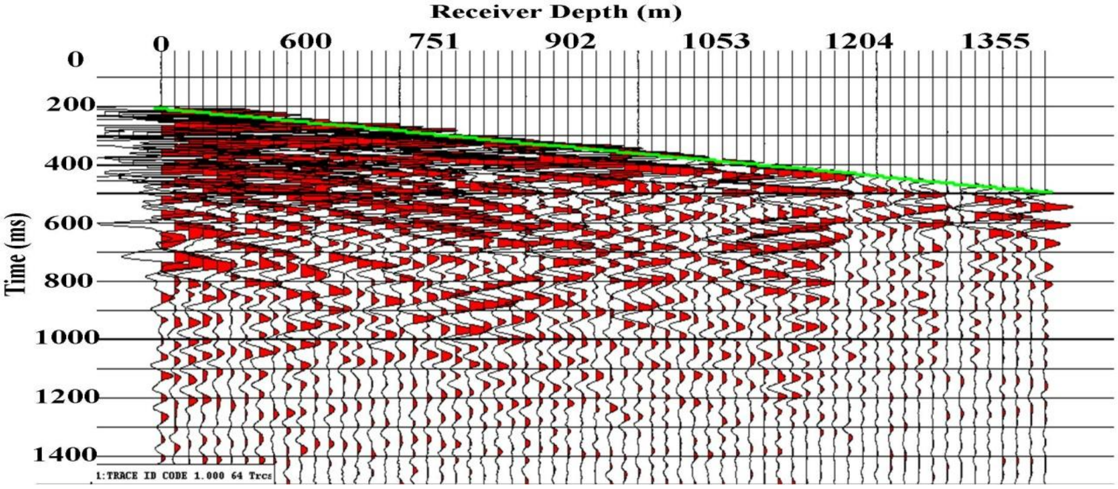

Figure A.4: East walkaway offset 249 X component with first break.

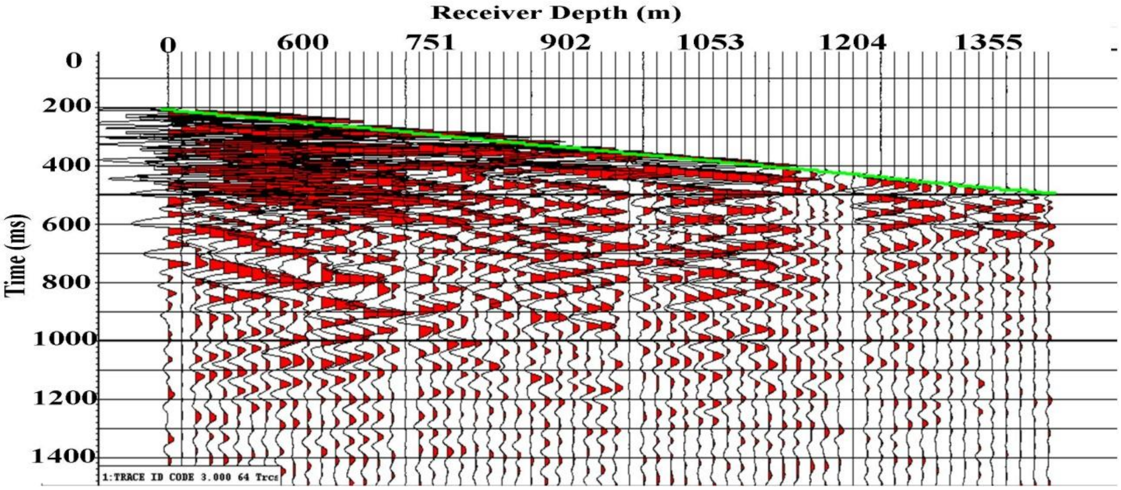

Figure A.5: East walkaway offset 249 Y component with first break.

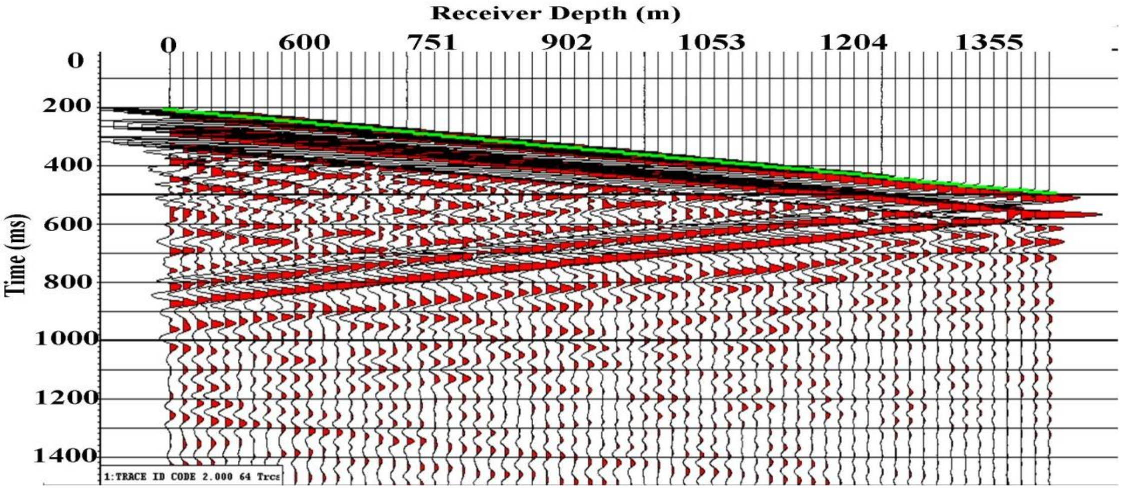

Figure A.6: East walkaway offset 249 Z component with first break.

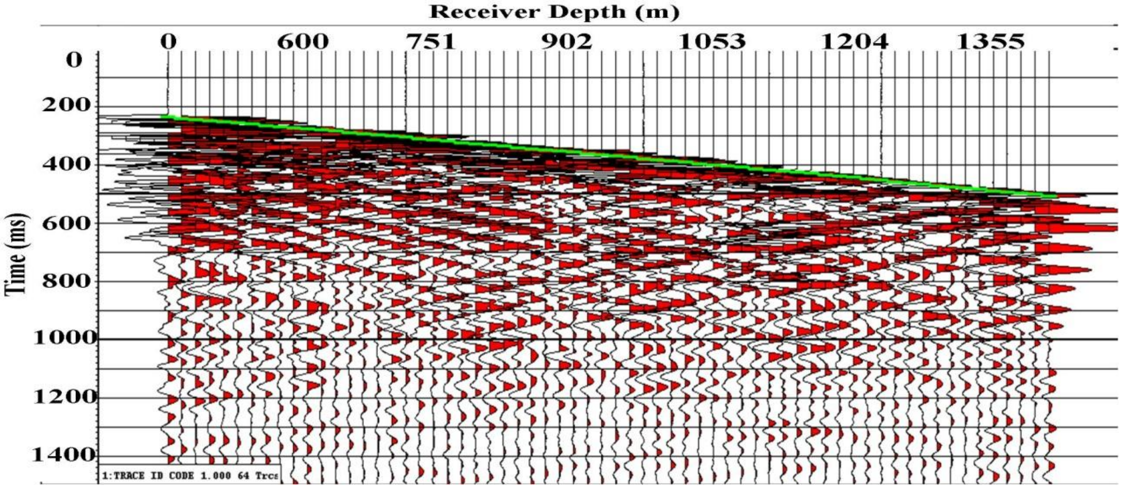

Figure A.7: East walkaway offset 388 X component with first break.

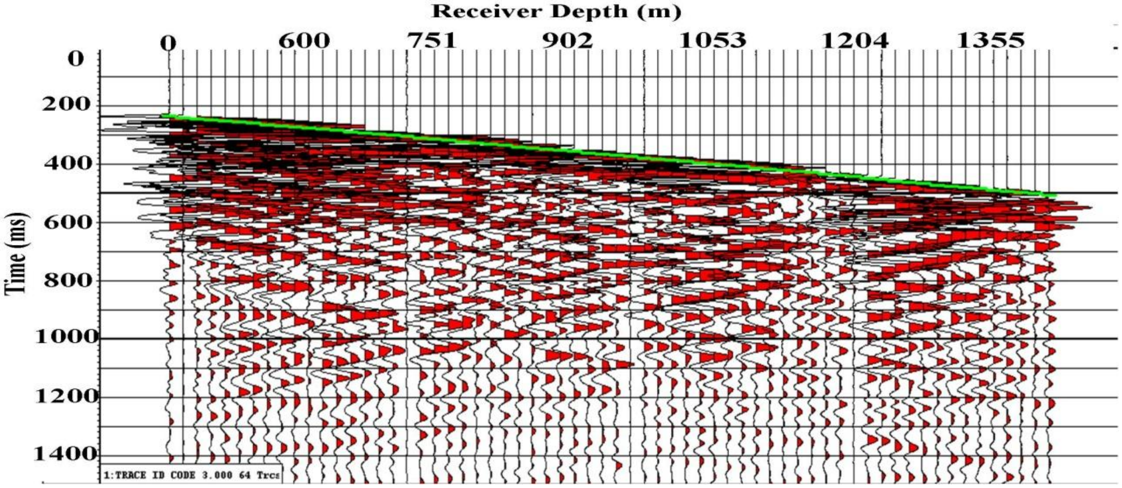

Figure A.8: East walkaway offset 388 Y component with first break.

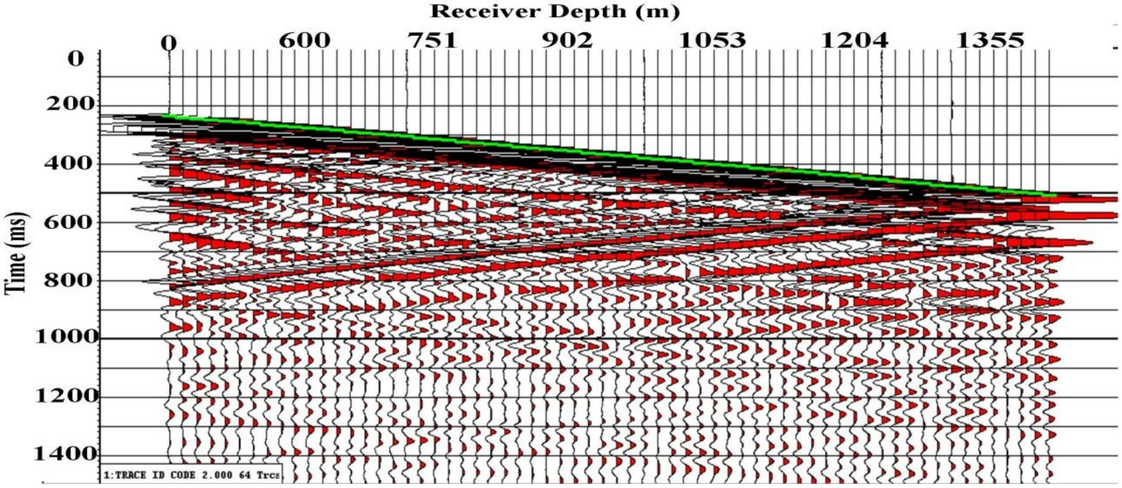

Figure A.9: East walkaway offset 388 Z component with first break.

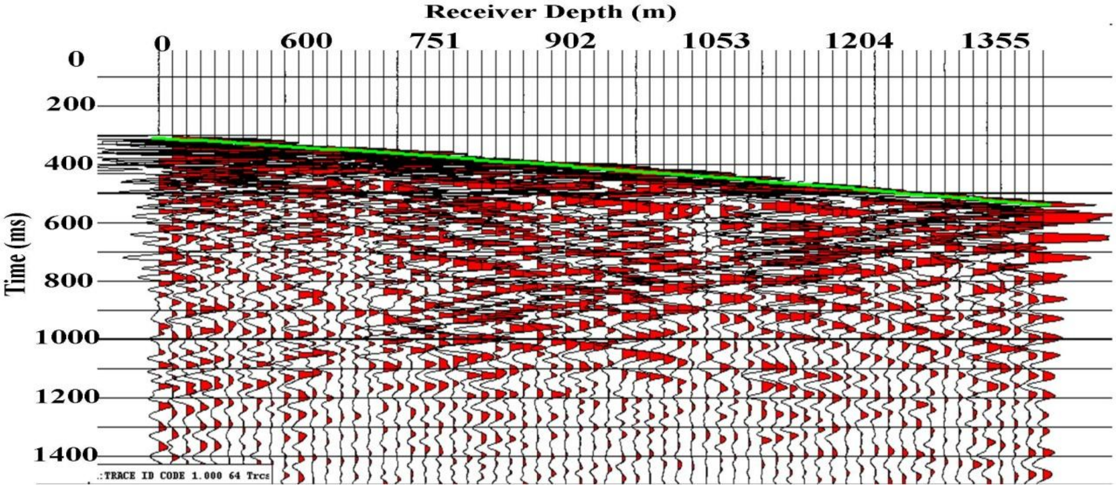

Figure A.10: East walkaway offset 667 X component with first break.

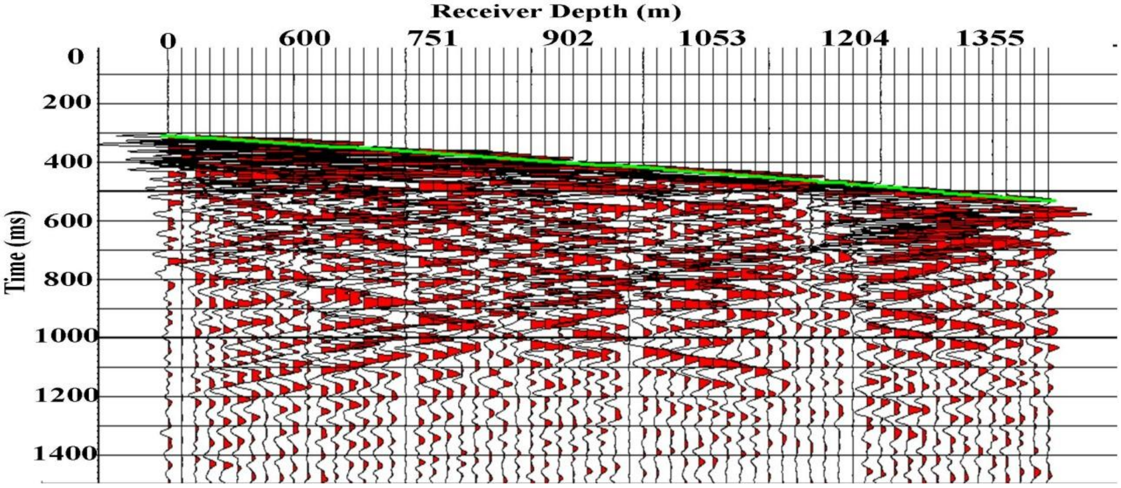

Figure A.11: East walkaway offset 667 Y component with first break.

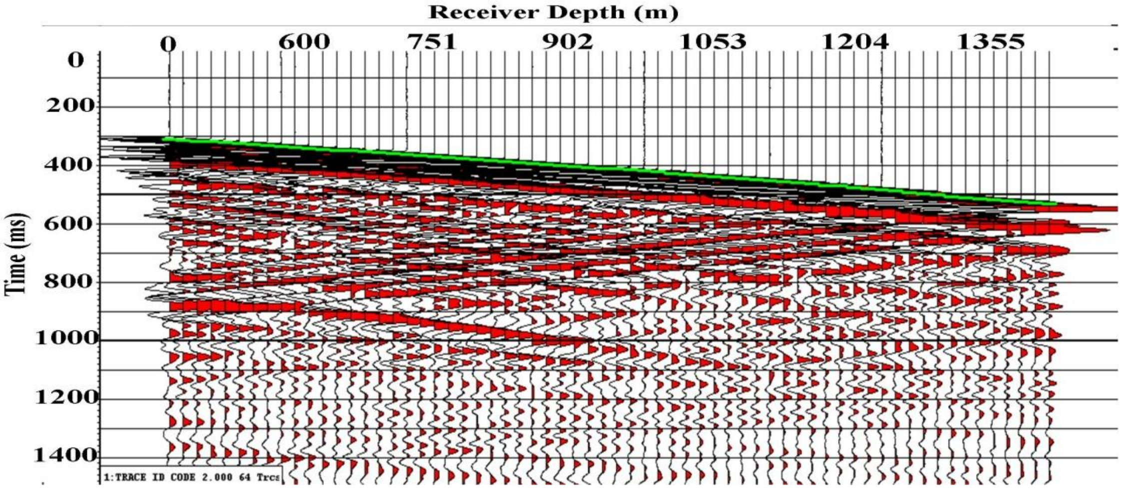

Figure A.12: East walkaway offset 667 Z component with first break.

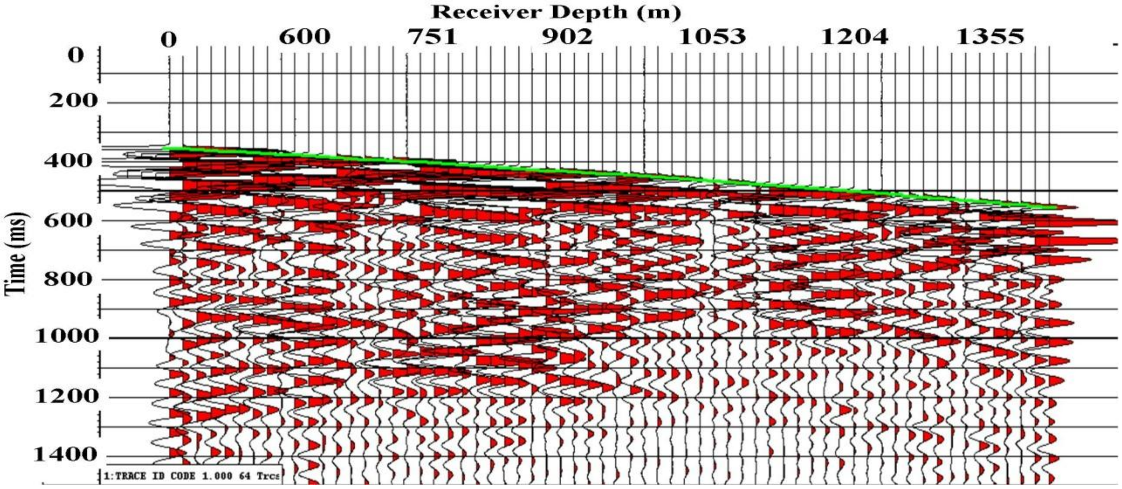

Figure A.13: East walkaway offset 807 X component with first break.

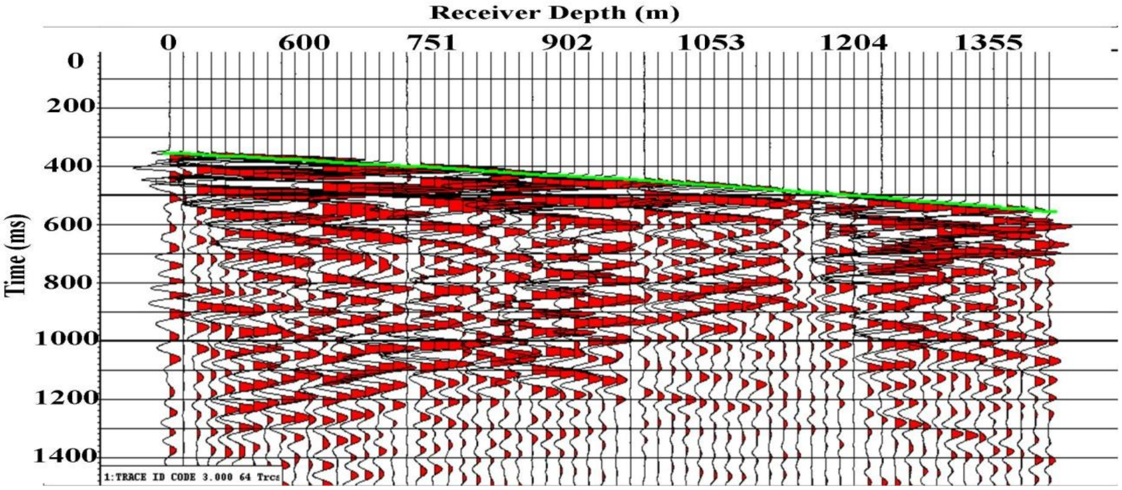

Figure A.14: East walkaway offset 807 Y component with first break.

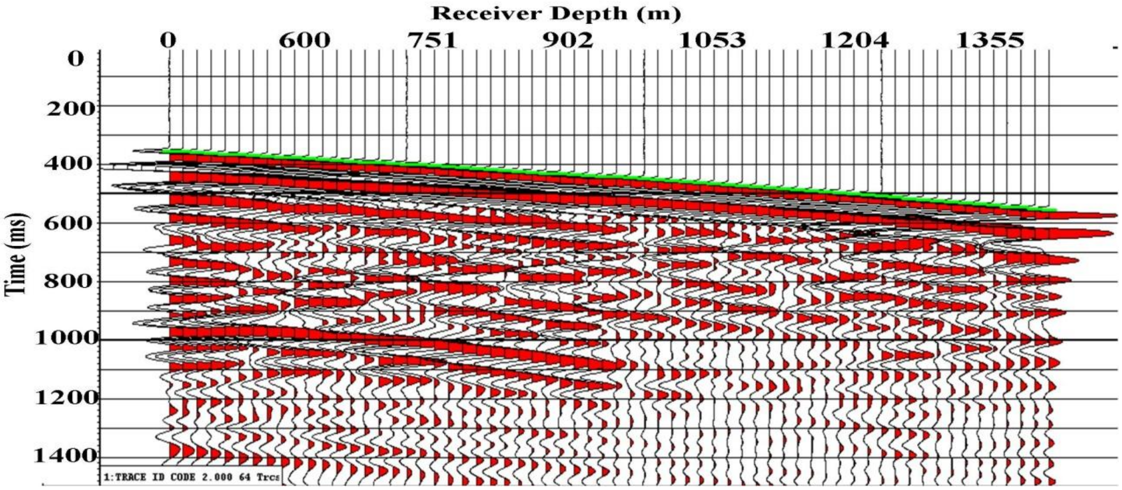

Figure A.15: East walkaway offset 807 Z component with first break.

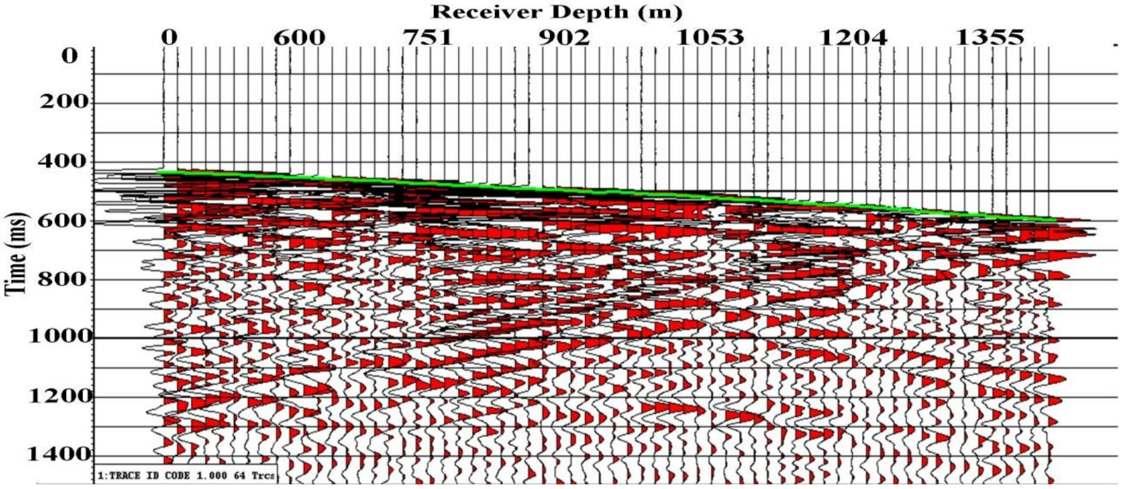

Figure A.16: East walkaway offset 1086 X component with first break.

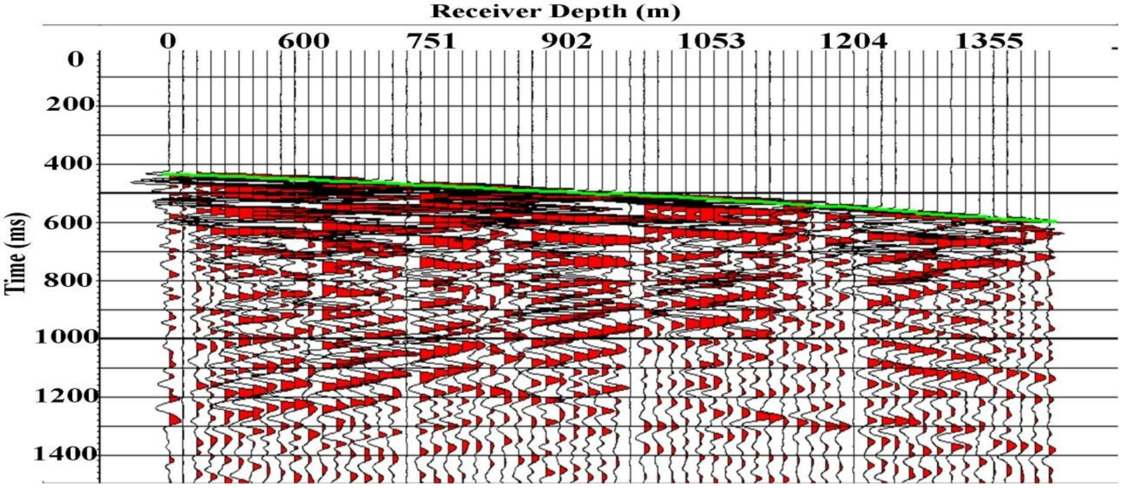

Figure A.17: East walkaway offset 1086 Y component with first break.

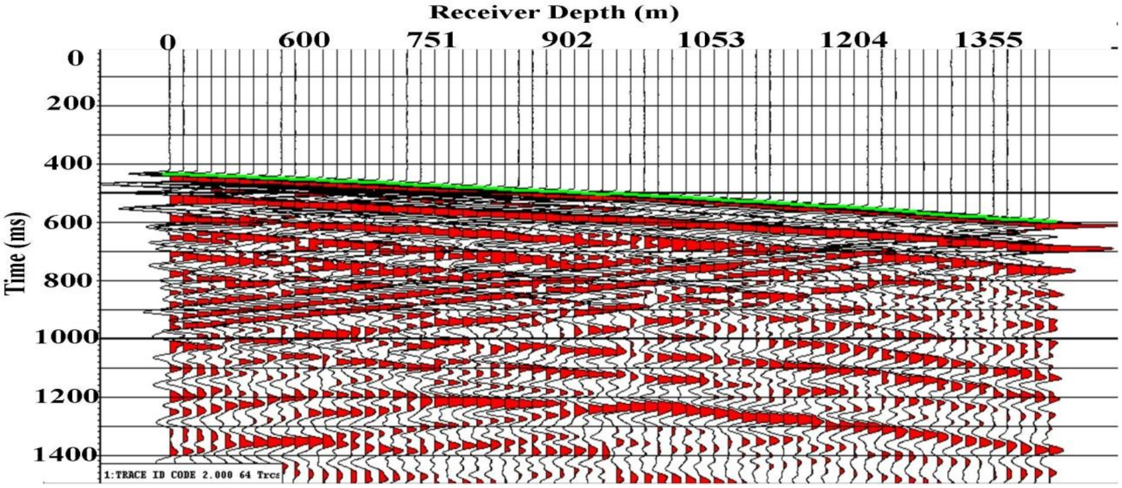

Figure A.18: East walkaway offset 1086 Z component with first break.

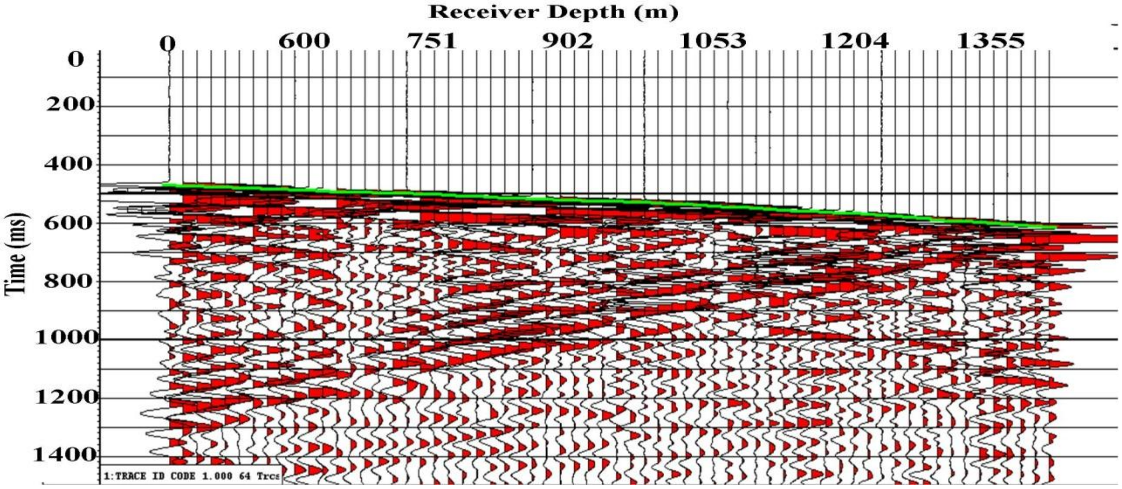

Figure A.19: East walkaway offset 1226 X component with first break.

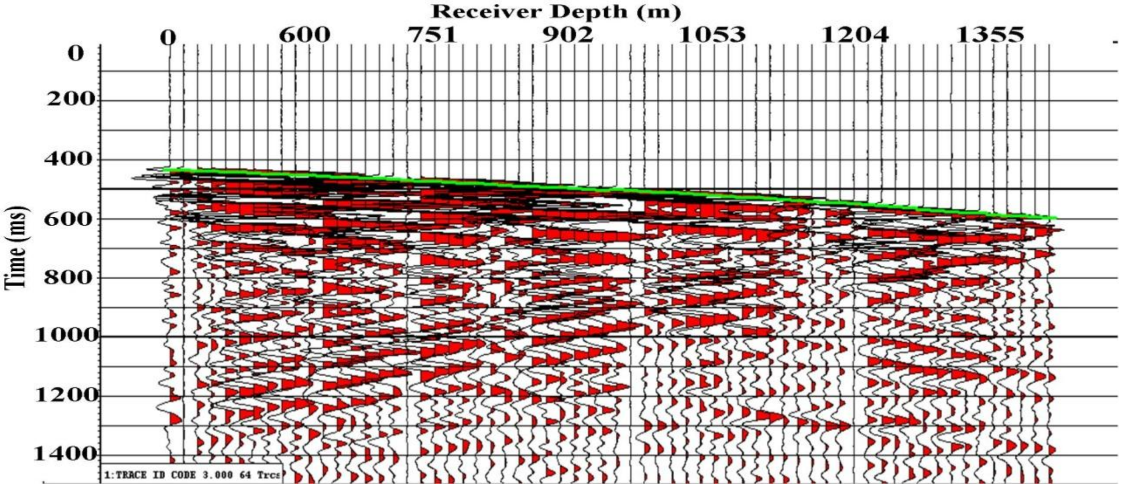

Figure A.20: East walkaway offset 1226 Y component with first break.

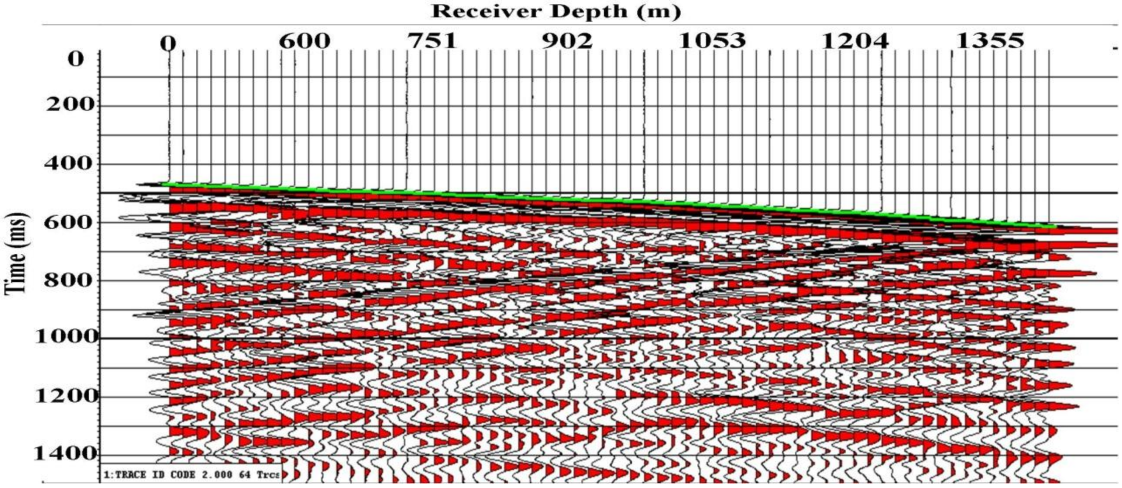

Figure A.21: East walkaway offset 1226 Z component with first break.

A number of observations are apparent about the horizontal components. The components contain mixed upgoing and downgoing wavefields especially when increasing offset. In addition, some of the traces seem to be dead traces. The two horizontal components need to be rotated in the plane of the well and the source in order to maximize the incoming energy. This is performed through hodogram rotations mentioned in Chapter 3.

As far as the vertical component, in the near offsets, the upgoing reflections are very well defined. As the offset increases, the vertical component has a lot more downgoing shear waves that super impose the upgoing wavefields. In addition, as offset increases, the dominant downgoing P waves in the vertical Z component decrease in amplitude. However, as offset increases, the amplitude of shear waves increases as well. The amount of shear wave energy increases at later times as well.

APPENDIX B: Angle of incidence calculation

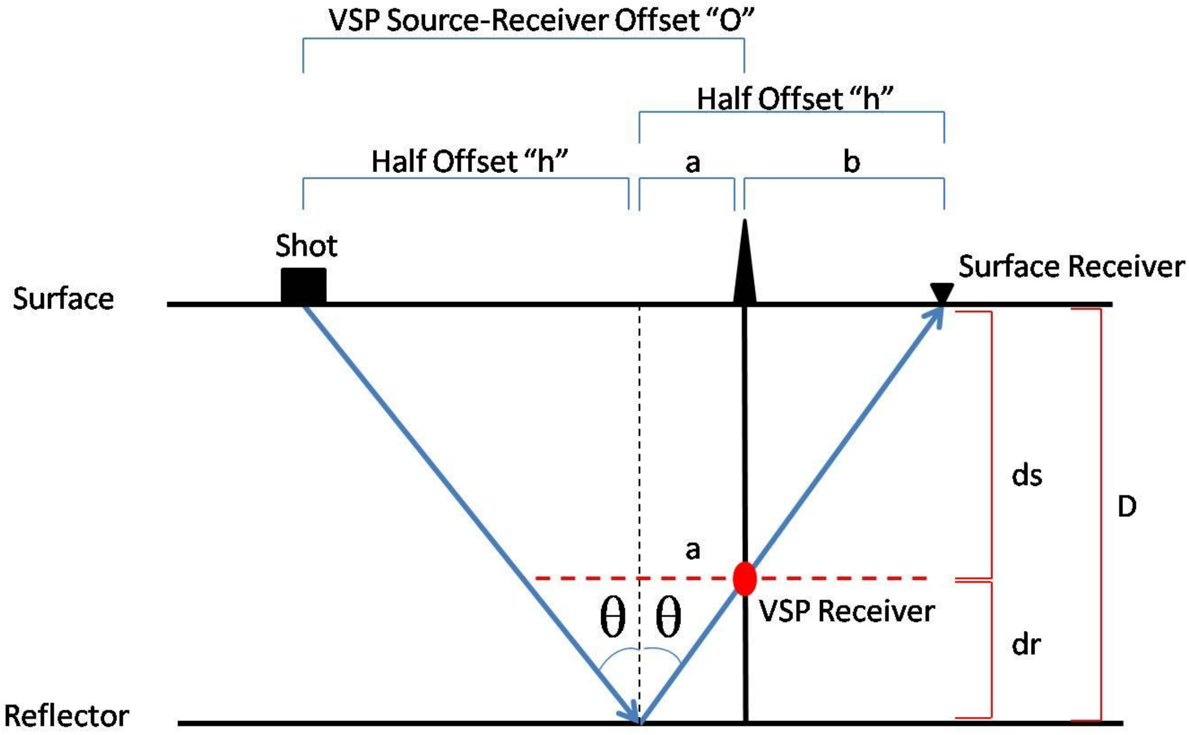

Figure B.1: Diagram of VSP angle of incidence calculation.

Assuming straight rays and knowing that the angle of incidence is equal to the angle of reflection:

From the figure we know that

$$O = h + a$$

$$tan\theta = \frac{h}{D}$$

Resubstituting for h gives:

$$tan\theta = \frac{O - a}{D}$$

Also we can see that:

$$tan\theta = \frac{a}{dr}$$

That means that:

$$a = dr\ tan\theta$$

By resubstitution:

$$tan\theta = \frac{O - (dr\ tan\theta)}{D}$$

$$D\ tan\theta = O - (dr\ tan\theta)$$

$$O = D\ tan\theta + (dr\ tan\theta)$$

$$O = \ tan\theta\ (D + dr)$$

$$tan\theta = \frac{O}{(D + dr)}$$

Tables B.1 – B.12 below show the calculation for the four deepest receivers of the survey which are essentially the closest to the Mannville B coals. These depths correspond to 1370.52 m, 1385.64 m, 1400.76 m and 1415.88 m. Ultimately an average of all these incident angle was calculated for each offset of each walkaway VSPCDP gather and shown in Table B.13. The angles are then input into the headers to turn the VSPCDP offset gathers to average angle gathers.

Table B.1: Calculation of angle of incidence for the east walkaway VSP gather for receiver depth 1370.52 m.

Walkaway	Offset (m)	Depth Of Reflector (m)	Depth Of Receiver (m)	Depth (Reflector - Receiver) (m)	Angle Of Incidence (Degrees)
East	51	1423.00	1370.52	52.48	1.98
	114	1423.00	1370.52	52.48	4.42
	249	1423.00	1370.52	52.48	9.58
	388	1423.00	1370.52	52.48	14.73
	529	1423.00	1370.52	52.48	19.72
	667	1423.00	1370.52	52.48	24.33
	807	1423.00	1370.52	52.48	28.68
	946	1423.00	1370.52	52.48	32.67
	1086	1423.00	1370.52	52.48	36.35
	1226	1423.00	1370.52	52.48	39.72

Table B.2: Calculation of angle of incidence for the east walkaway VSP gather for receiver depth 1385.64 m.

Walkaway	Offset (m)	Depth Of Reflector (m)	Depth Of Receiver (m)	Depth (Reflector - Receiver) (m)	Angle Of Incidence (Degrees)
East	51	1423	1385.64	37.36	2.00
	114	1423	1385.64	37.36	4.46
	249	1423	1385.64	37.36	9.68
	388	1423	1385.64	37.36	14.88
	529	1423	1385.64	37.36	19.91
	667	1423	1385.64	37.36	24.55
	807	1423	1385.64	37.36	28.93
	946	1423	1385.64	37.36	32.93
	1086	1423	1385.64	37.36	36.64
	1226	1423	1385.64	37.36	40.01

Table B.3: Calculation of angle of incidence for the east walkaway VSP gather for receiver depth 1400.76 m.

Walkaway	Offset (m)	Depth Of Reflector (m)	Depth Of Receiver (m)	Depth (Reflector - Receiver) (m)	Angle Of Incidence (Degrees)
East	51	1423	1400.76	22.24	2.02
	114	1423	1400.76	22.24	4.51
	249	1423	1400.76	22.24	9.78
	388	1423	1400.76	22.24	15.03
	529	1423	1400.76	22.24	20.10
	667	1423	1400.76	22.24	24.77
	807	1423	1400.76	22.24	29.18
	946	1423	1400.76	22.24	33.21
	1086	1423	1400.76	22.24	36.92
	1226	1423	1400.76	22.24	40.31

Table B.4: Calculation of angle of incidence for the east walkaway VSP gather for receiver depth 1415.88 m.

Walkaway	Offset (m)	Depth Of Reflector (m)	Depth Of Receiver (m)	Depth (Reflector - Receiver) (m)	Angle Of Incidence (Degrees)
East	51	1423	1415.88	7.12	2.04
	114	1423	1415.88	7.12	4.56
	249	1423	1415.88	7.12	9.88
	388	1423	1415.88	7.12	15.18
	529	1423	1415.88	7.12	20.30
	667	1423	1415.88	7.12	25.00
	807	1423	1415.88	7.12	29.44
	946	1423	1415.88	7.12	33.48
	1086	1423	1415.88	7.12	37.21
	1226	1423	1415.88	7.12	40.61

Table B.5: Calculation of angle of incidence for the southeast walkaway VSP gather for receiver depth 1370.52 m.

Walkaway	Offset (m)	Depth Of Reflector (m)	Depth Of Receiver (m)	Depth (Reflector - Receiver) (m)	Angle Of Incidence (Degrees)
Southeast	51	1423.00	1370.52	52.48	1.98
	131	1423.00	1370.52	52.48	5.07
	270	1423.00	1370.52	52.48	10.37
	431	1423.00	1370.52	52.48	16.28
	551	1423.00	1370.52	52.48	20.48
	692	1423.00	1370.52	52.48	25.13
	830	1423.00	1370.52	52.48	29.36
	970	1423.00	1370.52	52.48	33.32
	1100	1423.00	1370.52	52.48	36.71
	1250	1423.00	1370.52	52.48	40.27
	1391	1423.00	1370.52	52.48	43.31

Table B.6: Calculation of angle of incidence for the southeast walkaway VSP gather for receiver depth 1385.64 m.

Walkaway	Offset (m)	Depth Of Reflector (m)	Depth Of Receiver (m)	Depth (Reflector - Receiver) (m)	Angle Of Incidence (Degrees)
Southeast	51	1423	1385.64	37.36	2.00
	131	1423	1385.64	37.36	5.13
	270	1423	1385.64	37.36	10.47
	431	1423	1385.64	37.36	16.44
	551	1423	1385.64	37.36	20.67
	692	1423	1385.64	37.36	25.35
	830	1423	1385.64	37.36	29.61
	970	1423	1385.64	37.36	33.59
	1100	1423	1385.64	37.36	36.99
	1250	1423	1385.64	37.36	40.56
	1391	1423	1385.64	37.36	43.61

Table B.7: Calculation of angle of incidence for the southeast walkaway VSP gather for receiver depth 1400.76 m.

Walkaway	Offset (m)	Depth Of Reflector (m)	Depth Of Receiver (m)	Depth (Reflector - Receiver) (m)	Angle Of Incidence (Degrees)
Southeast	51	1423	1400.76	22.24	2.02
	131	1423	1400.76	22.24	5.18
	270	1423	1400.76	22.24	10.58
	431	1423	1400.76	22.24	16.61
	551	1423	1400.76	22.24	20.87
	692	1423	1400.76	22.24	25.59
	830	1423	1400.76	22.24	29.87
	970	1423	1400.76	22.24	33.87
	1100	1423	1400.76	22.24	37.28
	1250	1423	1400.76	22.24	40.86
	1391	1423	1400.76	22.24	43.90

Table B.8: Calculation of angle of incidence for the southeast walkaway VSP gather for receiver depth 1415.88 m.

Walkaway	Offset (m)	Depth Of Reflector (m)	Depth Of Receiver (m)	Depth (Reflector - Receiver) (m)	Angle Of Incidence (Degrees)
Southeast	51	1423	1415.88	7.12	2.04
	131	1423	1415.88	7.12	5.23
	270	1423	1415.88	7.12	10.69
	431	1423	1415.88	7.12	16.77
	551	1423	1415.88	7.12	21.07
	692	1423	1415.88	7.12	25.82
	830	1423	1415.88	7.12	30.13
	970	1423	1415.88	7.12	34.15
	1100	1423	1415.88	7.12	37.57
	1250	1423	1415.88	7.12	41.16
	1391	1423	1415.88	7.12	44.21

Table B.9: Calculation of angle of incidence for the south walkaway VSP gather for receiver depth 1370.52 m.

Walkaway	Offset (m)	Depth Of Reflector (m)	Depth Of Receiver (m)	Depth (Reflector - Receiver) (m)	Angle Of Incidence (Degrees)
South	51	1423.00	1370.52	52.48	1.98
	139	1423.00	1370.52	52.48	5.38
	240	1423.00	1370.52	52.48	9.24
	379	1423.00	1370.52	52.48	14.41
	518	1423.00	1370.52	52.48	19.34
	647	1423.00	1370.52	52.48	23.68
	802	1423.00	1370.52	52.48	28.53
	938	1423.00	1370.52	52.48	32.45
	1079	1423.00	1370.52	52.48	36.18
	1214	1423.00	1370.52	52.48	39.45
	1346	1423.00	1370.52	52.48	42.37

Table B.10: Calculation of angle of incidence for the south walkaway VSP gather for receiver depth 1385.64 m.

Walkaway	Offset (m)	Depth Of Reflector (m)	Depth Of Receiver (m)	Depth (Reflector - Receiver) (m)	Angle Of Incidence (Degrees)
South	51	1423	1385.64	37.36	2.00
	139	1423	1385.64	37.36	5.44
	240	1423	1385.64	37.36	9.33
	379	1423	1385.64	37.36	14.55
	518	1423	1385.64	37.36	19.53
	647	1423	1385.64	37.36	23.90
	802	1423	1385.64	37.36	28.77
	938	1423	1385.64	37.36	32.71
	1079	1423	1385.64	37.36	36.46
	1214	1423	1385.64	37.36	39.74
	1346	1423	1385.64	37.36	42.67

Table B.11: Calculation of angle of incidence for the south walkaway VSP gather for receiver depth 1400.76 m.

Walkaway	Offset (m)	Depth Of Reflector (m)	Depth Of Receiver (m)	Depth (Reflector - Receiver) (m)	Angle Of Incidence (Degrees)
South	51	1423	1400.76	22.24	2.02
	139	1423	1400.76	22.24	5.49
	240	1423	1400.76	22.24	9.43
	379	1423	1400.76	22.24	14.69
	518	1423	1400.76	22.24	19.72
	647	1423	1400.76	22.24	24.12
	802	1423	1400.76	22.24	29.03
	938	1423	1400.76	22.24	32.98
	1079	1423	1400.76	22.24	36.74
	1214	1423	1400.76	22.24	40.03
	1346	1423	1400.76	22.24	42.96

Table B.12: Calculation of angle of incidence for the south walkaway VSP gather for receiver depth 1415.88 m.

Walkaway	Offset (m)	Depth Of Reflector (m)	Depth Of Receiver (m)	Depth (Reflector - Receiver) (m)	Angle Of Incidence (Degrees)
South	51	1423	1415.88	7.12	2.04
	139	1423	1415.88	7.12	5.55
	240	1423	1415.88	7.12	9.53
	379	1423	1415.88	7.12	14.84
	518	1423	1415.88	7.12	19.91
	647	1423	1415.88	7.12	24.34
	802	1423	1415.88	7.12	29.28
	938	1423	1415.88	7.12	33.26
	1079	1423	1415.88	7.12	37.03
	1214	1423	1415.88	7.12	40.33
	1346	1423	1415.88	7.12	43.26

Table B.13: East walkaway average angle calculation.

Walkaway	Offset (m)	Angle Of Incidence (Degrees)
East	51	2.01
	114	4.49
	249	9.73
	388	14.95
	529	20.01
	667	24.66
	807	29.05
	946	33.07
	1086	36.78
	1226	40.16

Table B.14: Southeast walkaway average angle calculation.

Walkaway	Offset (m)	Angle Of Incidence (Degrees)
Southeast	51	2.01
	131	5.15
	270	10.53
	431	16.53
	551	20.77
	692	25.47
	830	29.74
	970	33.73
	1100	37.13
	1250	40.71
	1391	43.76

Table B.15: South walkaway average angle calculation.

Walkaway	Offset (m)	Angle Of Incidence (Degrees)
South	51	2.01
	139	5.47
	240	9.38
	379	14.62
	518	19.63
	647	24.01
	802	28.90
	938	32.85
	1079	36.60
	1214	39.89
	1346	42.82